

**DESIGN AND CONTROL OF A TELE-OPERATED MOBILE
PLATFORM**

AMAREN PRASANNA DAS



**DEPARTMENT OF MECHANICAL ENGINEERING
INDIAN INSTITUTE OF TECHNOLOGY DELHI**

DECEMBER 2018

DESIGN AND CONTROL OF A TELE-OPERATED MOBILE PLATFORM

by

AMAREN PASANNA DAS

Department of Mechanical Engineering

Submitted

in fulfilment of the requirements of the degree of Doctor of Philosophy

to the



INDIAN INSTITUTE OF TECHNOLOGY DELHI

DECEMBER 2018

Certificate

This is to certify that the thesis entitled **DESIGN AND CONTROL OF A TELE-OPERATED MOBILE PLATFORM**, submitted by **Shri. Amaren Prasanna Das** to the Indian Institute of Technology Delhi, for the award of the degree of **Doctor of Philosophy** in Mechanical Engineering, is a record of the original, bona-fide research work carried out by him under our supervision and guidance. The thesis has reached the standards fulfilling the requirements of the regulations related to the award of the degree.

The results contained in this thesis have not been submitted in part or in full to any other university or institute for the award of any degree or diploma.

Prof. S. K. Saha

Professor

Department of Mechanical Engineering
Indian Institute of Technology Delhi
New Delhi - 110016, India

Prof. S. Bhasin

Associate Professor

Department of Electrical Engineering
Indian Institute of Technology Delhi
New Delhi - 110016, India

Dr. D. N. Badodkar

Ex-Group Director RDDG & Ex-Prof. HBNI
Bhabha Atomic Research Center
Mumbai, India

In memory of my father

Late Shri Shyam Narayan Das

Acknowledgements

The work presented in this thesis would not have been possible without the assistance of countless individuals. I extend my eternal gratitude to all those people. However, despite being a dangerous practice, I would like to single out a few, select, individuals for special recognition.

This thesis would not have seen the light of the day without the continuous and persistent motivation of my guide Prof. S. K. Saha. His advice and guidance on technical issues helped give direction to this research. Moreover, he played a pivotal role in providing the much needed psychological and emotional support. Each and every meeting with him was a booster to my self confidence.

I am deeply grateful to my co-supervisor, Professor S. Bhasin in the Department of Electric Engineering at IIT-Delhi, for his continued encouragement and invaluable suggestions in the field of control engineering and in particular adaptive control during this work. He has been instrumental in introducing me to the latest research results in the field of time delayed non-linear systems. I also express my gratitude to Dr. Deepak N Badodkar, my supervisor at my parent organization BARC, Mumbai for his encouragement and the logistic support he had provided throughout the tenure of my research. Without his support the development and fabrication of the physical system would not have been possible.

It will be imprudent not to mention the help and support provided by my colleague Shri. Rahul V Sakrikar. One person, on whom I fell back in case of any hardware issues be it electrical or mechanical. While discussing and sorting out technical glitches I found his profound experience and field knowledge highly enriching. I still remember his *encouraging* words, “Are tera PhD ka kya hua? Saha kuch kaam nahi deya kya?” Another colleague, Shri Shishir Kr. Singh has provided his selfless service to help me develop all the software required for running the actual system. Without his help and support it would have been impossible

to conduct experimental runs and data collection. I express my deepest regards to both of them.

I cannot forget the support and help of my co-researchers and classmates Dr. Riby Abraham, Dr. Parmanand Nandihal, Dr. Abdullah Aamir Hayat and Dr. Arun Dayal Uday during my stay and course work at IIT-Delhi. Thereafter, providing all kinds of logistic support at IIT-Delhi. Without their help it would have been impossible to continue my work at IIT-Delhi. I thank them from the bottom of my heart and wish them grand success in their life.

Finally, I thank my two daughters, Akaisha and Sayuri, my mother for their patience and support. Special thanks to my wife Namrata, who had taken upon herself the responsibility of managing the family during my course work at IIT-Delhi and providing the required time and space for my research work thereafter. In absence of her support, patience and companionship this journey would not have been completed.

Amaren Pasanna Das

Abstract

A customized Redundantly Actuated Redundantly Steered (RARS) mobile manipulator tolerant to single actuator failure was designed, developed and fabricated for radiation measurement and mapping. The detail design aspects based on the environment and mission requirement is presented in the thesis. The dynamic model of the system with wheel slip was developed using Natural Orthogonal Compliment (NOC) approach and simulations were performed for specific paths to verify the actuator requirements and response time. The user interface and control architecture implemented on the mobile robot for teleoperation were developed for convenient and reliable functioning of the same. The time delay introduced due to video data transfer and its effects on system's stability and poor operator performance is demonstrated using simulations. A predictive display of the remote environment based on mathematical model of the mobile robot and RGB-Depth sensor data received from remote location is proposed, which was practically implemented. This strategy has largely improved robot's navigation by the operator even over significantly delayed communication network.

Contents

Certificate	i
Acknowledgements	v
Abstract	vii
Table of Contents	ix
List of Figures	xiii
List of Tables	xvii
1 Introduction	1
1.1 Literature Survey	4
1.1.1 Special purpose robots	4
1.1.2 Redundant mobile robots	6
1.1.3 Mathematical modeling	7
1.1.4 Stability of mobile manipulator	9
1.1.5 Path tracking	10
1.1.6 Obstacle avoidance and path planning	11
1.1.7 Tele-operation	13
1.1.7.1 Human interface	13
1.1.7.2 Control of time delayed teleoperation	14
1.1.8 Predictive display	15
1.2 Research gaps and contributions	16
1.3 Thesis Organization	17
2 Design of the RARS Mobile Robot	21

2.1	Design Overview	22
2.2	Kinematic Topology	24
2.3	Design of the Traction System	25
2.3.1	Stability of mobile manipulator	26
2.3.2	Selection of motor and gearbox	30
2.4	Design of Steering System	31
2.4.1	Minimum turning radius	32
2.4.2	Calculation of steering torque	34
2.5	Scissor Mechanism for Manipulator Arm	34
2.6	Summary	36
3	Dynamics of Wheeled Mobile Robots	39
3.1	Modeling using the Natural Orthogonal Compliment (NOC)	40
3.2	Dynamic Equation of WMR	43
3.2.1	Kinematic analysis	44
3.2.2	Special cases	49
3.2.2.1	Standard caster ($d_1 = 0$)	49
3.2.2.2	Under-actuated case ($d_2 = 0$)	50
3.3	Dynamics with No Wheel Slip	50
3.3.1	Generalized inertia matrix, \mathbf{I}	50
3.3.2	Matrix of convective inertia term \mathbf{C}	52
3.3.3	Simulation	54
3.3.4	Inverse dynamics	55
3.4	Dynamics with Wheel Slip	57
3.4.1	Defining Slip	57
3.4.2	Kinematics with wheel slip	59
3.4.3	Dynamics with wheel slip	66
3.4.4	Simulation	70
3.4.5	Results and inference	73
3.5	Dynamical Model of Steering System	76

3.5.1	Design of PID controller	80
3.5.2	Simulation and results	82
3.6	Summary	83
4	Control of a Mobile Manipulator	85
4.1	Control Architecture and Hardware	85
4.1.1	Local onboard controller	86
4.1.2	Details of the motor controller	88
4.2	Control Algorithm	90
4.2.1	Safety interlocks	95
4.2.2	Wheel odometry	95
4.3	Remote control station	98
4.4	Summary	99
5	Simulation of Tele-operation	101
5.1	Modeling of Mobile Robot	102
5.2	Model of Human Operator	102
5.3	Simulation and Results	105
5.3.1	Simulation algorithm	105
5.4	Summary	107
6	Predictive Display for Time Delay Compensation	109
6.1	Time Delay Compensation	109
6.1.1	Proposed controller	111
6.1.2	Simulation algorithm and results	113
6.2	Delay Compensation using Predictive Display	114
6.2.1	The Kinect sensor	115
6.2.2	Onboard data processing and transmission	116
6.2.3	3-D reconstruction	117
6.2.4	Extrapolation of remote scene	118
6.3	Summary	119

7 Conclusions	121
7.1 Thesis Summary	121
7.2 Current Status	123
7.3 Future Scope	123
Bibliography	127
A	139
A.1 Measurment of Time Delay in Video Feedback	139
B	141
B.1 Stability of Pure Pursuit under Time Delay	141
C	145
C.1 Optimal Design of Steering Linkages	145
Publications from the Thesis	147
Brief Bio-data of the Author	149

List of Figures

1.1	Robotics in factory (Source: Kuka Robot)	2
1.2	Health care (Source: da Vinci Surgical System)	2
1.3	Exploration and surveillance Source: Autonomous Space Robotics Lab - University of Toronto	2
1.4	Honda Asimo, Source: http://asimo.honda.com	2
1.5	Sony Abio, Source: https://us.aibo.com/	2
1.6	Robot for Fukushima Daiichi, Source: Ohno, et al [1]	4
1.7	NERO III, Source: Luk et al [2]	4
1.8	Kuka AGV OmniMove https://www.kuka.com/en-in/products/mobility	5
1.9	Mobile robot with PCW [8]	5
1.10	Follow the carrot	11
1.11	Vector pursuit	11
2.1	3-D Model of the mobile manipulator	23
2.2	Photograph of the actual system	24
2.3	Rear suspension	26
2.4	Mobile manipulator on slope	27
2.5	Centrifugal forces	30
2.6	RARS support polygon	30
2.7	Ackerman steering condition	32
2.8	Davis steering gear	33
2.9	Steer torque	33
2.10	Scissor mechanism	35

3.1	WMR-Std. caster	44
3.2	WMR-general	44
3.3	Path traced by robot	55
3.4	Inverse dynamics of the mobile robot	57
3.5	Longitudinal slip [132]	58
3.6	Wheel skid [132]	58
3.7	Free body diagram of RARS robot	60
3.8	External force on rear wheel	68
3.9	External forces on front wheel	68
3.10	Friction model	73
3.11	Input torque profile	73
3.12	RARS path traced when $\mu = 0.3$	74
3.13	Forces on RARS when $\mu = 0.3$	74
3.14	RARS, radial deviation ($\mu = 0.3$)	75
3.15	Phase and phase error ($\mu = 0.3$)	75
3.16	RARS path traced when $\mu = 0.1$	75
3.17	Forces on RARS when $\mu = 0.1$	75
3.18	RARS radial deviation ($\mu = 0.1$)	76
3.19	Phase and phase error ($\mu = 0.1$)	76
3.20	Plot of β and $\dot{\beta}$	76
3.21	Steering assembly	77
3.22	Steering linkage	77
3.23	Change in steer angle	82
3.24	Control effort	82
4.1	Control architecture	85
4.2	Data from PC to the robot	86
4.3	Data from the robot to PC	86
4.4	Wiring diagram of the WMR	87
4.5	Block diagram of EPOS4 controller	88

4.6	Current control block	89
4.7	Velocity control bolck	89
4.8	Position control bolck	91
4.9	Block diagram of WMR controller	92
4.10	Ackerman steering condition	93
4.11	Davis steering gear	93
4.12	Tracing a line	96
4.13	Motor torque	96
4.14	Linear velocity	96
4.15	Angular velocity	96
4.16	Tracing a circle	97
4.17	Motor torque	97
4.18	Linear velocity	97
4.19	Angular velocity	97
4.20	User interface for teleoperation	98
5.1	Teleoperation architecture	101
5.2	Assumed driving strategy	103
5.3	Geometry of Pure pursuit	104
5.4	Simulation scheme	105
5.5	Block diagram for teleoperation	106
5.6	Simulation with no time delay in either direction	107
5.7	Simulation with time delay $h_1 = .5$ sec and $h_2 = 0$ sec	108
5.8	Simulation with time delay $h_1 = .8$ sec and $h_2 = 0$ sec	108
6.1	Smith predictor [142]	110
6.2	Block diagram of time delayed system	111
6.3	Delay measurment	111
6.4	Smith predictor applied to RARS mobile robot	112
6.5	Simulation block diagram	112

6.6	Time delay $T_1 = .5$ sec and $T_2 = 0$ sec	114
6.7	Time delay $T_1 = .8$ sec and $T_2 = 0$ sec	114
6.8	Kinect sensor from Microsoft	115
6.9	Predictive display architecture	117
6.10	PCD at time T	119
6.11	Predicted scene	119
7.1	QR code Youtube	123
7.2	QR Code alternate	123
A.1	User interface for teleoperation	140
A.2	Experimental setup: Schematic	140
A.3	Screen shot of operator PC	140
B.1	Results obtained by Ollero [45]	143

List of Tables

2.1	Key parameters and specifications of the mobile manipulator.	23
3.1	Dynamic and kinematic parameters	56
3.2	Key parameters steering assembly.	82
4.1	Proportionality constant table	88
4.2	Parameters for left and right rear wheel motor controllers	90
4.3	Parameters of steering motor controller	91

Chapter 1

Introduction

The use of robots such as robotic arm shown in Figure 1.1 has been used in factories for a long time, basically for repetitive kind of job. Though it started with the intention to reduce human labour, production cost, and increased productivity, with technological development their scope has expanded beyond manufacturing domain. Robots are now being used for health care, surveillance, exploration, etc. as illustrated in Figures 1.2 and 1.3. The reduction in development cost has resulted in introduction of robotic systems in entertainment industries and personal care as well. Robots have matured from heavy duty serial linked mechanical arms to a more presentable form such as ASIMO (Figure 1.4) by Honda and Aibo by Sony (Figure 1.5).

In areas where human access is not preferred or restricted due to risk of life or inhospitable environmental conditions as in chemical, space or nuclear industries, robotic systems have gained huge popularity in providing services as surveillance, rescue, exploration and remote maintenance. Research in teleoperated and autonomous mobile robotics has been fuelled largely by these requirements. Teleoperated mobile robots are suitable for these applications as the workspace required to be covered is very large, and it is essential to maintain physical separation between the robot and its control station. Moreover, the remote environment is in general unknown.



Figure 1.1: Robotics in factory (Source: Kuka Robot)



Figure 1.2: Health care
(Source: da Vinci Surgical System)



Figure 1.3: Exploration and surveillance
Source: Autonomous Space Robotics
Lab - University of Toronto



Figure 1.4: Honda Asimo,
Source:<http://asimo.honda.com>



Figure 1.5: Sony Aibo,
Source: <https://us.aiobo.com/>

The present research too was motivated by a similar requirement for in-situ measurement of the ionizing radiation and neutron field, inside the vault and cave areas of K-130, K-500 and Medical Cyclotron operational at VECC, Kolkata, West Bengal. Cyclotrons are used to accelerate charged particles to high energies. These are required for experiments in nuclear physics and nuclear medicine. The particles are accelerated to high energy using a high frequency alternating voltage, which is applied between two hollow “D”-shaped sheet metal electrodes called “Dees” inside a vacuum chamber. The area surrounding the Dee is called the vault. The cave is the area where beam line (beam of accelerated charged particles) is available for experimentation. Radiation mapping of these areas is a mandatory requirement for getting safety clearance from regulators during commissioning of new units and at regular intervals during operational life of the cyclotron facility. Though, there are radiation detectors placed at different locations in these areas they can only measure radiation levels at discrete locations, but can not provide the 3-D radiation map. The advantage of having a radiation map is that it provide detailed input to health physicist of the dose a person may receive and accordingly plan emergency operations. These maps also provide the plant operators with the location of radiation leakage and accordingly tune the system to improve its efficiency.

The challenge faced for in-situ inspection during operation of cyclotron is that the interaction between an accelerated beam of charged particles and the target produce Bremsstrahlung and characteristic X-rays, prompt γ -rays, neutrons and delayed radiation (β and γ) this makes human presence unacceptable. A teleoperated mobile robot with wireless communication link is the obvious solution. As the robot is to move in areas where human presence is prohibited, it was important that the robot should be recoverable even in case of actuator failure during field operation. This thesis discusses the design, analysis and development of a prototype robot to carry out in-situ measurement and mapping of radiation level.



Figure 1.6: Robot for Fukushima
Daiichi,
Source: Ohno, et al [1]

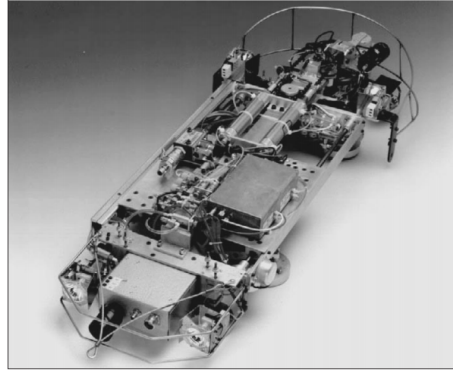


Figure 1.7: NERO III,
Source: Luk et al [2]

1.1 Literature Survey

In this section, we discuss some of the important works published pertaining to the scope of this thesis. Few of the techniques and methods published in these literatures are directly used. The section on *Special Purpose Robots* lists literature which were reviewed to arrive at the overall design of the mobile robot developed in this research. The dynamic analysis of the mobile platform was based on the works cited in section *Mathematical Modeling*. The literature discussed in *Path Tacking* helped to arrive at the “human model” proposed in this thesis for simulation of teleoperation. The section on *Tele-operation* discusses literature in a much broader sense; such as force feedback, haptic interface design, etc., than what was adapted in this thesis. This was done for completeness of the subject. Last section on *Predictive Display*, though a part of human interface for teleoperation is discussed separately because it forms one of the major components of the tele-operation system network designed for the mobile robot presented in this thesis.

1.1.1 Special purpose robots

This section reviews some of the special purpose robots built for various applications. Design and fabrication of a low cost, solar powered mobile robot for scientific



Figure 1.8: Kuka AGV OmniMove
<https://www.kuka.com/en-in/products/mobility>



Figure 1.9: Mobile robot with PCW [8]

missions on the Antarctic plateau was presented by Ray [3]. Honeycomb-glass-fibre composite was used to provide high strength and low weight. Ohno, et al. [1] developed a robotic vehicle shown in Figure 1.6 for measuring the radiation in the Fukushima Daiichi Nuclear Power Plant. A survey of different types of climbing robots for non-destructive testing of pressure vessel is given by Luk [2], such as NERO III shown in Figure 1.7. Briones [4] presents a vacuum cup based wall climbing robot for inspection of nuclear power plants. Galt [5] has developed eight-legged teleoperated mobile robot for the use in nuclear industry. Development of a magnetic-wheel based mobile robot for painting of ship is discussed by Cho [6]. Compliant link based mobile robot was designed and tested by Borenstein[7], in which the author claims that due to its unique design, better dead-reckoning accuracy was achieved compared to other contemporary designs. This vehicle has two independent drive units or "trucks" that are free to rotate about a vertical shaft connected to the vehicle body. Each truck comprises two drive motors on a common axes and forms a differential drive system. Mechanical compliance was implemented by means of a linear bearing that allows relative motion between the front and rear truck. Other literature giving details of mobile robots based on differential wheel, traction belt and omnidirectional wheel are given in the introductory part of Chapter 2.

1.1.2 Redundant mobile robots

The robots discussed above were designed for some specific task. Therefore each differed from another in some design aspect which is specific to its task requirement. The major design requirement for the robot at hand, as discussed in the introduction of this chapter, was to give it enough mobility so that it can be recovered from the high radiation zone to a safe area even in case one of the actuators fail. This feature is referred as *single actuator fault tolerant design*. This is achieved by providing redundant actuators. There are number of mobile robots which use redundant actuation. They are based either on omni-directional (also called Mecanum or Swedish) wheel or Powered Caster wheels. Muir[9], Yi[10], Lin [11], Diegel [12] and Taheri [13] have presented mobile platforms with 4 Mecanum wheels which are redundant systems. Kuka AGV shown in Figure 1.8 is another redundantly actuated mobile platform based on omni-directional wheels.

Powered Caster Wheeled (PCW) base redundant robotic platform has been presented by Oetomo [14]. In the paper, a mobile platform with 3 PCW was presented and it was proved that for any omnidirectional mobile platform with powered caster wheels, a singularity-free workspace can be achieved throughout when there is at least two sets of completely actuated wheels i.e., minimum 4 actuators are needed. Chung [15] has proposed a mobile platform with two passive and two PCW configuration which also needs four actuators. Li [8] presented a four PCW based mobile platform which uses 6 motors. Design proposed by [16, 17] uses 6 PCW, which means there are 12 actuators.

Omni-directional wheeled robots are not suitable for uneven or dirty floor encountered in factory environments. Hence powered castor wheeled based robots are preferred on factory floors, as they use conventional wheels [18]. PCW use minimum of 4 actuators. With increasing number of actuators the control becomes increasingly complicated. We propose 3 actuators based wheeled mobile robot which use lesser number of actuators than the minimum required for PCW based systems and use of conventional wheels makes it suitable for factory floor. The

proposed design gives the robot the required redundancy which makes it possible to drive it even in case one of its motors fails.

1.1.3 Mathematical modeling

A very comprehensive list of Wheeled Mobile Robots (WMR) using different wheel configuration is given by Muir and Neuman [9]. In the paper, kinematic equations of conventional, omnidirectional and ball wheels were presented. The kinematics of the WMR was derived by combining the kinematic information of individual wheel. Detection of wheel slip based on error in the least square solution was also discussed. Similar issues were addressed by Alexander in [19]. The major difference is that he uses physical friction model in the analysis of over actuated systems where rolling constrains are not satisfied. A seminal work by Champion [20] gives the structural classification of wheeled mobile robots based on the *degree of mobility*, δ_m , and *degree of steerability*, δ_s . It was based on the number of conventional fixed wheels and conventional centered orientable wheels. According to them any WMR fall in one of the 5 categories given by $(\delta_m, \delta_s) \rightarrow (3, 0), (2, 1), (1, 1), (1, 2)$. The configuration and posture kinematic models of each type was derived. Based on dynamic model, the minimal number of actuators required for full maneuverability of each type was presented. Kinematic analysis of omni-directional over-actuated mobile robot was presented in [10]. Two different methods for forward kinematics was also discussed along with singularity analysis. Actuator switching scheme based on load distribution to avoid singularity was also presented.

Dynamic modeling of mobile manipulator can be categorized as: force based, i.e, the Newton -Euler (NE) formulation and energy based as in Euler-Lagrange (EL) equations. Hoostmans [21] used NE method to arrive at the dynamic model of a mobile manipulator that has two links mounted on a mobile platform. Chung [22] used EL method to arrive at the equations of motion for a mobile manipulator. Geometric mechanics was used to adapt Luh and walker [23] algorithm by Boyer and Ali [24] to apply recursive inverse dynamics formulation to wheeled systems.

Orthogonal compliment method utilizes the advantage of NE and EL approach to derive the equations of motion of a multibody system. It uses the fact that the motion can take place only in the null space of the constraint inducing matrix A defined as $Ax = 0$, where x is a vector of independent co-ordinates. The orthogonal compliment of the constraint inducing matrix A is used to eliminate the non-working constraint forces and moments from the equations of motion. Angeles and Lee [25] used the natural orthogonal compliment method to derive the equations of motion for holonomic mechanical systems. In this, orthogonal compliment was derived from the velocity constraints naturally, hence the name. This was used by Angeles [26] and Saha in [27],[28] to derive the equations of motion for a WMR.

The literature listed above presents the dynamic model of wheeled mobile robot under ideal rolling condition of wheels. In practical situation this is not the case. Wheel slip exists both in lateral and longitudinal direction. The automotive industries has extensively studied the effect of wheel slip on the dynamics of the vehicle from the perspective of vehicle handling and instability. In the robotic community study of wheel slip and its effect on the equations of motion has been motivated from the point of view of control for path following and trajectory tracking. Williams [29] and Balakrishna [30] has presented dynamic model of mobile robot with omnidirectional wheels with wheel slip included in the dynamics. The work in [29] has considered both lateral and longitudinal slip at the kinematic constraint level only and the wheel mass and inertia were not included in the derivation of the equations of motion. In [30] the dynamics of wheels are included in the analysis but lateral slip was not considered. A simple dynamic model of a car like robot has been presented by Khan [31]. The model was derived assuming the vehicle as a single mass. The dynamic coupling of wheel motion with platform was neglected. In [30] and [31] Dugoff model [32] was used for modeling wheel-ground friction forces. Dynamic model of a mobile robot with four powered caster wheel has been presented by Lee [33]. The Lagrangian method was used to derive

the equations of motion. Friction force acting at the tire-ground interface was included in the dynamics of the robot. Dynamic model of differential drive robot with wheel slip discussed in [34],[35] did not consider the effect of caster in the dynamic model whereas [36] included the effect of caster wheels in arriving at the dynamics of the mobile robot.

Another major research area is the estimation of slip and friction force acting on the tire. Ojeda [37] presents a method based on motor current measurement, along with GPS data to estimate wheel slippage. Dakhllallah [32] used extended Kalman filter to estimate tire forces and slip angle. Lee [38] presented a method to estimate the maximum tire force in real time based on the wheel speed and vehicle velocity measurements.

1.1.4 Stability of mobile manipulator

Stability of mobile manipulators has been studied by both the vehicular community and the robotics community. The vehicular community has focused on characterizing the lateral rollover of the vehicle as in [39, 40]. The robotic community has discussed the problem from the point of view of motion planning of manipulator and have proposed different stability margins. Dubowsky [41] has studied the motion planning of mobile manipulator for stationary platform. The criterion for stability is that the support point should not loose ground contact. McGhee [42] proposed as shortest distance between the Center of Gravity and the edge of the support polygon projected on a horizontal plane. *Zero moment point* (ZMP) was developed to study the stability of biped mechanism by Vukobratovic et al. [43, 44]. It was later adapted by Ollero [45], Hung et al. [46, 47], and Sugano [48] to examine the stability of mobile manipulators. Furuno [49] proposed the method for planning the trajectory of the nonholonomic mobile manipulator from its end-effector's path considering the dynamic stability. Then ZMP criterion was used as an index for the system stability. Messuri et al. [50] proposed the stability measure called '*Energy Stability Margin*'. This uses minimum work required for

tipping over of the legged vehicle, a measure which is sensitive to the height of centre of gravity. Ghasempoor and Sepehri [51] extended the method of Messuri by including external and inertial loads. *Force-angle stability* measure which is a simple graphical method was proposed by Papadopoulos [52, 53]. The method is applicable to system subjected to both inertial and external forces, operating over even and uneven terrains.

1.1.5 Path tracking

Path tracing algorithm for the control of mobile robot is used to arrive at the mathematical model of a human operator for simulation of tele-operation loop, discussed in chapter 5. Geometry based path tracking algorithms are most intuitive and hence suitable for the present application. The major algorithms in this category reported in the literatures are *pure pursuit* [54], *follow the carrot* [55], *vector pursuit* [56], and *follow the past* [57]. In pure-pursuit [54], the steer angle of the robot is set so that the robot moves in circle to reach a *goal point* on the desired path. The goal point is based on the “Look Ahead Distance”, which is practically the maximum distance one can see from the current vehicle position. The detailed discussion is given in Chapter 5. Corrective action was based on position error of the vehicle, where orientation error was not taken into account explicitly.

In case of “Follow the Carrot” method [55], the steering angle is set proportional to the *orientation error* defined in Figure 1.10. The orientation error is defined as the difference between the current orientation of the vehicle and the orientation required to reach the goal point on the reference path. The proportionality constant is decided based on trial and error.

The two previous geometric path tracking techniques generate steering commands based upon the goal point on the reference trajectory to be traced. Witkin [56] suggested a strategy to use the path orientation and curvature known at the goal point to improve path tracking, such that the vehicle arrived at the goal

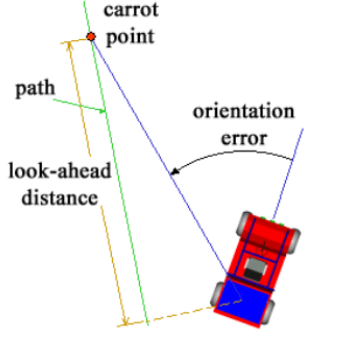


Figure 1.10: Follow the carrot

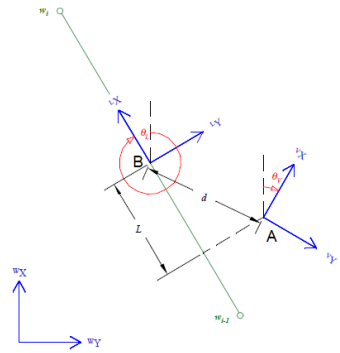


Figure 1.11: Vector pursuit

point with the correct orientation and curvature. Wit used screw theory to find the error between the screw at the current location, point A and the required screw at the goal position, Point B as shown in Figure 1.11. Control is then generated proportional to this error.

Hellstrom [57] has proposed an algorithm which uses the knowledge of previously recorded steer angle, associated with the path traced earlier. In this algorithm, the steer angle of the vehicle is set based on the orientation error, position error and the past recorded steer angle. A recent survey by Paden [58] provides extensive review of other control strategies for path tracking of autonomous unmanned vehicles such as those based on Lyapunov method, Model Predictive Controller, adaptive control, etc.

1.1.6 Obstacle avoidance and path planning

The robotic system developed in this work is not an autonomous mobile robot as it is controlled from the remote station by an operator. In future, it might be required to provide autonomous navigation to the mobile robot. Autonomous navigation has two important ingredients; path planning and obstacle avoidance. In this section, algorithms and techniques that have been proposed by different authors in the field of autonomous navigation are summarized.

The purpose of obstacle avoidance algorithms is to avoid collisions with obstacles. Obstacle avoidance algorithm deals with planning the movement of a

robot based on the information perceived by its sensors, of the surrounding environment. Artificial potential field method proposed by Khatib [59], [60] and discussed in Latombe [61] is one of the oldest method used for obstacle avoidance. It creates a repulsive potential field around the obstacle. The robot is thus pushed off as it approaches the obstacle. Real-Time obstacle avoidance using artificial potential field method has been used in [59],[62],[63]. Virtual Force Field (VFF) method was proposed by Bornstein [64] for real-time obstacle avoidance of a mobile robot. VFF combines potential field method [61] with certainty grid. To compute the certainty grid, the robot work space is divided into a grid and each cell of the grid is given a value based on the chance of the obstacle being located in that cell. The amount of repulsive force acting on the robot is inversely proportional to the distance between the occupied cell and the robot. Borenstein and Koren [65] proposed the Vector Field Histogram (VFH), in this method polar histogram is generated around the robot. The value present in the sectors of the polar histogram show the *polar obstacle density*. The direction of motion of the robot is computed by choosing the sector with least concentration of obstacles. The VFH+ suggested in [66] improves upon the VFH by introducing *threshold hysteresis* generated using a cost function to improve the shape of the trajectory. The Dynamic Window Approach (DWA) [67] is another method for reactive obstacle avoidance, which takes into account the kinematic and dynamic constraints of the vehicle in contrast to VFF and VFH methods. Obstacle avoidance in highly dense and troublesome environment using Nearness Diagram (ND) is presented in [68]. This method uses *divide and conquer* approach splitting the environment into sectors to represent the location of obstacles.

Some of the major path planning methods are the well known **A*** method, Visibility graph, Artificial potential method and Voronoi diagram method [69]. The A* [61] is a heuristic method in which the space is divided into a grid. A collision free path is found by joining the adjacent free cells. A modified version of A* is presented in [70]. Visibility graph method presented in [71], where the

obstacles are represented as convex polygon, a line is joined between the vertices of the polygons with out passing through it. The algorithm generates the path by joining these lines from the robot current location to the goal position. The Voronoi diagram [61, 72, 73] consists of arcs (lines) which are equidistant from the two nearest obstacles. The obstacles in the Voronoi diagram are presented as polygons. The maximized clearance between the Voronoi arc segments and the polygons helps the robot maintain safe distance away from the obstacles.

1.1.7 Tele-operation

Tele-operation deals with connection of a human operator with the robot in order to reproduce human action at a distance. Tele-operation is in general bidirectional or bilateral as the human needs to have a feedback in order to understand the results of his action and to perceive the remote environment. It started with its use in nuclear and space industries [74, 75], but now it is used in underwater exploration, surgery, live-power line maintenance, mining, etc. All characterized by reducing the risk to human operators. One of the major surveys report is by Sheridan [76], where the focus is on supervisory control, human machine interaction and software based teleoperation. The two major research areas in teleoperation is the “human interface ” and “control” design.

1.1.7.1 Human interface

Human interface is a means through which the operator interacts with the remote robot by perceiving the remote environment and sending commands accordingly. Thus, the human interface has two important purpose: one to excite the human senses to show the action of the executed task and to process the human command properly to execute it at the remote end. Force and haptic feedback of remote environment drastically improves operator’s performance. Hence a serial link haptic device PHANTOM [77] was developed at MIT during 1994 to provide 3-DOF force feedback for touch feedback purpose. DELTA Haptice Device de-

scribed in [78] provides 6-DOF force feedback with moderate force. Clover [79] has reported the use of off-the-shelf serial industrial robots for haptic realization of tasks requiring a large workspace and high force capability. Customized 10-DOF haptic device was reported for similar purpose in [80]. Design of a 6-DOF parallel mechanism for force feedback is discussed in [81].

Another major form of human interface is the visual feedback. The main challenge is to provide depth perception of remote environment. Most stereoscopic systems used in telerobotics are based on shutter glasses [82, 83], head-mounted displays [83] or polarized images [84]. Systems based on shutter glasses hide user's eyes alternately in synchronization to screen refreshment, which projects images for left and right eye alternately. A second type of interfaces is based on polarized images. The user is also required to wear glasses that filter the left and right images. The third type of interface is the head mounted display such as "Google cardboard", especially designed to immerse users into virtual environments where the left and right images are projected on each eye using two separate screens or split screens.

1.1.7.2 Control of time delayed teleoperation

Control of a tele-operetion system deals with two issues, *transparency* and *stability*. Transparency deals with what information is to be exchanged between the remote and local station so that the operator can have a natural feel of the remote environment. A position-position architecture is suggested by Goertz [85], where master position is passed as a command to the slave servo (position) controller, and slave position is returned to the master as a position command. A position-force architecture has been proposed by Flatau [86] in which the master sends the position to the slave and the slave sends back the force felt by it in the remote environment. A general 4-channel architecture been suggested by Lawrence [87], and transparency has been defined as a measure of performance in teleoperation and evaluated for different architectures.

An excellent survey article on control of bilateral teleoperation was given by Hokayem and Spong [88]. Few of these are briefly presented here. A teleoperation system, comprised of a master and slave with their corresponding controllers, residing between the human operator and the environment, can be modelled as a two port network. Passivity based design of stabilizing control using wave-variable concept and scattering theory has been proposed by Anderson and Spong [89], Rebelo [90] and Anderson and Slotin [91]. Port-Hamiltonian based approach was used in [92, 93]. Design of a back-stepping controller for time delayed systems based on with partial differential heat equation was studied by Kristic [94].

1.1.8 Predictive display

Delays are inherent in teleoperation over wireless network. Practically, much of the delay is due to relay stations and limited bandwidth of the network. As little as a half second delay in the visual feedback significantly reduces human performance [95]. The operator tends to adopt an inefficient “move then wait and see” policy in order to complete the task.

To overcome performance deterioration of the operator due to time delay in visual feedback, two approaches have been reported in the literature, namely, *supervisory control or tele-assistance* and *predictive display*. In *supervisory control* [96, 97, 98] the operator partly guides the robot by giving intermittent commands to achieve the goal. The drawback of such system is that operator looses direct contact with the task. In predictive display systems, a natural and widely used techniques, synthesised view of the remote environment is displayed to the operator based on his movements. It has been used for space teleoperation as early as in 1993, which was reported by Sheridan [99], Bejczy [100] and Kim [101]. Whereas the above two used a-prior modeling and calibration of remote environment, Jagersand [102] used delayed visual feedback and operator control signal to build predicated image which was presented to the operator. The system was implemented with a fixed remote environment with a manipulator arm with two

wall mounted cameras. An estimation function was proposed $I_i \approx \phi_k(x_i), i \in 1,..k$, that approximated each image I_i seen so far on the trajectory, i.e, $x_1, x_2.....x_k$. Uncalibrated monocular camera mounted on manipulator (eye-in-hand) based image predication method was discussed by Yeres [103] and Deng [104]. Multiple sensors based dense 3-D map of a remote scene was reported by Kelly [105] and [106]. While Kelly used fusion of LIDARr and camera, Burkert used stereo cameras. Hu [107] has used SLAM based Predictive Dispaly (PD) system for telemanipulation of a mobile robot. In this approach, texture and geometry of the remote site was transmitted instead of video stream which reduced bandwidth utilization.

1.2 Research gaps and contributions

The major gap in the area of mobile robots is to design a fault tolerant mobile robot with conventional wheels and with relatively less number of actuators compared to what has been discussed in the existing literatures cited in section 1.1.2. Accordingly, the original contributions of the present research are listed below:

- (i) ***Design of a Redundantly Actuated Redundantly Steered (RARS) teleoperated mobile robot for remote surveillance and mapping application.***

Introduction of the Davis steering mechanism [108] with two differentially driven conventional wheels allowed us to control the robot with three actuators, while having the ability to rescue the robot if one of the motors fails during remote operation.

- (ii) ***Kinematic and dynamic modellings of the RARS robot.***

This RARS mobile robot has a combination of differentially driven rear wheels, and front wheels steered by Davis steering mechanism. Modeling of a redundantly actuated mobile robot including both the longitudinal and lateral slip using NOC approach has been presented for the first time in Section 3.4.3

- (iii) *Synchronised control architecture required for intuitive teleoperation of the RARS mobile robot.*

Since the actuator controlling the Davis steering mechanism needs to be synchronised with differential drive of the rear wheel actuators appropriate control strategy was introduced as described in section 4.2.

1.3 Thesis Organization

The thesis contains eight chapters and three appendix. They are organized as follows:

Chapter 1: Introduction

This chapter, discusses the scope of mobile robotics in general and the motivation which led to this research work. It also includes literature review in the following areas: kinematics and dynamics of mobile robots, control of mobile robot, control for time delay systems, performance of operator under tele-operation, and predictive display systems. Finally the research contribution of this thesis is listed.

Chapter 2: Design of RARS Mobile Robot

This chapter highlights the design considerations of a tele-operated mobile robot based on mission requirements and environmental conditions. It discusses the mechanical design for the traction system, the steering gear, and the scissor mechanism. Selection of steering system based on terrain condition and power requirement is also discussed.

Chapter 3: Kinematics and Dynamics of Wheeled Mobile Robot

In this chapter, the dynamic equations of a four wheeled differentially driven robotic platform derived using natural orthogonal compliment method is presented. The platform has two actuated wheels and two passive wheels. Different types of passive wheels were studied and corresponding dynamic equations were

derived.

Chapter 4: Control of RARS Mobile Robot

The control architecture and the hardware used for tele-operation is presented along with the detailed description of implementation of the controller software at both the remote (mobile robot) and the local station. The experimental results of robots position based on wheel odometry and is torque requirement for few predefined paths are presented.

Chapter 5: Simulation of Tele-operation

In this chapter simulation of a teleoperated mobile robot is presented both without time delay and under time delay due to communication link. It is shown via simulations that with increase in time delay, teleoperation loop become unstable.

Chapter 6: Predictive Display for Time Delay Compensation

In this chapter, we propose a Predictive Display strategy to counter the time delay in video feedback by extrapolating in time the camera view based on the predicted position of the robot at remote location.

Chapter 7: Conclusions

This chapter summarizes major results of this research work. Limitations of the system along with the future scope of work based on present experiences are also addressed.

Bibliography

Appendix A: Measurement of Time Delay in Video Feedback

Here the experimental set up and methodology used to determine the time delay is presented.

Appendix B: Stability of Pure Pursuit under Time Delay

Based on the paper by Ollero [45] stability analysis of pure pursuit tracking algorithm with input delay is discussed.

Appendix C: Optimal Design of Steering Linkages

This appendix describes the formulation of optimization problem for steering linkage.

Chapter 2

Design of the RARS Mobile Robot

Most of the mobile robots presented in literature use differential wheel drive with passive castor as in [27], [109] and [110]. The other common methods for locomotion of mobile robots are the omnidirectional wheels [111] and [112], and tracked wheel system [113] and [114]. According to Nagatani [115], a vehicle with Mecanum wheels is susceptible to slippage and same is the case for tracked vehicle, which are inherently skid steered. The slippage of the wheels prevents the most popular dead-reckoning method using rotary shaft encoders from being performed well.

The major design objective for the mobile manipulator at hand was to make it fault tolerant to single actuator failure. This was important as the mobile manipulator was to move in an environment where human access is prohibited. With the fault tolerant design it could be assured that the mobile manipulator can be extracted from the restricted zone even in case one of its the actuator fails.

The proposed design combines differential drive for the two rear wheels and motorized Davis mechanism for steering the front two passive wheels. This makes the system both Redundant Actuated in traction and Redundantly Steered (RARS). The proposed system has only 3 actuators as compared other redundant wheeled

mobile robots which are having minimum 4 actuators.

In the literature, most common redundantly actuated system are based on either powered caster wheels (PCW) or omnidirectional wheels. One of the first mobile platform the CMU Rover [116, 117], was a PCW based system. Other PCW based robots are presented in [14], [15], [8] and [18]. Mobile robots discussed in [9], [10] and [118] are redundantly actuated systems based on omnidirectional wheels. The RARS design scores over the omnidirectional wheels based system in terms of lesser number of moving parts thus increasing its reliability. Because each omni wheel is made of multiple rollers. Moreover in industrial environment debris can clog the rollers and alter the friction characteristics of the wheels as shown in [119]. The PCW system has issues with singular configuration and wheel locking up the drive system due to improper coordination between steering actuators as discussed in [14] and [120]. Moreover, due to changing orientation of all wheels it becomes difficult for the operator to negotiate obstacles when operated in teleoperation mode.

This chapter discusses kinematic topology and the design methodology of the RARS mobile manipulator. The advantage of Davis steering mechanism is highlighted over castor wheels or other steering methods. The actuator sizing and stability analysis of the RARS mobile robot is also presented.

2.1 Design Overview

The objective of a mobile robot under consideration is to navigate inside the cyclotron vault and collect radiation intensity data at all the required points decided by the operator. Data is to be collected not only at different planer locations of the floor but also at varying height from the floor. To cater to this operational requirement, a mobile platform with a vertically extendable manipulating arm was developed. Together, they are referred henceforth as "mobile manipulator" or simply "mobile platform". The 3-D model of the mobile-manipulator with its

major subsystems are shown in Figure 2.1, whereas and the actual system is shown in Figure 2.2.

The environmental condition required that the vehicle be either autonomous or teleoperated. To keep the complexity low, it was decided to have wireless teleoperated navigation and control. This gives an operator full flexibility to drive and control the system from a remote station using visual feedback provided from the on-board camera. The key parameters of the mobile manipulator are listed in Table 2.1.

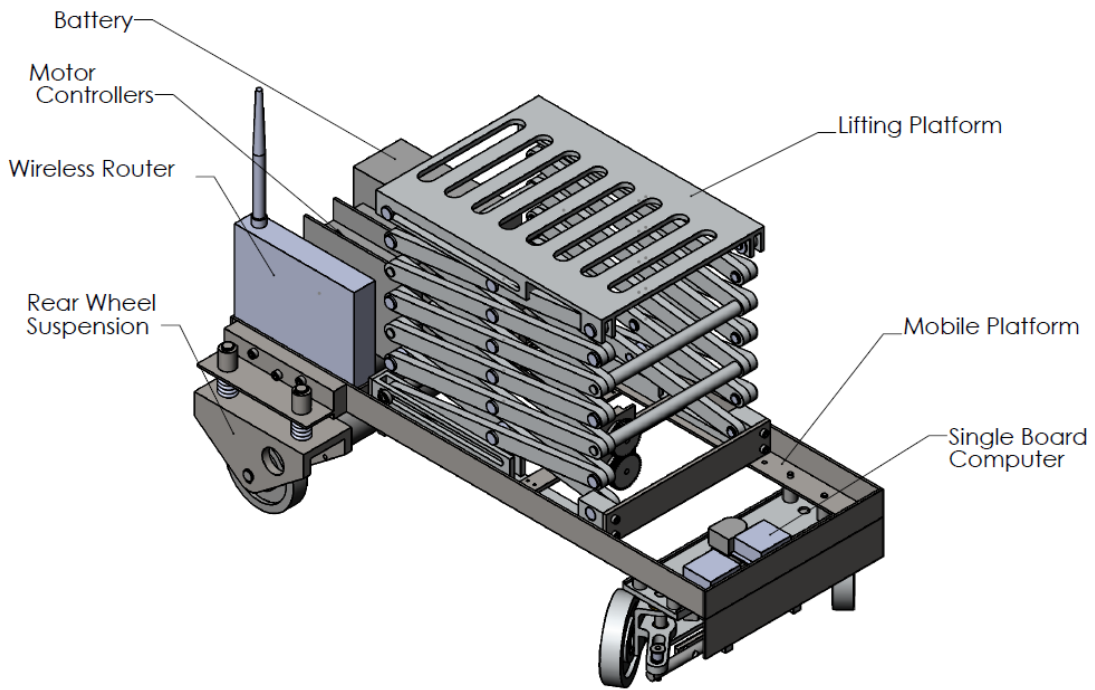


Figure 2.1: 3-D Model of the mobile manipulator

Table 2.1: Key parameters and specifications of the mobile manipulator.

Weight	70 Kg	Without payload
Payload	10 Kg	—
Footprint	700 mm × 400 mm	-
Height Collapsed	500 mm	Along Z-Axis
Height Extended	1500 mm	Along Z-Axis
Steering mechanism	Davis Steering	—
Turning radius	415 mm	—
Ground clearance	45 mm	—
Maximum traction speed	30 m/min	On flat terrain
Ramp climb angle	30°	Platform in retracted position

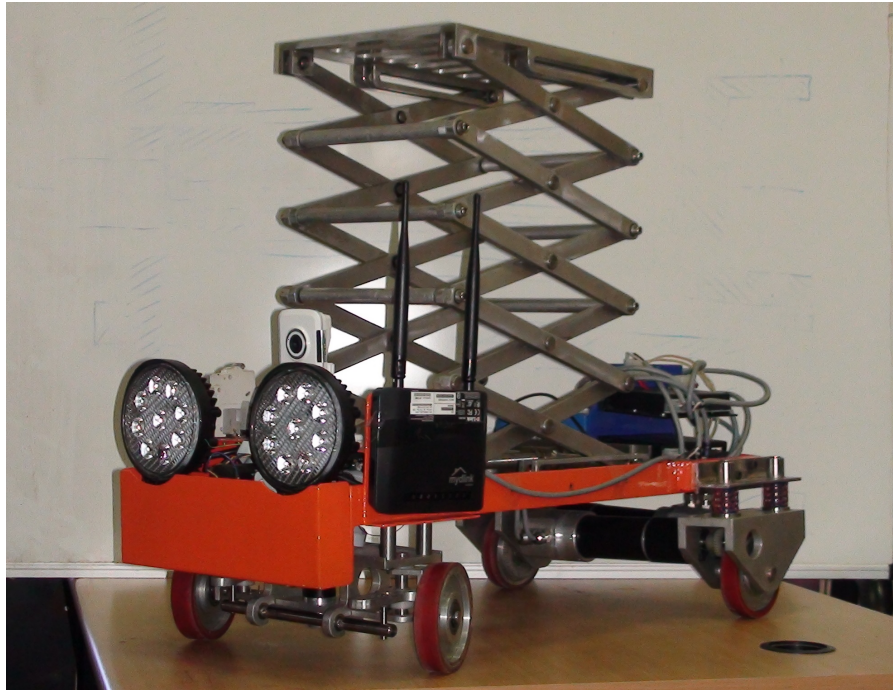


Figure 2.2: Photograph of the actual system

The mobile manipulator has a footprint of 700 mm × 400 mm based on the narrow passage through which the system has to negotiate. These passages are formed inside the vault area by the pipelines and structural supports of the cyclotron and its associated equipment. Two DC motors, with speed servo controller, provide the traction to each rear wheels. The two front wheels are inter-connected with a Davis steering mechanism [108]. A scissor mechanism provides the vertical motion to the detector that is mounted on the manipulating arm.

In order to keep the self weight of the system small, all the structural parts are made of aluminum alloy AL6061, apart from the base frame. Stainless Steel (SS304) angle sections was used for the base frame, which give it excellent strength to weight ratio.

2.2 Kinematic Topology

One of the major requirements of the proposed mobile manipulator was that it should be tolerant to single actuator failure, as mentioned in Chapter 1. The objective was to increases the reliability of the robotic platform. The second

major objective was easy and intuitive manoeuvrability of the platform under teleoperation.

The robot has four wheels arranged in a rectangular configuration. This provides more stability as the support polygon is large with respect to other configuration such as rhombus. The rectangular wheel position layout has another advantage that it is car like, which makes driving intuitive.

The proposed mobile manipulator has two rear wheel driven by two independent motors. The front wheels are passive wheels, steered by a single motor connected through Davis Steering linkage. Thus the total no of actuators used by the mobile platform is three.

This kinematic topology of the RARS robotic platform makes it tolerant to single actuator failure. In case the steering actuator fails, the RARS can be operated as a differential drive robot. The system still has all the required mobility (2-DOF) to bring it to any desired location.

In case one of the rear wheel drive motor fails, it becomes kinematically similar to the bicycle model [20]. The system is still a 2-DOF system. It can be operated in this mode to bring to any desired location.

2.3 Design of the Traction System

Traction is provided by the two rear wheels driven independently. This makes the system over actuated. A mechanical differential connecting the two rear wheels, as used in cars, would overcome this. It was not proposed to do so as the proposed vehicle is planned to be teleoperated in a environment inaccessible to humans. This calls for a single-failure-safe design. The proposed design gives two major advantages. Firstly, in case one of the wheel loosing contact with the ground due to overhang in small pits or while over an obstacle, the mechanical differential system would keep supplying power to the free hanging wheel. The system will hence get stuck, maybe in an unrecoverable location. This situation is avoided in the present

design as the motor having traction can be independently powered, to move the vehicle. Secondly, using the proposed design, in case of one actuator failure, either the traction or the steering motor, still the vehicle can be manoeuvred to a safe location, albeit with dragging of the wheel with failed actuator.

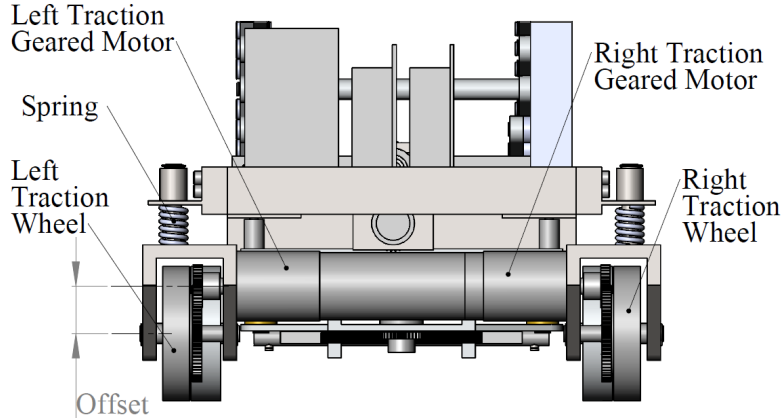


Figure 2.3: Rear suspension

Each wheel is driven by a Maxon DC RE50 200W Motor through a 26:1 reduction gearbox. The motors are mounted at an offset to the wheel axis for increased ground clearance and lateral compactness, as shown in Figure 2.3. Spring suspension is provided at each wheel to ensure sufficient contact force on uneven ground. The diameter of the wheel is 100 mm (D_w), which is sufficient to ride over obstacle of height 20 mm (Max). They are made of Aluminum alloy-6061 with 5mm thick molded polyurethane (PU) liner. The PU liner provides large traction on cement flooring while being resistant to wear.

2.3.1 Stability of mobile manipulator

One of the methods to study stability of dynamic structure is to use *Zero Moment Point* or ZMP introduced by Vukobratovic et al. [43, 44]. It was used for stability analysis of mobile robots as discussed in the literature survey section of this thesis. The idea of ZMP-stabilization is to find a point on the ground where the net moment due to all forces acting on the mobile manipulators is zero. This point is called the ZMP. If the ZMP is inside the *support polygon* then the system is

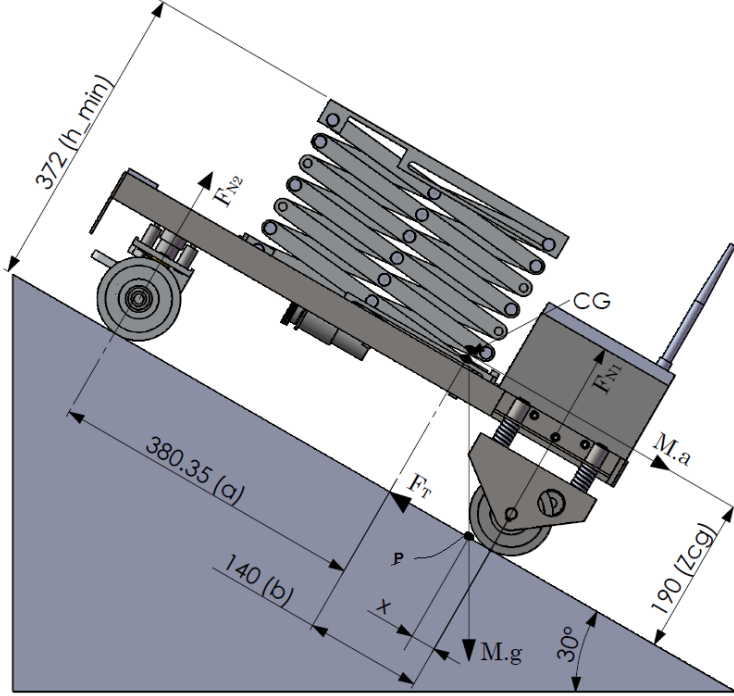


Figure 2.4: Mobile manipulator on slope

stable. A support polygon is a convex polygon formed by joining points of contact of the mobile robot with the ground. The support polygon for the RARS robot is given by $\{O_1, O_2, O_4, O_5\}$ as shown in Figure 2.6. To make the analysis simpler and conservative we will use the rectangular polygon formed by $\{A, B, O_4, O_5\}$ shown by black hash in Figure 2.6.

The two major forces action on a dynamic system is the gravitational force and the inertial forces due to acceleration. They all act at centre of mass of the robot. Therefore the distribution of load becomes very important. From stability point of view the center of mass should be centrally located in the support polygon $\{A, B, O_4, O_5\}$, whereas to generate maximum traction the CG should be close to rear wheel axel, i.e., on side AB of the support polygon. The load distribution was optimized to generate maximum normal reaction, F_n , at the rear wheels without overturning while moving up the ramp of 30° with the manipulator in the collapsed condition as shown in Figure 2.4. Maximizing rear wheel reaction by increasing b , as per Equation 2.1 ensures increased traction, $F_T = \mu F_N$ (μ is the coefficient of friction), but at the same time decreases the stability margin indicated by “x” in

Figure 2.4.

$$F_{N2} = \frac{m_r g \cos \theta}{a + \frac{1}{b}} \quad (2.1)$$

Let p , be the position ZMP located at a distance x form the rear wheel contact point, then we get

$$x(F_{N2} - m_r g \cos \theta + F_{N1}) = (a + b)F_{N2} + m_r(a_l + g \sin \theta)z_{cg} - m_r g b \cos \theta \quad (2.2)$$

Assuming that the *ZMP*, is at the rear wheel contact point, i.e., $x = 0$ the above equation reduces to

$$(a + b)F_{N2} = b(m_r g \cos \theta) - z_{cg}(m_r g \sin \theta + m_r a_l) \quad (2.3)$$

The critical condition, which initiates over turning about the rear axle is given by $F_{N2} = 0$. This reduces the above equation 2.3 to

$$m_r g b \cos \theta = (m_r g \sin \theta + m_r \bar{a})z_{cg}, \quad \Rightarrow g\left(\frac{b}{z_{cg}} \cos \theta - \sin \theta\right) = a_l \quad (2.4)$$

where

F_{N1}, F_{N2} : normal reaction on the front and rear wheels.

a_l : the linear acceleration of the mobile robot along the ramp.

a and b : the distance of the vehicle centre of gravity (CG) from the rear and front wheels.

Z_{cg} : the height of CG from the plane containing the contact point of the wheels.

m_r : mass of the vehicle.

g : acceleration due to gravity.

θ : the inclination of the traction surface from horizontal.

The mass distribution of the mobile robot was adjusted such that the stability margin x as shown in Figure 2.4 was fixed to 30 mm, which limits the acceleration of the mobile robot while climbing up over a ramp of 30° to $a_l = 0.144g$. Operation of system below this acceleration limit safeguards it against overturning along the longitudinal direction.

The stability analysis of the RARS robot on a ramp was carried out with the manipulator in the retracted condition. In case the manipulator is extended the CG of the system shift towards the rear wheel axle. A condition will be reached when the vector M_g crosses the rear wheel contact point, and the mobile robot will overturn. To insure against this unstable situation the vehicle is never moved on the ramp with manipulator extended.

Another instability is encountered during turning or negotiating the curve. The centrifugal force tends to overturn the vehicle in lateral direction as shown in Figure 2.5. If p is the ZMP for this configuration, the location of ZMP, i.e., x is given by Equation 2.5.

$$2dN_3 + \frac{m_r v^2}{R} - m_r gd = x(N_4 + N_3 - M_r g) \quad (2.5)$$

The overturning will start when ZMP reaches the outer boundary of the support polygon that is on the side O_4B or O_3A and N_3 or N_4 becomes zero respectively. This limits the linear velocity of the vehicle for a given steer angle. If v is the linear velocity of the vehicle and R the radius of the path, if the above overturning conditions i.e., $x = 0$ and $N_3 = 0$ are applied to the above equation, we get

$$\frac{m_r v^2}{R} Z_{cg} = m_r gd \quad (2.6)$$

Thus the limiting velocity as a function of R (turning radius)

$$v = \sqrt{\frac{Rgd}{Z_{cg}}} \quad (2.7)$$

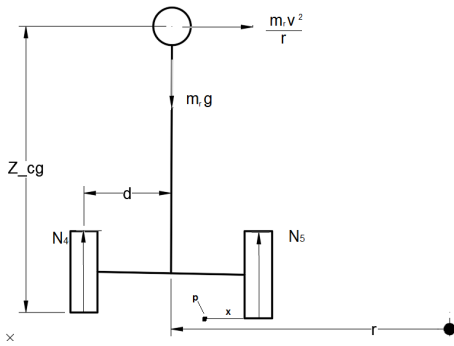


Figure 2.5: Centrifugal forces

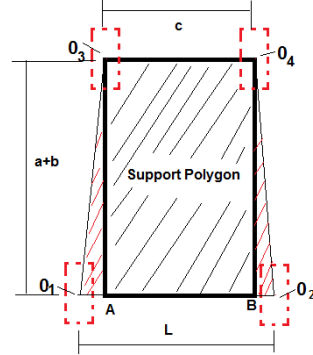


Figure 2.6: RARS support polygon

This sets the limiting velocity as $v = 1.9$ m/sec based on the $Z_{cg} = 190$ mm and $d = 168$ mm as shown in Figure 2.4 and 2.5. Where, R equals the minimum turning radius of the vehicle which is 415 mm as given in Table 2.1.

2.3.2 Selection of motor and gearbox

The torque requirement for the rear wheels were calculated based on the static moment balance with the assumption that each rear wheel shares equal load and the total suspended weight is 80 kg. From the freebody diagram (Figure 2.4), using moment and force balance we get the following:

$$F_{N1} = \frac{aM \cos \theta}{a + b - \mu Z_{cg}}, \quad F_T = \mu F_{N1} \quad (2.8)$$

where, M is the mass of vehicle. In order to estimate the traction motor size, we take worst case scenario of $\theta = 30^\circ$ and $\mu = 0.3$. This leads to

$$F_{N1} = 66 \text{ kg}, \quad F_T = 0.3 \times 66 \approx 20 \text{ kg}$$

Since the traction is provided by the two rear wheels, the torque required per wheel (T_w) is given by

$$T_w = (F_T/2)(D_w/2) = (20/2) \times 50 = 500 \text{ kg-mm} \simeq 5 \text{ Nm} \quad (2.9)$$

The motor torque T_M , required based on the assumption of factor of safety, $FS = 1.5$ is

$$T_M = (FS) \times T_w = 1.5 \times 5 = 7.5 \simeq 8 \text{ Nm} \quad (2.10)$$

Assuming the maximum speed, $V_{ramp} = 1 \text{ m/s}$, of the mobile manipulator over a ramp, the required power, P_M , of the traction motor is calculated as,

$$\begin{aligned} \omega_w &= V_{ramp}/(D_w/2) \simeq 200 \text{ rpm} \\ P_m &= \omega_w T_m = 20 \times 8 = 160 \text{ W} \end{aligned} \quad (2.11)$$

The nearest Maxon motor available as per the catalogue [121] is 200 W, RE50-370354 motor. The nominal speed, N_s is 5680 rpm. Therefore, the gearing ratio required is, $N_s/\omega_w = 5680/200 \simeq 28.4$. The nearest gear box available is of ratio 26 : 1, which was chosen.

2.4 Design of Steering System

The design objective of a steering system should be to ensure rolling motion of all the wheels during every possible manurers of the mobile robot. This is to reduce the friction drag due to sliding motion which degrades the energy efficiency of a mobile robot. In case of four wheeled vehicle, with the orientation of the rear wheels fixed and front wheels steered, the condition shown in Figure 2.7, referred in some literature as Ackerman steering condition, must be satisfied to ensure pure rolling of all the wheels.

This mobile manipulator uses Davis steering mechanism, Figure 2.8, on the front wheels. Caster wheels were not used as they tend to align with obstacles and thus get stuck. On the other hand tracked wheels have excellent rough terrain capabilities, but is power intensive due to skid steering. Another option was to use Omnidirectional wheels, which need complex controller for coordination and an extra actuator. Moreover, the floor of the cyclotron are in general not clean of loose small objects, which may get stuck in between the free rollers of the

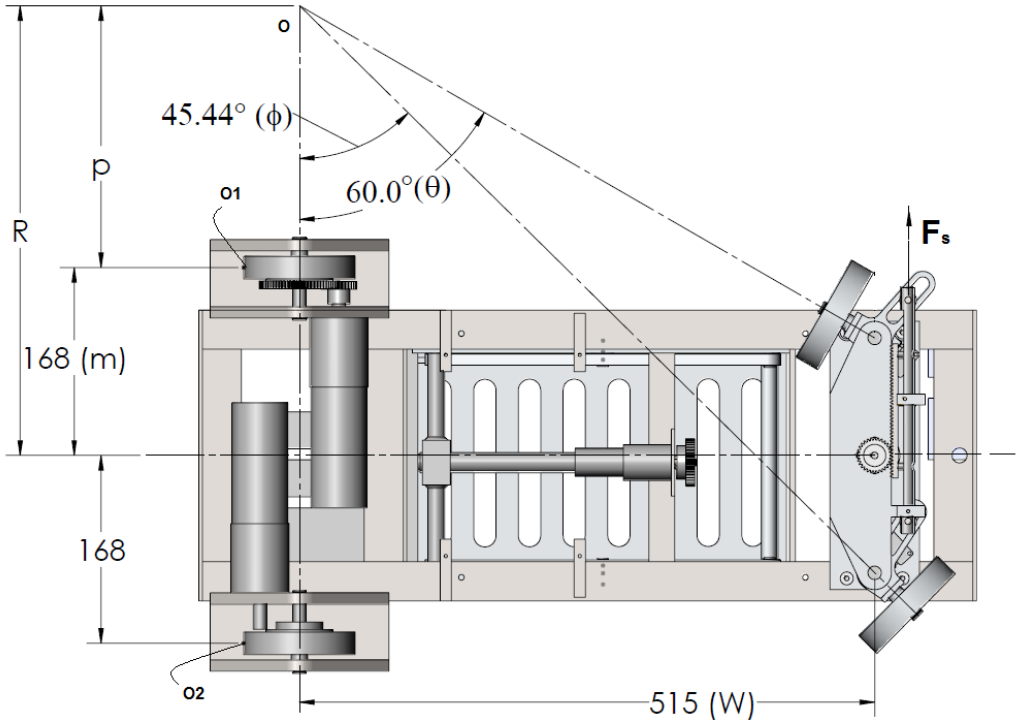


Figure 2.7: Ackerman steering condition

omnidirectional wheels. This will reduce the efficiency of the vehicle.

Davis steering mechanism was chosen over Ackerman steering gear as it satisfies the steering condition given by Equation 2.12, which ensures pure rolling of all wheels, over the entire steering range. This makes the system, suitable for passive wheel odometry and also energy efficient. The steering gear being positively driven by position controlled servo motor does not align with the obstacles and thus are able to crossover it. The dimensions of the links used in the steering mechanism is given in Figure 2.8, and are based on the Ackerman steering law given below:

$$\cot \phi - \cot \theta = a/w, \quad \frac{2b}{h} = \frac{a}{w} \quad (2.12)$$

where a and b is limited by the overall size of the vehicle, discussed earlier.

2.4.1 Minimum turning radius

The mechanical construction of this steering mechanism limits the steering angle. This in turn limits the minimum radius the vehicle can negotiate. The parameters

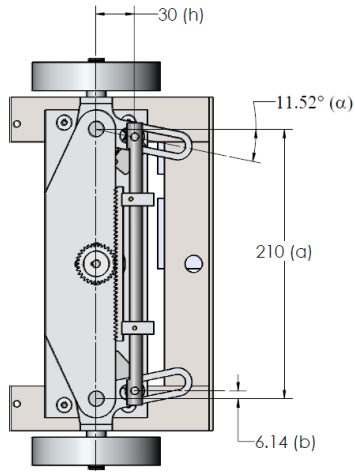


Figure 2.8: Davis steering gear

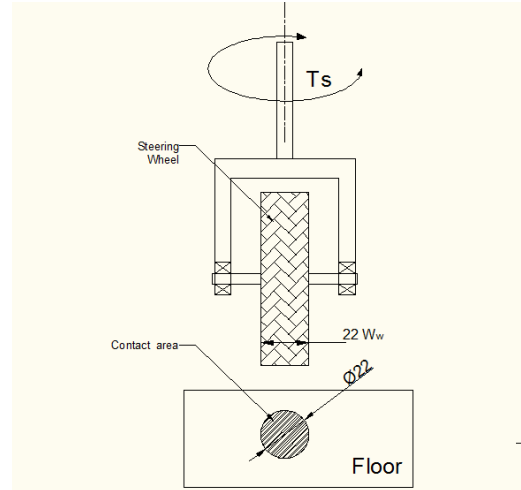


Figure 2.9: Steer torque

of the steering linkages were found using optimization with constraints on overall dimensions and location of links. The details of the method used is given in Appendix C.1. The Figure 2.7 shows the extreme values of ϕ and θ , one side of the steering limits. The **turning radius** R for a given steer angle θ is calculated from the geometry of Figure 2.8 as

$$\tan \theta = \frac{w}{p + m - \frac{a}{2}} \quad \text{and} \quad R = m + p$$

Eliminating p from the above equation and rearranging , we get

$$R(\theta) = \frac{a}{2} + w \cot \theta \quad (2.13)$$

The extreme value of $\theta = 60^\circ$ as shown in Figure 2.7, this gives the *minimum turning radius* R_{min} as

$$R_{min} = \frac{210}{2} + 515 \cot(60^\circ) = 402 \text{ mm}$$

2.4.2 Calculation of steering torque

In order to choose an appropriate steering motor some torque estimate was needed, which is carried out in this section. The torque required to steer the front wheel is estimated based on static equilibrium because the system moves at very slow speed (0.5 m/sec). A simplified assumption was made that the wheel deforms under normal load and the contact area thus generated is circular in shape with diameter that of the wheel width, W_w , as shown in Figure 2.9. In order to estimate the normal reaction on each wheel, we assumed that the total weight of 80kg was equally shared by the four wheels. Therefore, $N_s = 80/4 = 20$ kg. Next, the uniform pressure formula [108] used for brakes/clutches design was applied to find the resistance torque T_s , between the ground and the wheel i.e.,

$$T_s = \frac{N_s \mu}{3} W_w = 0.4 \text{ Nm} \quad (2.14)$$

The resistance torque, T_s , of both the wheels are balanced by the force F_s acting on the rack as shown in Figure 2.7. The rack is coupled to the steering motor by a pinion of diameter, $D_p = 40$ mm. The motor torque, T_{m_s} in Equation 2.15 is calculated with a high factor of safety, $FS = 3$. This is because T_s is estimated based on a simplified model of brake design. The power, P_{m_s} of the steering motor based on torque T_{m_s} and the steering speed ω_s of 100 rpm is

$$T_{m_s} = (FS) \frac{2T_s D_p}{h} = 1.6 \text{ Nm} \quad \text{and} \quad P_{m_s} = T_{m_s} \omega_s = 17 \text{ W} \quad (2.15)$$

Based on the above specifications, a 20W, RE25 DC motor of Maxon make and a gear box GP32 of ratio 159:1 was chosen for the steering mechanism.

2.5 Scissor Mechanism for Manipulator Arm

The manipulating arm was designed to move the radiation sensor mounted on the “*lifting platform*” up to a height of 1.5 m from the floor level. This motion was

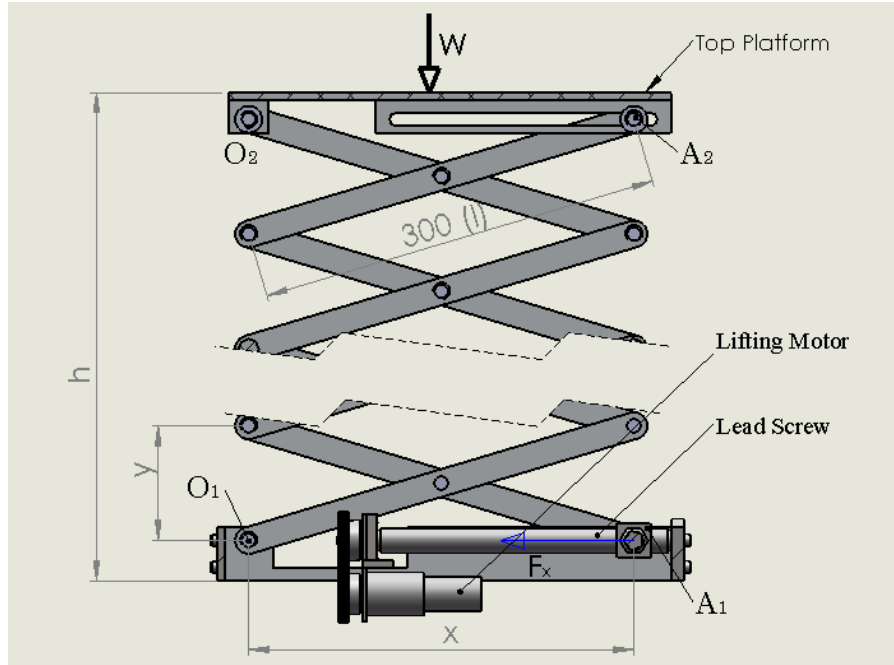


Figure 2.10: Scissor mechanism

generated using a scissor mechanism, shown in Figure 2.10. The scissor mechanism has two major advantages over other lifting methods such as telescopic pillar, screw or belt based linear motion units, etc. First, the ratio of height in extended and collapsed condition is very large. In our case it is 3 : 1. Second, the self weight of the mechanism is less as it is made of links having rectangular cross-section.

The scissor mechanism, Figure 2.10, has 6 stages, where each “X” denotes one stage. The Scissor is connected to the top platform by a pivot joint O_2 and a prismatic joint A_2 , and coupled to the base frame by pivot joint O_1 and a prismatic joint A_1 . The linear actuation of joint A_1 is provided by a lead screw of pitch (P) 1.5 mm and mean diameter (d_m) 10 mm. This results in vertical motion of the top platform.

The relation between the vertical motion of the platform and the horizontal displacement of point A_1 is given by geometry of the mechanism shown in Figure 2.10

$$\begin{aligned}
 y &= l \sin \theta \quad \Rightarrow dy = l \cos \theta d\theta; \\
 x &= l \cos \theta \quad \Rightarrow dx = -l \sin \theta d\theta \\
 h &= Ny \quad \Rightarrow dh = Ndy
 \end{aligned} \tag{2.16}$$

where, l is the link length, θ the angle of the link with horizontal plane, N the number of stages, and h the height of platform.

The number of stages used in the scissor mechanism is six ($N=6$). From the principle of virtual work, we get

$$-F_x dx = W dh, \Rightarrow F_x = \frac{WN}{\tan \theta} \quad (2.17)$$

where, F_x is the axial force on the prismatic joint, A_1 , and W is the payload. From Equation 2.17, it is clear that as $\theta \rightarrow 0$, the force $F_x \rightarrow \infty$. In the present design, $\theta_{min} = 5^\circ$ and $\theta_{max} = 45^\circ$. Therefore, the extended height $h_{max} = Nl \sin \theta_{max} = 1.3$ m and the collapsed height $h_{min} = 156$ mm. Assuming $W = 8$ kg as payload the maximum force $F_x = 342$ kg is required at $\theta_{min} = 5^\circ$.

The motor torque required for the scissor mechanism is calculated using screw jack formula given in [108] and presented here as Equation 2.18.

$$T_L = \frac{F_x d_m}{2} \left(\frac{p + \pi \mu d_m \sec \alpha}{\pi d_m - \mu p \sec \alpha} \right) = 7.5 \text{ Nm} \quad (2.18)$$

where coefficient of friction, $\mu = 0.1$, ACME thread angle, $2\alpha = 60^\circ$, pitch diameter, $d_m = 15$ mm, and pitch, $p = 1.5$ mm, is used. Based on the above specification 10 W, RE20 DC motor with a gear box of 25:1 ratio was chosen from Maxon motor catalogue [121].

2.6 Summary

A customized design of a mobile manipulator taking into consideration the field requirements and floor condition existing inside the cyclotron vault is presented. Requirement of an overactuated system and the advantage of the proposed kinematic design over other redundantly actuated system is discussed. The advantage of scissor mechanism for vertical motion of the sensor over other mechanism is highlighted. Design calculations for motor selection and stability analysis using

ZMP to arrive at the maximum permitted acceleration for the proposed RARS mobile manipulator are presented.

Chapter 3

Dynamics of Wheeled Mobile Robots

In the field of mobile robotics, extensive research has been carried out. Mobile robots can broadly be divided into three categories, namely wheeled robots, legged robots [122], and aerial vehicles [123]. There are few mobile robots which use both wheels and legs for locomotion. For example, Creadapt [124] in order to take advantage of both modes of locomotion. Among these, the most extensively studied are the Wheeled Mobile Robots (WMR). They have been classified into five generic classes by Champion et. al. [20], [125] based on their mobility resulting from the kinematic constraints due to different wheel types. The most common among these are the 3 wheeled differentially driven WMR with one castor wheel. Because of its simplicity in modelling, they have been used in most of the control and motion planning algorithms [126], [127] and [128].

In order to develop a model-based control algorithm, it is imperative to have a good dynamic model of the WMR. These dynamic models are used in simulation software, Software in Loop (SIL) testing and Hardware in Loop (HIL) testing of the controllers. Different methods have been adopted to derive the dynamic model of WMRs. A general dynamical model was derived for three-wheel mobile robots with nonholonomic constraints by B. d'Andrea-Novel [129] using Lagrange

formulation. Alternatively, Thanjavur and Rajagopalan [130] have used Kane's method, and Saha et al. [28],[27] used Natural Orthogonal Compliment (NOC) method for the same.

In this chapter we first present the kinematic model of the mobile robot with two passive wheel at the front. It is then proved using kinematics why a passive wheel with caster offset along the plane of the wheel self orients itself. while casters with zero offset must be actuated. This has not been explicitly presented in literature.

Next the dynamic equation of a mobile robot using Natural Orthogonal Compliment method is derived for both for ideal rolling condition of wheels and in presence of longitudinal and lateral slip of wheels. Use of NOC for modeling differential drive wheeled vehicle under ideal rolling condition as been presented by Angels and Saha [28], [27]. We extend this method to include both the lateral and longitudinal slip of the wheels, and derive the dynamic equations of motion of a mobile robot with redundant actuators.

The RARS robot has a unique drive configuration, which uses both differential drive and Davis mechanism for steering. This system has a redundant configuration and very few literature presents dynamical analysis with slip included in the dynamics. To our knowledge no literature is present, where the concept of NOC has been used to model redundantly actuated mobile robot. The two models are compared using simulation to find the deviation in the path traced by RARS robot under different peak value of co-efficient of friction between the wheel and ground plane.

3.1 Modeling using the Natural Orthogonal Compliment (NOC)

Let us consider a system with n rigid bodies interconnected with different types of joints. Let, f_i be the net force acting at the center of mass (CM) of the i^{th}

body and n_i is the net moment. If m_i is the mass, I_{ci} is the moment of inertia with respect to the CM, c_i is the position vector of the CM and ω_i is the angular velocity of the same body, then equations of motion of the i^{th} rigid body are given by Newton-Euler equations as

$$f_i = m_i \ddot{c}_i \quad \text{and} \quad n_i = I_{ci} \dot{\omega}_i + \omega_i \times I_{ci} \omega_i \quad (3.1)$$

Let us define twist (t) and wrench(w) as

$$t_i \equiv \begin{pmatrix} \omega_i \\ \dot{c}_i \end{pmatrix} \quad w_i \equiv \begin{pmatrix} n_i \\ f_i \end{pmatrix}$$

Note that the wrench w_i acting on the i^{th} body can be decomposed into w_i^w , called the *working component* and w_i^c , the *non-working component*. The working component consists of all the external moments and forces, which imparts/extracts energy to/from the system, e.g., motor actuating torque. The non-working component of the wrench consists of the moments and forces that are used to constrain the motion of the body at the joints. Then, Newton-Euler equations (3.1) can be rewritten in a single matrix equation as

$$M_i \dot{t}_i + W_i M_i t_i = w_i^w + w_i^c \quad \therefore w_i \equiv w_i^w + w_i^c \quad (3.2)$$

where

$$M_i \equiv \begin{pmatrix} I_{ci} & 0 \\ 0 & m_i \tilde{1} \end{pmatrix}, \quad W_i \equiv \begin{pmatrix} \Omega_i & 0 \\ 0 & 0 \end{pmatrix}, \quad \Omega_i \equiv \omega_i \times \tilde{1} \quad (3.3)$$

in which Ω_i , is referred as the cross-product matrix of vector ω_i and $\tilde{1}$ denotes the identity matrix. For details, refer to [26],[131]. If we define

$$M \equiv diag[M_1, M_2, \dots, M_n], \quad W \equiv diag[W_1, W_2, \dots, W_n], \quad t \equiv [t_1^T, t_2^T, \dots, t_n^T]^T$$

and

$$w^j \equiv [w_1^{j^T}, w_2^{j^T}, \dots, w_n^{j^T}]^T, j = c, w$$

then the equations of all the n rigid bodies in the system can be collected and written as a single matrix equation

$$M\dot{t} + WMt = w^c + w^w \quad (3.4)$$

The above equation is referred to as decoupled equations of motion of the system.

The kinematic constraints, both holonomic and non-holonomic (e.g., pure rolling), between two bodies i and j of a system can be expressed as a linear homogeneous system of algebraic equations [26], namely

$$A_i t_i + A_j t_j = 0 \quad (3.5)$$

where A_i, A_j depend on the kinematic parameters.

The constraint equations corresponding to all the joints in the system can be written in terms of the *generalized twist vector* t . Furthermore, if $\dot{\theta} \equiv [\dot{\theta}_1, \dot{\theta}_2, \dots, \dot{\theta}_n]^T$ denote the *independent generalized joint rates*. One can then write t in terms of $\dot{\theta}$ as $t = T\dot{\theta}$. Using the fact, that $\dot{\theta}$ can take any arbitrary value, we get

$$At = 0, \Rightarrow AT\dot{\theta} = 0 \Rightarrow AT = 0 \quad (3.6)$$

The Equation 3.6 indicates that T is the orthogonal complement of A . Since this relation arises naturally, hence the name *Natural Orthogonal Complement*. It can be shown [26] that the non-working wrench w^c lies in the range space of A^T . In view of Equation 3.6, it can be proved that w^c lies in the null space of T^T . Therefore,

$$T^T w^c = 0 \quad (3.7)$$

To eliminate the non-working moments and forces, i.e., w^c from the uncoupled

equation of motion (3.4), we multiply both sides of the equation by T^T ,

$$T^T M \dot{t} + T^T W M t = T^T w^W, \Rightarrow T^T M T \ddot{\theta} + T^T (M \dot{T} + W M T) \dot{\theta} = T^T w^w \quad (3.8)$$

Equation 3.8 represents the dynamic equation of interconnected n -body system. This equation is expressed in terms of the independent generalized joint rates $\dot{\theta}$ and cosponsoring acceleration $\ddot{\theta}$. Further, using the relations $t = T\dot{\theta}$ and $\dot{t} = T\dot{\theta} + T\ddot{\theta}$ in Equation 3.8 the final equations of motion can be written as

$$I(\theta)\ddot{\theta} + C(\theta, \dot{\theta})\dot{\theta} = \tau \quad (3.9)$$

where

$$I(\theta) \equiv T^T M T \quad : \text{generalized inertia matrix}$$

$$C(\theta, \dot{\theta}) \equiv +T^T (M \dot{T} + W M T) \quad : \text{generalized convective inertia matrix}$$

$$\tau \equiv T^T w \quad : \text{generalized vector of driving forces}$$

Where,

$$I(\theta) = \sum_{i=1..n} (T_i^T M_i T_i) \quad (3.10)$$

$$C(\theta, \dot{\theta}) = \sum_{i=1..n} (T_i^T M_i \dot{T}_i + T_i W_i M_i T_i) \quad (3.11)$$

$$\tau = \sum_{i=1..n} T_i^T w_i^w \quad (3.12)$$

3.2 Dynamic Equation of WMR

The dynamic equation of a differentially driven 3 wheeled mobile robot based on the Natural Orthogonal Compliment (NOC) has been presented by Saha [28]. The vehicle consisted of 2 driven wheels and one standard caster wheel. In general, for large vehicles, it is necessary to have at least four wheels from the point of stability of the vehicle. Such a vehicle is shown in Figure 3.1. It may be noted

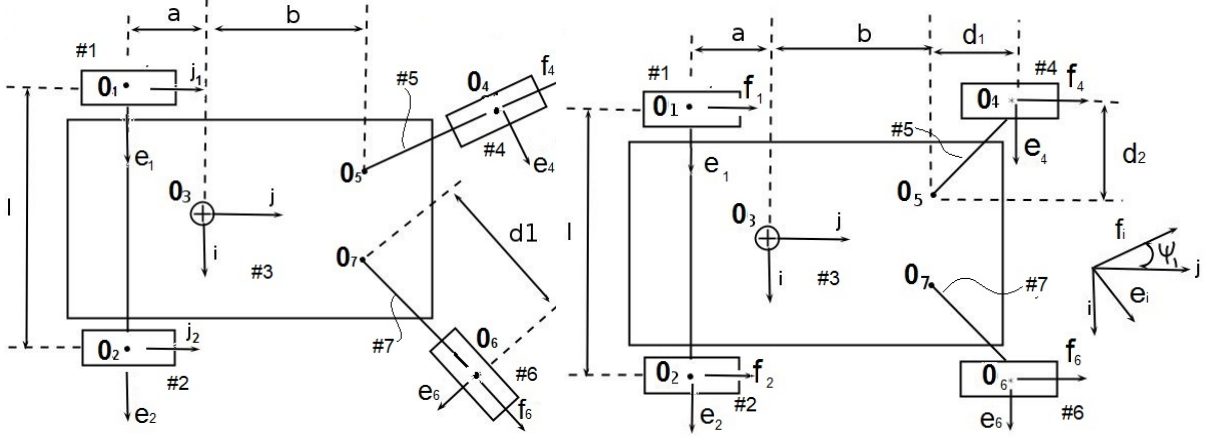


Figure 3.1: WMR-Std. caster

Figure 3.2: WMR-general

that the caster wheels used in this case are the standard caster, where the angle between line O_4O_5 and vector e_4 is 90° . Which is a special case of the more general configuration of the passive wheels shown in figure 3.2, where angle between line O_4O_5 and vector e_4 is not 90°

The vehicle considered for analysis in this chapter is shown in Figure 3.2. It consists of two independently driven wheels at the back and two passive wheels at the front. The actuated wheels are labelled as body #1 and #2 as indicated in Figure 3.2. The platform is body #3. The first caster wheel and its bracket is labelled as #4 and #5 respectively, with the castor pivoted at O_5 . Similarly, the second castor is pivoted at O_7 , and its bracket and wheel are labelled as #6 and #7, respectively, all the wheels are assumed to be rolling without slipping.

The RARS robot wheel configuration can be arrived from the generalized configuration of caster wheels presented above when $d_1 = 0$. Under this condition the and assuming that the steering mechanism always provides the correct steer angle, which is true in case of small curvature paths, the dynamic behaviour of the proposed robot will be similar to that shown Figure 3.2.

3.2.1 Kinematic analysis

In order to proceed with the kinematic analysis of the vehicle in Figure 3.2, we define an orthogonal triad of vectors i, j, k at point O_3 , the control point of the

platform, as shown in Figure 3.2. If $\dot{\theta}_1$ and $\dot{\theta}_2$ (positive when pointing along i) denote the rates of rotation of wheels #1 and #2 then the linear velocity of points O_1 and O_2 under pure rolling condition is given by

$$\dot{o}_i = -r\dot{\theta}_i j, \quad r=\text{radius of wheel} \quad (3.13)$$

The angular velocity of the platform ω_3 can be written as

$$\omega_3 = (r/l)(\dot{\theta}_1 - \dot{\theta}_2)k \quad (3.14)$$

Further, the velocity of point O_3 can be written as $\dot{o}_3 = \dot{o}_i + \omega_3 \times (c - o_i)$, $i = 1, 2$, where o_3 and o_i is the position vector of points O_3 and O_i respectively, with respect to some point fixed to the ground. Eliminating ω_3 one gets the following:

$$\dot{o}_3 = (ar/l)(-\dot{\theta}_1 + \dot{\theta}_2)i - (r/2)(\dot{\theta}_1 + \dot{\theta}_2)j \quad (3.15)$$

Now, the angular velocity of the drive wheel #1 can be expressed as $\omega_1 = -\dot{\theta}_1 i + \omega_3 k$. Using Equation 3.14, the same can be rewritten as

$$\omega_1 = \begin{pmatrix} -i + (r/l)k & -(r/l)k \end{pmatrix} \begin{pmatrix} \dot{\theta}_1 \\ \dot{\theta}_2 \end{pmatrix} \quad (3.16)$$

Similarly for the second wheel (#2) we get

$$\omega_1 = \begin{pmatrix} (r/l)k & i - (r/l)k \end{pmatrix} \begin{pmatrix} \dot{\theta}_1 \\ \dot{\theta}_2 \end{pmatrix} \quad (3.17)$$

Based on Equations 3.13 and 3.16, the twist for wheel #1 in terms of $\dot{\theta}_a \equiv (\dot{\theta}_1, \dot{\theta}_2)^T$, can be written as

$$t_1 = \begin{pmatrix} \omega_1 \\ \dot{o}_1 \end{pmatrix} = \begin{pmatrix} i + (r/l)k & -(r/l)k \\ -rj & 0 \end{pmatrix} \begin{pmatrix} \dot{\theta}_1 \\ \dot{\theta}_2 \end{pmatrix} \quad (3.18)$$

Similarly, for the other actuated wheel #2, one gets

$$t_2 = \begin{pmatrix} \omega_2 \\ \dot{\theta}_2 \end{pmatrix} = \begin{pmatrix} (r/l)k & i - (r/l)k \\ 0 & -rj \end{pmatrix} \begin{pmatrix} \dot{\theta}_1 \\ \dot{\theta}_2 \end{pmatrix} \quad (3.19)$$

To calculate the twist, t_3 of the platform body #3, Equations 3.14 and 3.15 are combined to get

$$t_3 = \begin{pmatrix} \omega_3 \\ \dot{\theta}_3 \end{pmatrix} = \begin{pmatrix} \rho\delta & -\rho\delta \\ r(\lambda i + (1/2)j) & r(-\lambda i + (1/2)j) \end{pmatrix} \begin{pmatrix} \dot{\theta}_1 \\ \dot{\theta}_2 \end{pmatrix} \quad (3.20)$$

where

$$\delta \equiv d/l, \quad \rho \equiv r/d, \quad \lambda \equiv a/l$$

From the above three equations, one gets

$$T_1 = \begin{pmatrix} i + (r/l)k & -(r/l)k \\ -rj & 0 \end{pmatrix}, \quad T_2 = \begin{pmatrix} (r/l)k & i - (r/l)k \\ 0 & -rj \end{pmatrix}$$

,

$$T_3 = \begin{pmatrix} \rho\delta & -\rho\delta \\ r(\lambda i + (1/2))j & r(-\lambda i + (1/2))j \end{pmatrix}$$

In order to calculate the twists of the caster bracket and the caster wheel, it is necessary to express the un-actuated joint rates, $\dot{\psi}_1$ and $\dot{\phi}_1$, in terms of the actuated joint rate vector $\dot{\theta}_a$. Note here that $\dot{\psi}_1$ denotes the rate of rotation of the bracket body (#5) about O_5 with respect to the platform, and $\dot{\phi}_1$ is the rate of rotation of caster wheel body (#4) about its axis e_4 with respect to the bracket.

$$\omega_5 = \dot{\psi}_1 k + \omega_3, \quad \omega_4 = \dot{\phi}_1 e_4 + \omega_5$$

The velocity of O_5 can be expressed in two independent forms, namely, one in

terms of the velocity of O_3 and the other one in terms of the velocity of O_4 , i.e.,

$$\dot{o}_5 = \dot{o}_4 + \omega_5 \times (d_2 e_4 - d_1 f_4), \quad \dot{o}_5 = \dot{o}_3 + \omega_3 \times (bj - mi) \quad (3.21)$$

On equating the above two equations together, and using the rotation matrix (R) between coordinate system $\{i, j, k\}$ and $\{e_4, f_4, k\}$ given Equation 3.22,

$$R = \begin{pmatrix} \cos(\psi_1) & -\sin(\psi_1) \\ \sin(\psi_1) & \cos(\psi_1) \end{pmatrix} \quad (3.22)$$

the equation in terms e_4 and f_4 , is obtained as

$$(-\dot{\phi}_1 r + \dot{\psi}_1 d_1) f_3 + d_3 \dot{\psi}_1 e_3 = \dot{o}_3 + \omega_3 (m \cos \psi_1 - b \sin \psi_1 - d_1) e_4 \quad (3.23)$$

Taking the dot product of the above equation first with e_4 and then with f_4 , and using Equation 3.15 for \dot{o}_3 , one gets

$$\begin{aligned} \begin{pmatrix} d_2 & 0 \\ -d_1 & r \end{pmatrix} \begin{pmatrix} \dot{\psi}_1 \\ \dot{\phi}_1 \end{pmatrix} &= \begin{pmatrix} (-ar/l)S_{\psi_1} + (r/2)C_{\psi_1} + \delta_1 & (ar/l)S_{\psi_1} + (r/2)C_{\psi_1} - \delta_1 \\ (ar/l)C_{\psi_1} + (r/2)S_{\psi_1} + \delta_2 & (-ar/l)C_{\psi_1} + (r/2)S_{\psi_1} - \delta_2 \end{pmatrix} \dot{\theta}_a \\ &= [F_{ij}] \dot{\theta}_a \end{aligned} \quad (3.24)$$

where,

$$\delta_1 = (r/l)(mC_{\psi_1} - bS_{\psi_1} - d_2), \quad \delta_2 = (r/l)(mS_{\psi_1} + bC_{\psi_1} + d_1)$$

Similarly, for the other caster wheel one gets,

$$\begin{aligned} \begin{pmatrix} d_2 & 0 \\ -d_1 & r \end{pmatrix} \begin{pmatrix} \dot{\psi}_2 \\ \dot{\phi}_2 \end{pmatrix} &= \begin{pmatrix} (-ar/l)S_{\psi_2} + (r/2)C_{\psi_2} - \delta_3 & (ar/l)S_{\psi_2} + (r/2)C_{\psi_2} + \delta_3 \\ (ar/l)C_{\psi_2} + (r/2)S_{\psi_2} + \delta_4 & (-ar/l)C_{\psi_2} + (r/2)S_{\psi_2} - \delta_4 \end{pmatrix} \dot{\theta}_a \\ &= [G_{ij}] \dot{\theta}_a \end{aligned} \quad (3.25)$$

where,

$$\delta_3 = (r/l)(mC_{\psi_2} + bS_{\psi_2} + d2), \quad \delta_4 = (r/l)(mS_{\psi_2} + bC_{\psi_2} + d1)$$

The angular and the linear velocity of the CM of the caster wheel #4, is written in terms of the co-ordinate frame fixed to the bracket #5, i.e. $\{e_4, f_4, k\}$, as

$$\omega_4 = \dot{\phi}_1 e_4 + (\omega_3 + \dot{\psi}_1)k, \quad \dot{o}_4 = \dot{\phi}_1 e_4 \quad (3.26)$$

Using Equations 3.24 and 3.14, the twist t_4 can be written as

$$t_4 = \begin{pmatrix} \Theta_4 \\ C_4 \end{pmatrix} \dot{\theta}_a \quad (3.27)$$

Using the definition of $F(i, j)$ in Equation 3.24, Θ_4 and C_4 can be written as

$$\Theta_4 = [F_{11}e_4 + \bar{F}_{21}k \quad F_{12}e_4 + \bar{F}_{22}k], \quad C_4 = r[-F_{11}f_4 \quad -F_{12}f_4]$$

$$\bar{F}_{21} = F_{21} + \rho\delta, \quad \bar{F}_{22} = F_{22} - \rho\delta$$

The angular and the linear velocity of the CM of the caster bracket #5 expressed in the co-ordinate frame fixed to the bracket is given as

$$\omega_4 = \dot{\phi}_1 e_3 + \dot{\psi}_1 k, \quad \dot{o}_4 = \dot{o}_4 + \omega_5 \times [-df_3] \quad (3.28)$$

Using Equations 3.14 and 3.25, the twist t_5 can next be expressed as

$$t_5 = \begin{pmatrix} \Theta_5 \\ C_5 \end{pmatrix} \dot{\theta}_a \quad (3.29)$$

where

$$\Theta_5 \equiv [\bar{F}_{21}k \quad \bar{F}_{22}k], \quad C_5 \equiv d[(1/2)\bar{F}_{21}e_4 - \rho F_{11}f_4 \quad (1/2)\bar{F}_{22}e_4 - \rho F_{12}f_4]$$

In a similar manner, the twists t_6 and t_7 of the other caster wheel and its bracket, respectively can be written as

$$t_6 = \begin{pmatrix} \Theta_6 \\ C_6 \end{pmatrix} \dot{\theta}_a, \quad t_7 = \begin{pmatrix} \Theta_7 \\ C_7 \end{pmatrix} \dot{\theta}_a \quad (3.30)$$

Using $G(i, j)$ defined in Equation 3.25, Θ_6 , C_6 , Θ_7 and C_7 are given by

$$\begin{aligned} \Theta_6 &\equiv [G_{11}e_6 + \bar{G}_{21}k \quad G_{12}e_6 + \bar{G}_{22}k], \quad C_6 \equiv r[-G_{11}f_6 \quad -G_{12}f_6] \\ \Theta_7 &\equiv [\bar{G}_{21}k \quad \bar{G}_{22}k], \quad C_7 \equiv d[(1/2)\bar{G}_{21}e_6 - \rho G_{11}f_6 \quad (1/2)\bar{G}_{22}e_6 - \rho G_{12}f_6] \\ \bar{G}_{21} &\equiv G_{21} + \rho\delta, \quad \bar{G}_{22} \equiv G_{22} - \rho\delta \end{aligned}$$

3.2.2 Special cases

Based on the above kinematic equations 3.24 and 3.25 for the caster wheels two special cases can be recognized one with $d_1 = 0$ and another ($d_2 = 0$). The RARS mobile robot designed fall in the second category and hence it requires a steering actuator as discussed below.

3.2.2.1 Standard caster ($d_1 = 0$)

The standard caster wheel configuration can be obtained by setting the value of $d_1 = 0$. In such condition, the left hand side matrix of Equations 3.24 and 3.25 become a diagonal matrix. Therefore, the first and second row of Equations 3.24 and 3.25 get divided by d_2 and r , respectively. The resulting equations relating the un-actuated joint rate to actuated joint rates are similar to those reported by [28],[26]. These passive wheel are self orienting. Hence there is no need for steering motors.

3.2.2.2 Under-actuated case ($d_2 = 0$)

It can be seen from Equation 3.24 that when the *caster offset*, $d_2 = 0$, the LHS matrix becomes singular. So the unactuated joint rates cannot be determined from $\dot{\theta}_a$. It is therefore essential to have proper caster offset in case we need caster like behaviour from a passive wheel.

An alternative solution is to put an extra actuator to control the bracket motion i.e., $\dot{\psi}_i$. This is the case in Ackerman and Davis steering mechanism, where the steering wheel controls the orientation of the front passive wheels of a car.

3.3 Dynamics with No Wheel Slip

In this section the equations of motion is derived under the assumption that all the wheel satisfies pure rolling condition, there is no slipping or skidding of the wheels. This is valid for vehicles with caster wheels as mentioned in Section 3.2.2.1 or incase where steered wheels are perfectly aligned according to the Ackerman steering condition. Dynamics of such architecture is simple which will lead to a realistic model of RARS developed in this research. This is effectively the case mentioned in Section 3.2.2.2.

Based on the twists calculated in terms of the independent joint rate vector vector $\dot{\theta}_a$, the generalized inertia matrix and the matrix of convective inertia term for the coupled equation of motion 3.9 can be derived

3.3.1 Generalized inertia matrix, I

The equations gives in Section 4.2.1 of the twist of individual body, i.e $t_i = T_i \dot{\theta}_a$ are used to obtain $t = [t_1^T, t_2^T, \dots, t_7^T]^T$ and $t = T \dot{\theta}$ where $T = [T_1^T, T_2^T, \dots, T_7^T]^T$. Since the matrix M is block diagonal, the inertia matrix of the full system denoted by I is given by

$$I = T^T M T = T_1^T M_1 T_1 + T_2^T M_2 T_2 + \dots + T_7^T M_7 T_7 \quad (3.31)$$

Next, the contribution of the rear wheels to the inertia matrix, i.e., I_m is given by

$$I_m = \sum_{i=1,2} T_i^T M_i T_i$$

or

$$I_m = \begin{pmatrix} I_w + (\rho\delta)^2 H + m_w r^2 & -2(\rho\delta)^2 H \\ -2(\rho\delta)^2 H & I + (\rho\delta)^2 H + m_w r^2 \end{pmatrix} \quad (3.32)$$

where

$$M_i \equiv \begin{pmatrix} \tilde{I}_w & 0 \\ 0 & m_w \mathbf{1} \end{pmatrix}, \quad \tilde{I}_w \equiv \begin{pmatrix} I_w & 0 & 0 \\ 0 & H & 0 \\ 0 & 0 & H \end{pmatrix} \quad (3.33)$$

Matrix \tilde{I}_w is the 3×3 moment of inertia matrix of the wheel in co-ordinate frame $\{i, j, k\}$, m_w is mass of the motorized wheels and $\mathbf{1}$ is the 3×3 identity matrix. If the mass of the platform is m_p and its moment of inertia about vector k is I_p , then [26]

$$I_3 = T_3^T M_3 T_3 = I_p (\rho\delta)^2 \begin{pmatrix} 1 & -1 \\ -1 & 1 \end{pmatrix} + m_p r^2 \begin{pmatrix} (1/4) + \gamma^2 & (1/4) - \gamma^2 \\ (1/4) - \gamma^2 & (1/4) + \gamma^2 \end{pmatrix} \quad (3.34)$$

Similarly, if m_c is the mass of the castor wheel and it is assumed to be a solid disk, then the generalized inertia matrix can be written as

$$\begin{aligned} I_c = \sum_{i=4,6} T_i^T M_i T_i &= (m_c r^2 / 4) \begin{pmatrix} 6F_{11}^2 + \bar{F}_{21}^2 & 6F_{11}F_{12} + \bar{F}_{21}\bar{F}_{22} \\ 6F_{11}F_{12} + \bar{F}_{21}\bar{F}_{22} & 6F_{12}^2 \bar{F}_2^2 \end{pmatrix} \\ &\quad + \begin{pmatrix} 6G_{11}^2 + \bar{G}_{21}^2 & 6G_{11}G_{12} + \bar{G}_{21}\bar{G}_{22} \\ 6G_{11}G_{12} + \bar{G}_{21}\bar{G}_{22} & 6G_{12}^2 \bar{G}_2^2 \end{pmatrix} \end{aligned} \quad (3.35)$$

If the mass of the brackets, i.e., body #5 and #7, are small compared to the mass of the caster wheels, then the contributions of $T_5^T M_5 T_5$ and $T_7^T M_7 T_7$ can be neglected.

3.3.2 Matrix of convective inertia term \mathbf{C}

The matrix of convective inertia terms of Equation 3.9 can be broken down into two parts, $T^T M \dot{T}$ and $T^T W M T$. As can be seen from Equations 3.18, 3.19 and 3.20, T_1, T_2, T_3 associated with rear wheels and the platform is constant. Therefore

$$T^T M \dot{T} = 0$$

. The generalized inertia matrix is constant for the rear wheels and the platform, therefore the vector $I_i \omega_i$ is parallel to $\omega_i, i = 1..3$

$$\Rightarrow \omega \times I\omega = 0$$

$$\Rightarrow T^T W M T = 0$$

. This shows that contribution of the rear wheels and the platform to the convective inertia term is zero. Moreover, the mass of the brackets are assumed to be zero, so they also do not contribute to the convective inertia term. Hence

$$C = T^T M \dot{T} + T^T W M T = \sum_{i=4,6} T_i^T M_i \dot{T}_i + \sum_{i=4,6} T_i^T W_i M_i T_i \quad (3.36)$$

The expression for the first term is found by using Equations 3.24, 3.25, 3.27 and 3.30. The terms \dot{F}_{ij} and \dot{G}_{ij} denote the derivatives of the elements of the matrix F and G defined in Equations 3.24 and 3.25 . To find \dot{T}_4 and \dot{T}_6 we have used the fact $\dot{e}_4 = \omega_4 \times e_4$ and $\dot{e}_6 = \omega_6 \times e_6$.

$$\begin{aligned} T^T M \dot{T} &= (m_c r^2 / 4) \left[\begin{pmatrix} 6F_{11}\dot{F}_{11} + \bar{F}_{21}\dot{F}_{21} & 6F_{11}\dot{F}_{12} + \bar{F}_{21}\dot{F}_{22} \\ 6\dot{F}_{11}F_{12} + \dot{F}_{21}\bar{F}_{22} & 6F_{12}^2\bar{F}_{22} \end{pmatrix} \right. \\ &\quad \left. + \begin{pmatrix} 6G_{11}\dot{G}_{11} + \bar{G}_{21}\dot{G}_{21} & 6G_{11}\dot{G}_{12} + \bar{G}_{21}\dot{G}_{22} \\ 6\dot{G}_{11}G_{12} + \dot{G}_{21}\bar{G}_{22} & 6G_{12}^2\bar{G}_{22} \end{pmatrix} \right] \end{aligned} \quad (3.37)$$

The second term of Equation 3.36 i.e, $\sum_{i=4,6} T_i^T W_i M_i T_i$ evaluates to zero, as shown below.

Next, consider passive wheel (#4), using Equation 3.27 and W defined in the Equation 3.3 one gets,

$$T_4^T W_4 M_4 T_4 = [\Theta_4, C_4] \begin{pmatrix} \Omega_4 & 0 \\ 0 & 0 \end{pmatrix} \begin{pmatrix} I_4 & 0 \\ 0 & m_4 \mathbf{1} \end{pmatrix} \begin{pmatrix} \Theta_4 \\ C_4 \end{pmatrix} = \Theta_4 \Omega_4 I_4 \Theta_4 \quad (3.38)$$

To evaluate the above equation, we express all the terms in the coordinate system $\{e_4, f_4, k\}$. Moreover, $\omega_4 = \Theta_4 \dot{\theta}_a$, using definition of Θ_4 from Equation 3.27 we get

$$\omega_4 = (F_{11}\dot{\theta}_1 + F_{12}\dot{\theta}_2)e_4 + (F_{21}\dot{\theta}_1 + F_{22}\dot{\theta}_2)k$$

and the cross product matrix of ω_4 as

$$\Omega_4 \equiv \begin{pmatrix} 0 & -(F_{21}\dot{\theta}_1 + F_{22}\dot{\theta}_2) & 0 \\ (F_{21}\dot{\theta}_1 + F_{22}\dot{\theta}_2) & 0 & -(F_{11}\dot{\theta}_1 + F_{12}\dot{\theta}_2) \\ 0 & (F_{11}\dot{\theta}_1 + F_{12}\dot{\theta}_2) & 0 \end{pmatrix}$$

When the above expressions are substituted in Equation 3.38, we get

$$T_4^T W_4 M_4 T_4 = 0, \Rightarrow T^T W M T = 0 \quad (3.39)$$

Therefore, the matrix of convective inertia term C of Equation 3.9 evaluates to

$$C = (m_c r^2 / 4) \left[\begin{pmatrix} 6F_{11}\dot{F}_{11} + \bar{F}_{21}\dot{F}_{21} & 6F_{11}\dot{F}_{12} + \bar{F}_{21}\dot{F}_{22} \\ 6\dot{F}_{11}F_{12} + \dot{F}_{21}\bar{F}_{22} & 6F_{12}^2\bar{F}_{22} \end{pmatrix} + \begin{pmatrix} 6G_{11}\dot{G}_{11} + \bar{G}_{21}\dot{G}_{21} & 6G_{11}\dot{G}_{12} + \bar{G}_{21}\dot{G}_{22} \\ 6\dot{G}_{11}G_{12} + \dot{G}_{21}\bar{G}_{22} & 6G_{12}^2\bar{G}_{22} \end{pmatrix} \right] \quad (3.40)$$

All the components of Equation 3.9 are now been evaluated, except the τ . These are simply the torques exerted by the actuated wheels. This completes the dynamic model of the WMR with generalized passive wheel configuration.

3.3.3 Simulation

The mobile manipulator proposed in Chapter 3 was modelled as a differentially driven robot. The front wheels and steering mechanism were not included in the dynamic model as their masses are too small compared to the platform. The weight of each wheel is 0.3Kg, the steering mechanism 0.24Kg, whereas the weight of the platform is 70Kg.

In simulation the vehicle reference point O_3 is required to trace a circle of radius 5m. As shown in the Figure 3.3. Let, β be the angle between the line joining point O_3 and O with respect to $X - axis$. The function $\beta(t)$ was defined such that the full circle is completed in 60Sec and the velocity and acceleration of the robot is zero at the beginning ($t=0$) and end of travel ($t=60$).

$$\beta(t) = \frac{20\pi}{60^3}t^3 - \frac{30\pi}{60^4}t^4 + \frac{12\pi}{60^5}t^5 \quad (3.41)$$

The initial pose of the vehicle is parallel to the $Y - axis$ i.e. $\beta = 0$ as shown by dotted line in Figure 3.3.

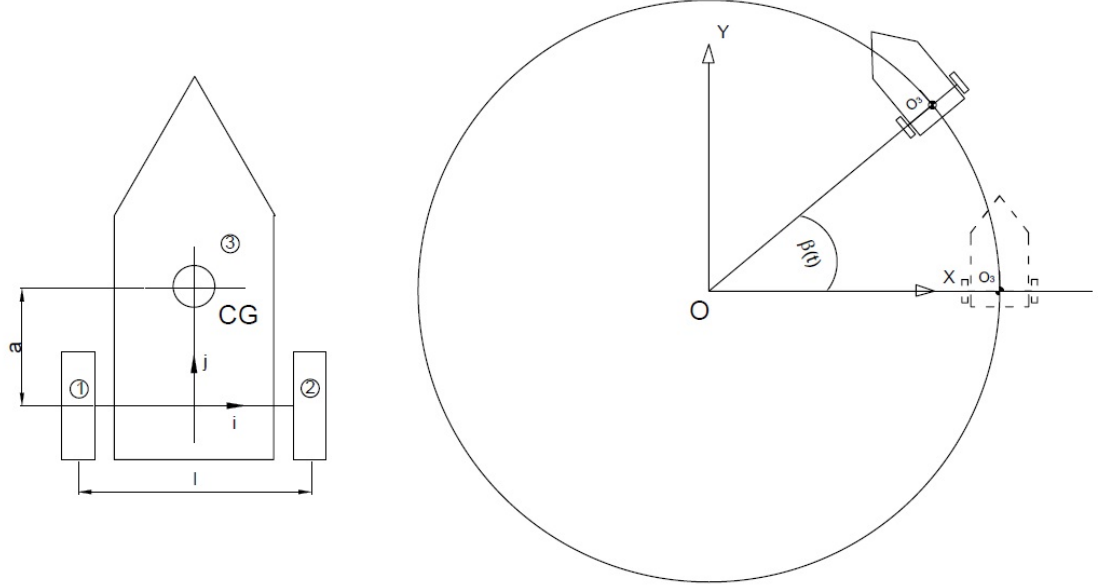


Figure 3.3: Path traced by robot

3.3.4 Inverse dynamics

In order to find the torque required to trace the mobile platform on the circular curve given in Figure 3.3, inverse dynamics was carried out. Using the model's inverse kinematic, the wheel velocity and acceleration were determined using pseudo inverse. The wheel angle, velocity and acceleration were used in the dynamics equation 3.42 to calculate the torque required by each motor. The results are plotted in Figure 3.4.

The equation of dynamic model is given in equation 3.42, where the actuated joints are $\theta_a(t) = (\theta_l, \theta_r)$, the rear left and right wheel rotation angles. The dynamic and kinematic parameters used in the simulation is listed in table 3.1. The rear wheels ($i = 1, 2$) and the platform $i = 3$, twist $t_i^T = T_i\theta_a$, is given by Equations 3.18, 3.19 and 3.20. The dynamic equation is of the vehicle on slope is

given as

$$\begin{aligned}
T^T M T \ddot{\theta}_a &= -T^T(M \dot{T} + W M T) \dot{\theta}_a + T^T(w^J + w^G) \\
\text{where } T &= (T_1^T T_2^T T_3^T)^T, \quad M = \text{diag}(M_1, M_2, M_3) \\
T^T M T &= I_1 + I_2 + I_m + I_3 = I_m + I_3 \\
W &= \text{diag}(W_1, W_2, W_3), \quad w^G = g \sin \alpha, \quad \alpha = 10^\circ
\end{aligned} \tag{3.42}$$

where w^G , w^J and α represent the gravitational force acting along the inclined plane, the external torque applied by a motor and the inclination of the plane to horizontal respectively. The generalized inertia matrix I_m and I_3 are given in Equation 3.32 and 3.34. As stated earlier the convective inertia term is zeros as the inertia matrices are constant. The expression for motor torque is then given as

$$T_1^T w_1^j = \tau_1, \quad T_2^T w_2^j = \tau_2 \tag{3.43}$$

$$T_3^T w^g = \begin{pmatrix} \rho \delta k & r(\lambda i + (1/2)j) \\ -\rho \delta k & r(-\lambda i + (1/2)j) \end{pmatrix} \begin{pmatrix} 0 \\ -j g \sin \alpha \end{pmatrix} = \begin{pmatrix} -\frac{1}{2} r g \sin \alpha \\ -\frac{1}{2} r g \sin \alpha \end{pmatrix} \tag{3.44}$$

Figure 3.4 presents the torques required at the wheels of the vehicle while move up a spiral ramp of slope 10° and radius 5m.

Table 3.1: Dynamic and kinematic parameters

<i>Part Name</i>	<i>Property</i>	<i>Value</i>
Rear Wheels		
m_1, m_2	mass	300g
I_1, I_2	Moment of Inertia	$\text{diag}(242, 242, 465)\text{kg mm}^2$
Base Frame		
m_3	mass	70Kg
I_3	Moment Of Inertia	$\begin{pmatrix} 1.18 & 0.01 & -0.05 \\ 0.01 & 1.28 & 0.08 \\ -0.05 & 0.08 & 0.53 \end{pmatrix} \text{Kg} - \text{m}^2$
l	length	400mm
r	wheel radius (r)	50mm
a	see Figure 3.3	220 mm

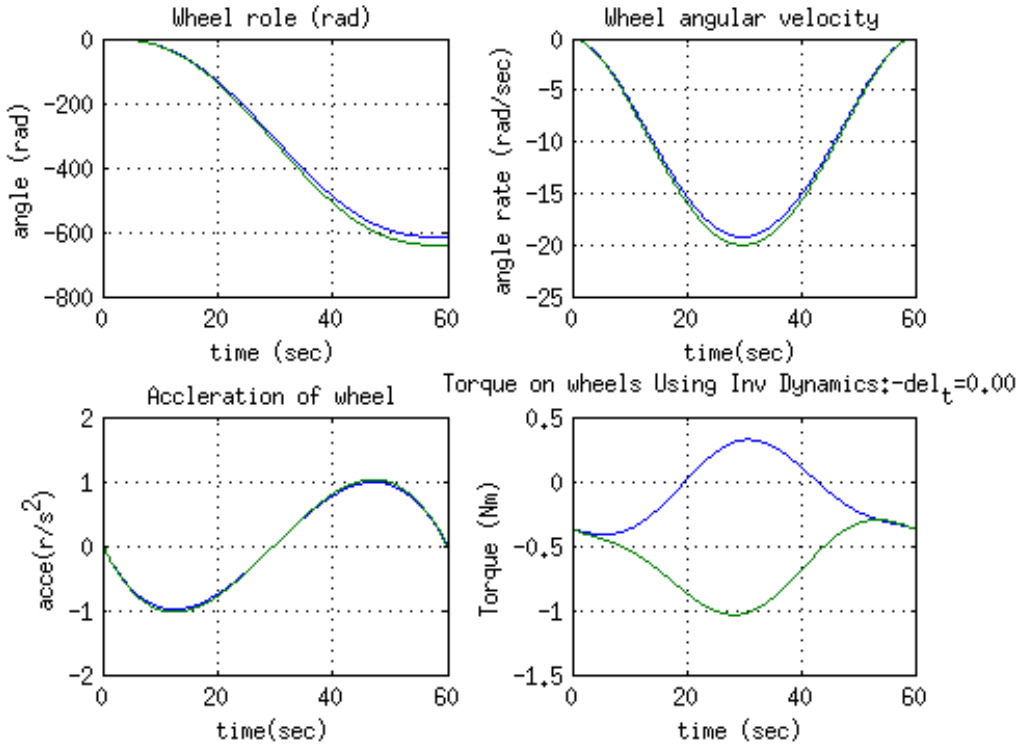


Figure 3.4: Inverse dynamics of the mobile robot

3.4 Dynamics with Wheel Slip

The above section presented the equations of motion of a mobile robot based on the no slip condition between the ground and the wheel, i.e. pure rolling condition. For RARS robot presented in this thesis the front steering wheels are passive but actively steered. Hence, the assumption of pure rolling condition of these wheels are no longer valid. Therefore, both the longitudinal slip and lateral slip (also called skid) are introduced in derive the equations of motion for RARS.

3.4.1 Defining Slip

Longitudinal slip occurs when the peripheral velocity of the wheel at the point of contact with respect to the ground, $\dot{\phi}r$ is different from the linear velocity v_l of the wheel C.G., as shown in Figure 3.5, where, $\dot{\phi}$ is the angular rate of the wheel and r is the effective radius of the wheel. Under pure rolling assumption $\dot{\phi}r = v_l$. However, this is not the case for a deformed wheel. The wheel slipping can be

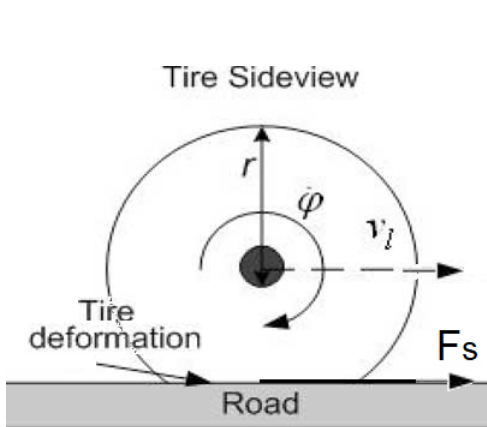


Figure 3.5: Longitudinal slip [132]

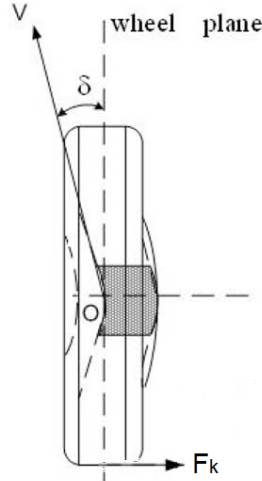


Figure 3.6: Wheel skid [132]

characterized by slippage (or Slip ratio)

$$\rho = \frac{\dot{\phi}r - v_l}{\max(\dot{\phi}r, v_l)}$$

that has a range of $\rho \in [-1, 1]$. The case $\rho = 0$ indicates no wheel slippage whereas $\rho = 1$ implies a complete slippage, i.e., the wheel is not moving linearly despite its angular rotation. In normal road condition, the wheel's slippage (ρ) is usually in the range, $-1 < \rho < 1$. The longitudinal force (F_s) acting on the wheel due to slip is related to the slip ratio ρ . There are several adhesions models proposed that gives relation between the slip ratio and friction force at wheel-ground interface. One of the well known adhesion relations is the *magic formula* presented by Pacejka [133] which is used extensively in automotive industry to modeling tire forces. Other friction models proposed in literature are by Claeys [134], Kulakowski [135] and Dugoff [136].

Lateral slip also called **skidding** is experienced when the wheel moves perpendicular to its plane. This is general encountered during cornering. This lateral movement is called skidding. The skidding produces frictional force perpendicular to the wheel plane as shown in Figure 3.6 by F_k . The force F_k is related to the slip angle δ , which is the angle formed between the wheel plane and the velocity vector of the wheel, when projected on the ground plane. The force F_k can again

be found using magic formula [133] given in Equation 3.45 or any other adhesion model. Where instead of the slip ratio we use the slip angle as the independent parameter.

$$Y(x) = D \sin[C \arctan Bx - E(Bx - \arctan(bx))] \quad (3.45)$$

3.4.2 Kinematics with wheel slip

Figure 3.7 shows the line diagram of the RARS robot. Even though the actual RARS robot uses Davis linkage for steering the front wheels, here let us consider the steer angles ψ_1, ψ_2 corresponding to each wheel. This makes the mathematical modelling more general. In order to simplify the model link connecting the front wheels to the platform, tie rod, etc. associated with the steering mechanism are excluded from the analysis, as their weights are small compared to the platform and wheels. The steering axis is assumed to pass through the center of the front wheel, i.e., the offset is zero. It means $d_1 = d_2 = 0$ (Figure 3.2). Thus, $O_4 = O_5$ and $O_6 = O_7$. In Figure 3.7 O_4 for wheel #4 and O_5 for wheel #5, denotes both the centre of the wheel and also the steering pivot point. The NoC approach was used to derive the equations of motion of the RARS robot with wheel slip taken into account for all the four wheels.

The set of independent variables for this model is given by

$$\dot{\theta} = (\dot{\theta}_1, \dot{\theta}_2, \dot{y}_1, \dot{y}_2, \dot{x}, \dot{\psi}_1, \dot{\psi}_2, \dot{\theta}_4, \dot{\theta}_5)^T \quad (3.46)$$

It may be noted that θ_i, ψ_i is same as defined earlier in Section 3.2. The variables \dot{y}_1, \dot{y}_2 are the linear velocity of centre of the rear wheels, i.e., of points point O_1 and O_2 , in the direction j of the body coordinate system. The lateral slip of the rear wheels are denoted by x_1 and x_2 as shown in the Figure 3.7. Due to rigidity

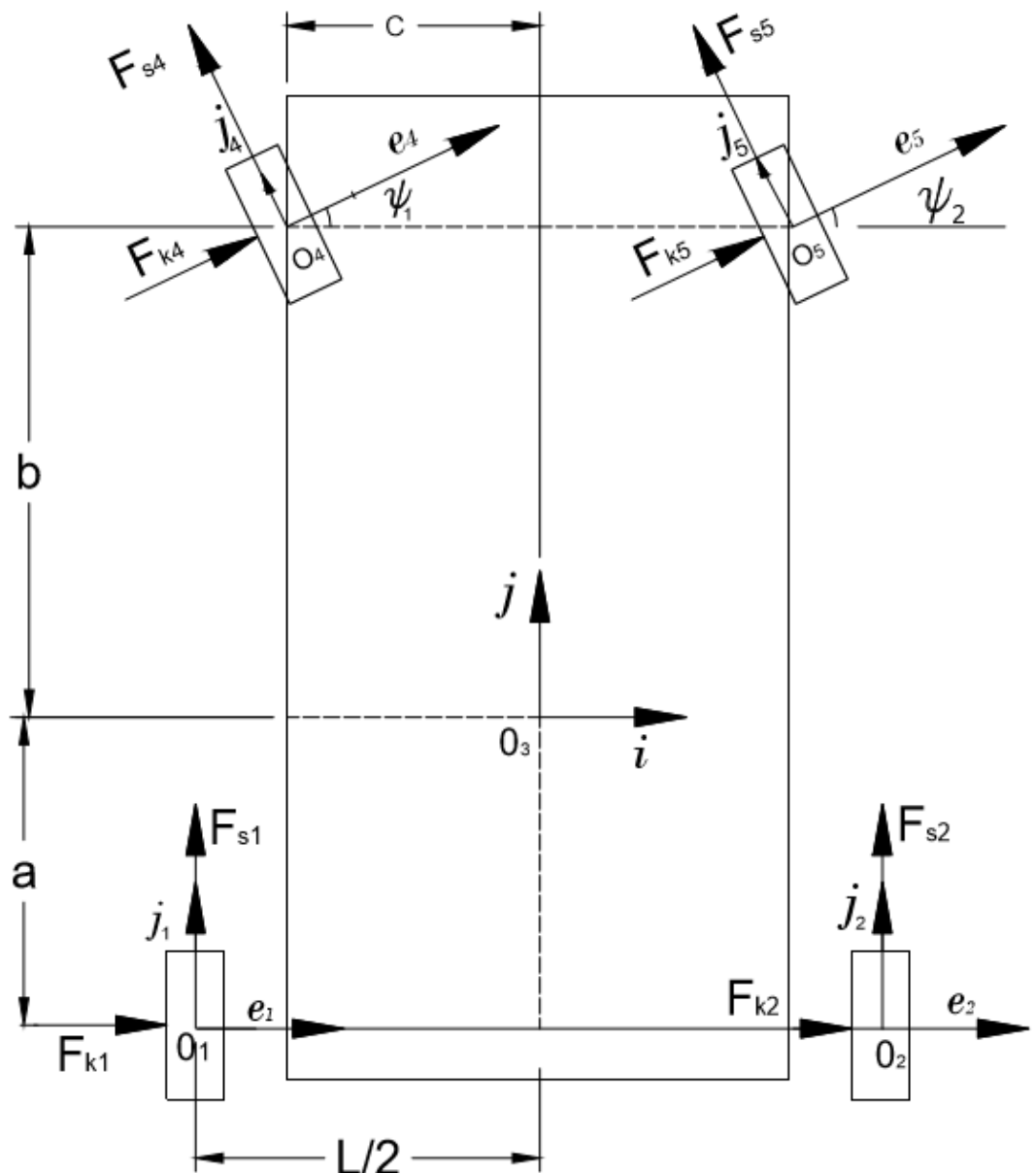


Figure 3.7: Free body diagram of RARS robot

constraints of the rear wheels there are related as follows

$$\dot{x}_1 = \dot{x}_2 = \dot{x}$$

The velocities of points O_1 and O_2 w.r.t the world coordinate X, Y, Z and expressed in the robot's body co-ordinate system i, j, k are given by

$$\dot{o}_1 = \dot{x}i + \dot{y}_1j, \quad \dot{o}_2 = \dot{x}i + \dot{y}_2j \quad (3.47)$$

Equating the velocity of point O_3 expressed in terms of \dot{o}_1 and \dot{o}_2 , one gets

$$\dot{o}_3 = \dot{o}_1 + \omega_3 \times o_1 o_3 = \dot{o}_2 + \omega_3 \times o_2 o_3 \quad (3.48)$$

Let ω_3 be the angular velocity of platform, i.e., body #3. Then

$$\omega_3 = \bar{\omega}_3 k, \quad \bar{\omega}_3 = \frac{\dot{y}_2 - \dot{y}_1}{l} \quad (3.49)$$

Using Equations 3.48 and 3.49 , we get

$$\dot{o}_3 = (\dot{x} + \frac{a\dot{y}_1}{l} - \frac{a\dot{y}_2}{l})i + (\frac{\dot{y}_1}{2} + \frac{\dot{y}_2}{2})j \quad (3.50)$$

The twist t_3 for body #3 is obtained as

$$t_3 = \begin{pmatrix} \omega_3 \\ \dot{o}_3 \end{pmatrix} = T_3 \dot{\theta}, \quad \text{where, } T_3 = \begin{pmatrix} 0 & 0 & -k/l & k/l & 0 & 0 & 0 & 0 & 0 \\ 0 & 0 & ai/l + j/2 & -ai/l + j/2 & 0 & 0 & 0 & 0 & 0 \end{pmatrix} \quad (3.51)$$

or in expanded form

$$T_3 = \begin{pmatrix} 0 & 0 & 0 & 0 & 0 & 0 & 0 & 0 & 0 \\ 0 & 0 & 0 & 0 & 0 & 0 & 0 & 0 & 0 \\ 0 & 0 & -\frac{1}{l} & \frac{1}{l} & 0 & 0 & 0 & 0 & 0 \\ 0 & 0 & \frac{a}{l} & -\frac{a}{l} & 1 & 0 & 0 & 0 & 0 \\ 0 & 0 & \frac{1}{2} & \frac{1}{2} & 0 & 0 & 0 & 0 & 0 \\ 0 & 0 & 0 & 0 & 0 & 0 & 0 & 0 & 0 \end{pmatrix} \quad (3.52)$$

Using the fact

$$\frac{di}{dt} = \bar{\omega}_3 k \times i = \bar{\omega}_3 j, \quad \frac{dj}{dt} = \bar{\omega}_3 k \times j = -\bar{\omega}_3 i, \quad \frac{dk}{dt} = \bar{\omega}_3 k \times k = 0$$

$$\dot{T}_3 = \begin{pmatrix} 0 & 0 & 0 & 0 & 0 & 0 & 0 & 0 & 0 \\ 0 & 0 & -\frac{\bar{\omega}_3}{2}i + \frac{a\bar{\omega}_3}{l}j & -\frac{\bar{\omega}_3}{2}i - \frac{a\bar{\omega}_3}{l}j & 0 & 0 & 0 & 0 & 0 \end{pmatrix} \quad (3.53)$$

The angular velocities ω_1 and ω_2 of wheels #1 and #2 are given as

$$\omega_1 = \dot{\theta}_1 i + \omega_3, \quad \omega_2 = \dot{\theta}_2 i + \omega_3 \quad (3.54)$$

Using Equations 3.47 and 3.54, one gets the twist vector for wheel #1 as

$$t_1 = \begin{pmatrix} \omega_1 \\ \dot{o}_1 \end{pmatrix} = T_1 \dot{\theta} \quad (3.55)$$

$$T_1 = \begin{pmatrix} i & 0 & -k/l & k/l & 0 & 0 & 0 & 0 & 0 \\ 0 & 0 & j & 0 & i & 0 & 0 & 0 & 0 \end{pmatrix} = \begin{pmatrix} 1 & 0 & 0 & 0 & 0 & 0 & 0 & 0 & 0 \\ 0 & 0 & 0 & 0 & 0 & 0 & 0 & 0 & 0 \\ 0 & 0 & -\frac{1}{l} & \frac{1}{l} & 0 & 0 & 0 & 0 & 0 \\ 0 & 0 & 0 & 0 & 1 & 0 & 0 & 0 & 0 \\ 0 & 0 & 1 & 0 & 0 & 0 & 0 & 0 & 0 \\ 0 & 0 & 0 & 0 & 0 & 0 & 0 & 0 & 0 \end{pmatrix} \quad (3.56)$$

and

$$\dot{T}_1 = \begin{pmatrix} \bar{\omega}_3 j & 0 & 0 & 0 & 0 & 0 & 0 & 0 & 0 \\ 0 & 0 & -\bar{\omega}_3 i & 0 & \bar{\omega}_3 j & 0 & 0 & 0 & 0 \end{pmatrix} \quad (3.57)$$

Using Equations 3.47 and 3.54 for wheel #2 the twist vector t_2 is obtained as

$$t_2 = \begin{pmatrix} \omega_2 \\ \dot{o}_2 \end{pmatrix} = T_2 \dot{\theta} \quad (3.58)$$

$$T_2 = \begin{pmatrix} 0 & i & -k/l & k/l & 0 & 0 & 0 & 0 & 0 \\ 0 & 0 & 0 & j & i & 0 & 0 & 0 & 0 \end{pmatrix} = \begin{pmatrix} 0 & 1 & 0 & 0 & 0 & 0 & 0 & 0 & 0 \\ 0 & 0 & 0 & 0 & 0 & 0 & 0 & 0 & 0 \\ 0 & 0 & -\frac{1}{l} & \frac{1}{l} & 0 & 0 & 0 & 0 & 0 \\ 0 & 0 & 0 & 0 & 1 & 0 & 0 & 0 & 0 \\ 0 & 0 & 0 & 1 & 0 & 0 & 0 & 0 & 0 \\ 0 & 0 & 0 & 0 & 0 & 0 & 0 & 0 & 0 \end{pmatrix} \quad (3.59)$$

and

$$\dot{T}_2 = \begin{pmatrix} 0 & \bar{\omega}_3 j & 0 & 0 & 0 & 0 & 0 & 0 & 0 \\ 0 & 0 & 0 & -\bar{\omega}_3 i & \bar{\omega}_3 j & 0 & 0 & 0 & 0 \end{pmatrix} \quad (3.60)$$

Next, the angular velocity of the steered wheel, i.e., body #4, relative to the absolute frame is given as

$$\omega_4 = \dot{\theta}_4 e_4 + \dot{\psi}_1 k + \omega_3$$

The transformation matrix between the Frame $\{e_4, f_4\}$ attached to the wheel #4 is given by the rotation matrix R_4 .

$$R_4 = \begin{pmatrix} \cos \psi_1 & -\sin \psi_1 \\ \sin \psi_1 & \cos \psi_1 \end{pmatrix} \quad (3.61)$$

Then, $e_4 = \cos \psi_1 i + \sin \psi_1 j$ and ω_4 can be written as

$$\omega_4 = \dot{\theta}_4 (\cos \psi_1 i + \sin \psi_1 j) + \dot{\phi}_1 k + \omega_3$$

Linear velocity of point o_4 is given by

$$\dot{o}_4 = \dot{o}_3 + \omega_3 \times \left(-\frac{c}{2}i + bj \right)$$

or in terms of the twist as

$$t_4 = \begin{pmatrix} \omega_4 \\ \dot{o}_4 \end{pmatrix} = T_4 \dot{\theta} \quad (3.62)$$

where

$$T_4 = \begin{pmatrix} 0 & 0 & 0 & 0 & 0 & 0 & 0 & \cos \psi_1 & 0 \\ 0 & 0 & 0 & 0 & 0 & 0 & 0 & \sin \psi_1 & 0 \\ 0 & 0 & -\frac{1}{l} & \frac{1}{l} & 0 & 1 & 0 & 0 & 0 \\ 0 & 0 & \lambda_1 & -\lambda_1 & 1 & 0 & 0 & 0 & 0 \\ 0 & 0 & \lambda_3 & \lambda_2 & 0 & 0 & 0 & 0 & 0 \\ 0 & 0 & 0 & 0 & 0 & 0 & 0 & 0 & 0 \end{pmatrix} \quad (3.63)$$

$$\dot{T}_4 = \begin{pmatrix} 0 & 0 & 0 & 0 & 0 & 0 & 0 & \lambda_4 & 0 \\ 0 & 0 & \lambda_7 & \lambda_6 & \bar{\omega}_3 j & 0 & 0 & 0 & 0 \end{pmatrix} \quad (3.64)$$

$$\lambda_1 = \frac{a+b}{l}, \quad \lambda_2 = \frac{l-c}{2l}, \quad \lambda_3 = \frac{l+c}{2l}$$

$$\lambda_4 = (\bar{\omega}_3 + \dot{\psi}_1)(\cos \psi_1 j - \sin \psi_1 i)$$

$$\lambda_6 = -\bar{\omega}_3(\lambda_1 j + \lambda_2 i), \quad \lambda_7 = \bar{\omega}_3(\lambda_1 j - \lambda_3 i)$$

Next, for wheel #5 one gets

$$\omega_5 = \dot{\theta}_5(R_5 \cdot e_5) + \dot{\psi}_2 k + \omega_3 = \begin{pmatrix} \dot{\theta}_5 \cos \psi_2 \\ \dot{\theta}_5 \sin \psi_2 \\ \dot{\psi}_2 + \frac{-\dot{\psi}_1 + \dot{\psi}_2}{L} \end{pmatrix}$$

Accordingly, the linear velocity of point o_5 is given as

$$\dot{o}_5 = \dot{o}_3 + \omega_3 \times o_3 o_5$$

where,

$$R_5 = \begin{pmatrix} \cos \psi_2 & -\sin \psi_2 \\ \sin \psi_2 & \cos \psi_2 \end{pmatrix} \quad (3.65)$$

Using

$$o_3 o_5 = \frac{c}{2} i + b j$$

along with ω_3 and \dot{o}_3 from Equations 3.49 and 3.50, the following is obtained.

$$\dot{o}_5 = (\dot{x} + y_1(\lambda_1) - y_2\lambda_1) i + (\lambda_2 y_1 + \lambda_3 y_2) j$$

The twist of body #5, i.e., wheel #5 is given as

$$t_5 = \begin{pmatrix} \omega_5 \\ \dot{o}_5 \end{pmatrix} = T_5 \dot{\theta} \quad (3.66)$$

Where

$$T_5 = \begin{pmatrix} 0 & 0 & 0 & 0 & 0 & 0 & 0 & 0 & \cos \psi_2 \\ 0 & 0 & 0 & 0 & 0 & 0 & 0 & 0 & \sin \psi_2 \\ 0 & 0 & -\frac{1}{l} & \frac{1}{l} & 0 & 0 & 1 & 0 & 0 \\ 0 & 0 & \lambda_1 & -\lambda_1 & 1 & 0 & 0 & 0 & 0 \\ 0 & 0 & \lambda_2 & \lambda_3 & 0 & 0 & 0 & 0 & 0 \\ 0 & 0 & 0 & 0 & 0 & 0 & 0 & 0 & 0 \end{pmatrix} \quad (3.67)$$

Using the fact $\dot{e}_5 = (\dot{\psi}_2 + \bar{\omega}_3)k \times e_5 = (\dot{\psi}_2 + \bar{\omega}_3)f_5$, $f_5 = -\sin \psi_2 i + \cos \psi_2 j$ and coordinate system $\{e_5, f_5\}$ is rotated by ψ_2 with respect to coordinate $\{i, j\}$, \dot{T}_5 is given as

$$\dot{T}_5 = \begin{pmatrix} 0 & 0 & 0 & 0 & 0 & 0 & 0 & 0 & \lambda_5 \\ 0 & 0 & \lambda_7 & \lambda_6 & \bar{\omega}_3 j & 0 & 0 & 0 & 0 \end{pmatrix} \quad (3.68)$$

where

$$\lambda_5 = (\bar{\omega}_3 + \dot{\psi}_2)(\cos \psi_2 j - \sin \psi_2 i)$$

3.4.3 Dynamics with wheel slip

The mass inertia matrix M_i of the wheel and platform are same as that used in Section 3.3.1. The generalized inertia matrix is then calculated using T_i derived in Section 3.4.2, as

$$I(\theta) = \sum_{i=1..n} (T_i^T M_i T_i) \quad (3.69)$$

Where the inertial matrix M_i , for $i = 1, 2, 4, 5$ given in Equation 3.33 for each wheel. For platform

$$I_p = \begin{pmatrix} p_{1,1} & p_{1,2} & p_{1,3} \\ p_{1,2} & p_{2,2} & p_{2,3} \\ p_{1,3} & p_{2,3} & p_{3,3} \end{pmatrix}, \quad M_3 = \begin{pmatrix} I_p & 0_{3x3} \\ 0_{3x3} & m_p 1_{3x3} \end{pmatrix}$$

where m_p is the mass of the platform and 1_{3x3} is the identity matrix. The generalized inertia matrix I is then given in terms of the physical parameters of the wheel and platform as

$$I = \begin{pmatrix} I_w & 0 & 0 & 0 & 0 & 0 & 0 & 0 & 0 \\ 0 & I_w & 0 & 0 & 0 & 0 & 0 & 0 & 0 \\ 0 & 0 & \bar{\alpha}_1 & \bar{\alpha}_2 & \bar{\alpha}_3 & -\frac{H}{l} & -\frac{H}{l} & 0 & 0 \\ 0 & 0 & \bar{\alpha}_2 & \bar{\alpha}_1 & -\bar{\alpha}_3 & \frac{H}{l} & \frac{H}{l} & 0 & 0 \\ 0 & 0 & \bar{\alpha}_3 & -\bar{\alpha}_3 & \bar{\alpha}_4 & 0 & 0 & 0 & 0 \\ 0 & 0 & -\frac{H}{l} & \frac{H}{l} & 0 & H & 0 & 0 & 0 \\ 0 & 0 & -\frac{H}{l} & \frac{H}{l} & 0 & 0 & H & 0 & 0 \\ 0 & 0 & 0 & 0 & 0 & 0 & 0 & \bar{\alpha}_5 & 0 \\ 0 & 0 & 0 & 0 & 0 & 0 & 0 & 0 & \bar{\alpha}_6 \end{pmatrix} \quad (3.70)$$

where

$$\bar{\alpha}_1 = \frac{p_{3,3}}{l^2} + m_p \left(\frac{a^2}{l^2} + \frac{1}{4} \right) + \frac{4H}{l^2} + m_w (2\lambda_1^2 + \lambda_2^2 + \lambda_3^2 + 1)$$

$$\bar{\alpha}_2 = -\frac{p_{3,3}}{l^2} + m_p \left(\frac{1}{4} - \frac{a^2}{l^2} \right) - \frac{4H}{l^2} - 2m_w (\lambda_1^2 + \lambda_2 \lambda_3)$$

$$\bar{\alpha}_3 = \frac{am_p}{l} + 2\lambda_1 m_w$$

$$\bar{\alpha}_4 = m_P + 4m_w$$

$$\bar{\alpha}_5 = I_w \cos^2 \psi_1 + H \sin^2 \psi_1$$

$$\bar{\alpha}_6 = I_w \cos^2 \psi_2 + H \sin^2 \psi_2$$

The convective term $C(\theta, \dot{\theta})$ is calculated using the T_i , and \dot{T}_i derived in Section 3.4.2, as

$$C(\theta, \dot{\theta}) = \sum_{i=1..n} T_i^T M_i \dot{T}_i + \sum_{i=1..n} T_i^T W_i M_i T_i \quad (3.71)$$

Introducing the following notions, the explicit expression of Equation 3.71, is obtained below.

$$\delta_0 = m_w \omega_3, \quad \delta_1 = \frac{m_p \omega_3}{2}, \quad \delta_2 = \frac{2a^2}{l^2} \delta_1 + \frac{a \omega_3 p_{3,3}}{l^2}, \quad m_w \omega_3 \lambda_1 (\lambda_2 + \lambda_3)$$

$$\delta_4 = \dot{\theta}_4 (H - I_w) \cos \psi_1 \sin \psi_1, \quad \delta_5 = H \lambda_{4j} \sin \phi_1 + I_w \lambda_{4i} \cos \psi_1 - \frac{\dot{\psi}_1 + \omega_3}{\dot{\theta}_4} \delta_4$$

$$\delta_6 = \dot{\theta}_5 (H - I_w) \cos \psi_2 \sin \psi_2, \quad \delta_7 = H \lambda_{5j} \sin \phi_2 + I_w \lambda_{5i} \cos \psi_2 - \frac{\dot{\psi}_2 + \omega_3}{\dot{\theta}_5} \delta_6$$

$$\delta_8 = \lambda_2 \delta_0 + \lambda_3 \delta_0 + \delta_0 + \delta_1 - \delta_2 \quad \delta_9 = (\lambda_2 + \lambda_3 + 1) \delta_0$$

$$C = \begin{pmatrix} 0 & 0 & 0 & 0 & 0 & 0 & 0 & 0 \\ 0 & 0 & 0 & 0 & 0 & 0 & 0 & 0 \\ 0 & 0 & 0 & -\frac{a\delta_1}{l} - 2\delta_3 + \frac{P_{33}\omega_3}{2l} & \delta_8 & 0 & 0 & -\frac{\delta_4}{l} - \frac{\delta_6}{l} \\ 0 & 0 & 2\delta_3 & \frac{P_{33}\omega_3}{2l} - \frac{a\delta_1}{l} & \delta_8 & 0 & 0 & \frac{\delta_4}{l} + \frac{\delta_6}{l} \\ 0 & 0 & -\delta_9 & -\lambda_3 \delta_0 - \delta_0 - \delta_1 & -\frac{2a\delta_1}{l} - \delta_0 \lambda_2 & 0 & 0 & 0 \\ 0 & 0 & 0 & 0 & 0 & 0 & 0 & \delta_4 \\ 0 & 0 & 0 & 0 & 0 & 0 & 0 & \delta_6 \\ 0 & 0 & 0 & 0 & 0 & 0 & 0 & \delta_5 \\ 0 & 0 & 0 & 0 & 0 & 0 & 0 & \delta_7 \end{pmatrix}$$

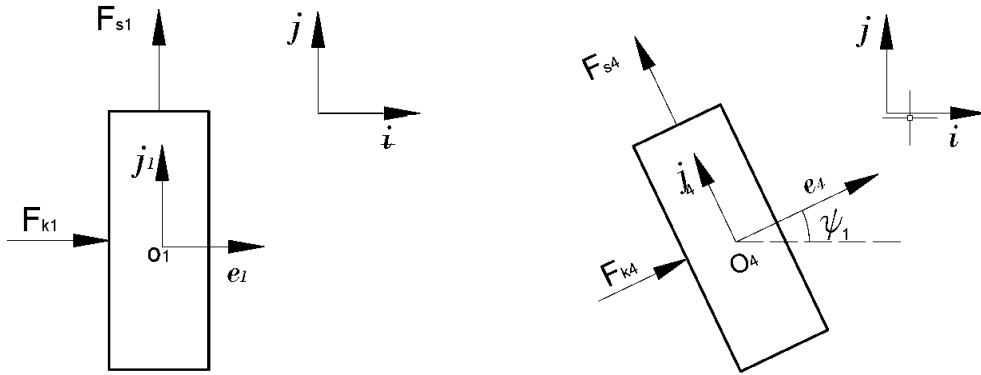


Figure 3.8: External force on rear wheel

Figure 3.9: External forces on front wheel

The wrench τ acting on the system is given as

$$\tau = \sum_{i=1..n} T_i^T w_i^w \quad (3.72)$$

The matrix T_i has allready been calculated in the above section, whereas w_i^w is derived next. The vector, w_i^w is the working wrench acting on the individual bodies. This consists of all the external forces such as actuator force, friction force and gravitational force. The forces acting on wheel 1, as shown in Figure 3.8, are the friction force due to longitudinal slip Fs_1 and frictional force due to lateral slip or skidding, Fk_1 at the ground-wheel interface . The motor torque acting on the wheel 1 is τ_{m1} . Similarly forces acting on wheel 2 are Fs_2 , Fk_2 and τ_{m2} . Therefore, w_1 and w_2 are written as

$$w_n = \begin{pmatrix} \tau_{m,n} i \\ F_{k,n} i + F_{s,n} j \end{pmatrix}, \quad n = \{1, 2\} \quad (3.73)$$

The superscript w has been removed as it is understood that only working forces need to be considered in the formulation below. The front wheels have steering actuation, let the steering torques be represented by $\tau_{s,4}$ and $\tau_{s,5}$ for the wheel #4, and #5. The friction forces on the front steered wheel is shown in Figure 3.9 act along $\{e_4, f_4\}$ and $\{e_5, f_5\}$ for the two front wheels. No traction motor torque is

applied to the front wheels as they are passive. Therefore, w_4 and w_5 are given by

$$w_n = \begin{pmatrix} \tau_{s,n}k \\ F_{k,n}e_n + F_{s,n}f_n \end{pmatrix}, \quad n = \{4, 5\} \quad (3.74)$$

Since no external force is acting on the platform, i.e., body #3,

$$w_3 = 0_{6x1}$$

One can then calculate $T_i^T w_i$, as

$$T_1^T w_1 = \begin{pmatrix} \tau_{m1} & 0 & F_{s1} & 0 & F_{k1} & 0 & 0 & 0 & 0 \end{pmatrix}^T \quad (3.75a)$$

$$T_2^T w_2 = \begin{pmatrix} 0 & \tau_{m2} & 0 & F_{s2} & F_{k2} & 0 & 0 & 0 & 0 \end{pmatrix}^T \quad (3.75b)$$

$$T_3^T w_3 = 0_{9x1} \quad \text{since } w_3 = 0 \quad (3.75c)$$

$$T_4^T w_4 = \begin{pmatrix} 0 & 0 & \alpha_1 & \alpha_2 & \alpha_3 & \tau_{s4} & 0 & 0 & 0 \end{pmatrix}^T \quad (3.75d)$$

$$T_5^T w_5 = \begin{pmatrix} 0 & 0 & \beta_1 & \beta_2 & \beta_3 & 0 & \tau_{s5} & 0 & 0 \end{pmatrix}^T \quad (3.75e)$$

where

$$\alpha_1 = -\frac{\tau_{s4}}{l} + \lambda_1(F_{k4}C_{\phi_1} - F_{s4}S_{\phi_1}) + \lambda_3(F_{k4}S_{\phi_1} + F_{s4}C_{\phi_1})$$

$$\alpha_2 = \frac{\tau_{s4}}{l} - \lambda_1(F_{k4}C_{\phi_1} - F_{s4}S_{\phi_1}) + \lambda_2(F_{k4}S_{\phi_1} + F_{s4}C_{\phi_1})$$

$$\alpha_3 = (F_{k4}C_{\phi_1} - F_{s4}S_{\phi_1})$$

$$\beta_1 = -\frac{\tau_{s5}}{l} + \lambda_1(F_{k5}C_{\phi_2} - F_{s5}S_{\phi_2}) + \lambda_2(F_{k5}S_{\phi_2} + F_{s5}C_{\phi_2})$$

$$\beta_2 = \frac{\tau_{s5}}{l} - \lambda_1(F_{k5}C_{\phi_2} - F_{s5}S_{\phi_2}) + \lambda_3(F_{k5}S_{\phi_2} + F_{s5}C_{\phi_2})$$

$$\beta_3 = (F_{k5}C_{\phi_2} - F_{s5}S_{\phi_2})$$

Therefore, the expression for τ in Equation 3.72 can be written as

$$\begin{aligned}\tau = & (\tau_{m1} \quad \tau_{m2} \quad (F_{s1} + \alpha_1 + \beta_1) \quad (F_{s2} + \alpha_2 + \beta_2) \\ & (F_{k1} + F_{k2} + \alpha_3 + \beta_3) \quad \tau_{s4} \quad \tau_{s5} \quad 0 \quad 0)^T \quad (3.76)\end{aligned}$$

The longitudinal friction force F_{si} for $i = 1, 2, 4, 5$ is given by Equation 3.45 or any other adhesion model, with x as the slip ratio ρ_i defined as

$$x = \rho_i = \frac{\dot{\theta}_i r - \dot{o}_i \cdot \hat{f}_i}{\max(\dot{\theta}_i r, |\dot{o}_i \cdot \hat{f}_i|)}$$

The lateral force F_{ki} for $i = 1, 2, 4, 5$, i.e., the skid forces are given again by adhesion model such as Equation 3.45, where x is the slip angle δ defined in Figure 3.6.

$$x = \delta_i = \tan^{-1}\left(\frac{\dot{o}_i \cdot e_i}{\dot{o}_i \cdot \hat{f}_i}\right)$$

It may be noted that f_i, e_i are unit vectors of the coordinate system defined at each wheel centre and \dot{o}_i are the velocities of wheel centres as shown in Figure 3.8.

3.4.4 Simulation

To study the effect of wheel slip on the mobile robot dynamics, forward dynamics of the mobile robot was carried out. A reduced order of the dynamic equation derived in section 3.2 was used. The order was reduced by neglecting the dynamic effect due to steering motion of the front wheels. The variables ψ_1 and ψ_2 was removed from the set of independent variables. They were directly set at each time step using the relation,

$$\phi_1 = \arctan\left(\frac{(a+b)(\dot{y}_2 - \dot{y}_1)}{\dot{y}_1 L}\right), \quad \phi_2 = \arctan\left(\frac{(a+b)(\dot{y}_2 - \dot{y}_1)}{\dot{y}_2 L}\right)$$

under the assumption $c = L/2$. The total number of independent variables was reduced from 9 to 5. The new set of independent variables are now

$$\dot{\theta}_{red} = (\dot{\theta}_1, \dot{\theta}_2, \dot{y}_1, \dot{y}_2, \dot{x})^T \quad (3.77)$$

The physical parameters used for the mobile robot are same as the one used in simulation of forward and inverse dynamics with ideal rolling condition for the wheels that are listed in Table 3.1. The generalized inertia matrix I_{red} and the convective term C_{red} of the reduced system are given by

$$I_{red} = \begin{pmatrix} 0.00046395 & 0 & 0 & 0 & 0 \\ 0 & 0.00046395 & 0 & 0 & 0 \\ 0 & 0 & 167.399 & -131.899 & 73.3333 \\ 0 & 0 & -131.899 & 167.399 & -73.3333 \\ 0 & 0 & 73.3333 & -73.3333 & 71.00 \end{pmatrix} \quad (3.78)$$

$$C_{red} = \begin{pmatrix} 0 & 0 & 0 & 0 & 0 \\ 0 & 0 & 0 & 0 & 0 \\ 0 & 0 & 0 & -\frac{73.3333(y_2-y_1)}{l} & \frac{35.5(y_2-y_1)}{l} \\ 0 & 0 & \frac{73.3333(y_2-y_1)}{l} & 0 & \frac{35.5(y_2-y_1)}{l} \\ 0 & 0 & -\frac{35.5(y_2-y_1)}{l} & -\frac{35.5(y_2-y_1)}{l} & 0 \end{pmatrix} \quad (3.79)$$

The equations of motion of the reduced system are given by

$$I_{red}\ddot{\theta}_{red} + C_{red}\dot{\theta}_{red} = \tau_{red} \quad (3.80)$$

The τ_{red} is calculated using Equation 3.72 with $i = 1, 2, 3$, where w_i for $i = 1, 2$ are given in Equation 3.73. Earlier $w_3 = 0$ was used as no external wrench was acting on it. In the reduced model case it is assumed that the frictional force acting on the front wheels are directly transmitted to the platform. Therefore, the moment acting about the C.G., of the platform, O_3 is given by

$$\tau_p = (F_{S4} + F_{K4}) \times (-ic + jb) + (F_{S5} + F_{K5}) \times (ic + jb) + T_s \quad (3.81)$$

where F_{Si}, F_{Ki} , $i = 4, 5$ are those explained in Section 3.4.3, T_s is calculated as given in Section 2.4.2. Therefore, w_3 is written as

$$w_3 = \begin{pmatrix} \tau_p \\ F_{S4} + F_{K4} + F_{S5} + F_{K5} \end{pmatrix} \quad (3.82)$$

To evaluate $F_{s,i}$ and $F_{k,i}$ for $i = 1, 2, 4, 5$, which are function of slip ratio or slip angle, Equation 3.83 [30], which is based on adhesion model proposed by [136] was used. A representative Friction-slip curve with the peak friction co-efficient, $\mu_{peak} = 0.1$, is given in Figure 3.10. The longitudinal and lateral friction forces acting on the wheels are given as $F_s = \mu N_i$ where N_i is the normal force action on the wheel due to ground reaction.

$$\mu = \begin{cases} -(\lambda - 0.15) \frac{0.34\mu_{peak}}{0.85} - \mu_{peak}, & -0.15 \leq \lambda \leq -1.00, \\ (\lambda - 0.15) \frac{\mu_{peak}}{0.15} + \mu_{peak}, & -0.15 < \lambda < 0.15, \\ -(\lambda - 0.15) \frac{0.34\mu_{peak}}{0.85} + \mu_{peak}, & 0.15 \leq \lambda \leq 1.00. \end{cases} \quad (3.83)$$

To calculate F_{Si}, F_{Ki} for $i = 4, 5$ spin rate of front wheels $\dot{\theta}_4, \dot{\theta}_5$ are required. This is obtained from Equation 3.84 which represents the dynamics of the front wheels, where r is the radius of wheel and I_w is the inertia of wheel about e_i .

$$I_w \begin{pmatrix} \ddot{\theta}_4 \\ \ddot{\theta}_5 \end{pmatrix} = \begin{pmatrix} F_{s4}r \\ F_{s5}r \end{pmatrix} \quad (3.84)$$

Figure 3.11 shows input torque applied to the two rear wheels for the forward dynamic simulation. This torque profile for the pair of rear wheels was generated by inverse dynamics of the mobile robot presented in Section 3.3.4 to trace a circular path given in Figure 3.3 and represented by Equation 3.41 on a flat surface under the assumption of pure rolling condition of all wheels.

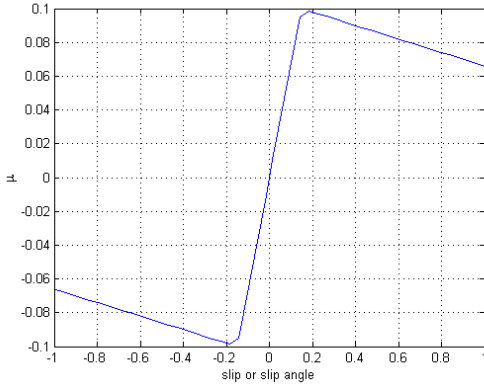


Figure 3.10: Friction model

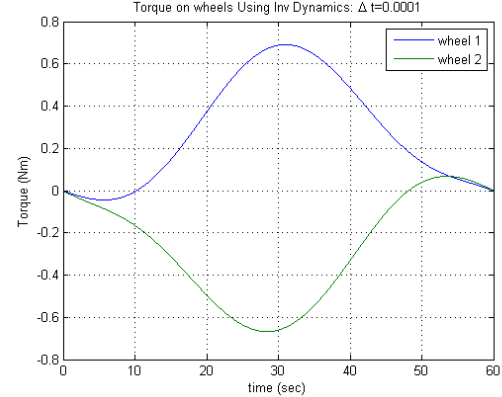


Figure 3.11: Input torque profile

3.4.5 Results and inference

The path traced by the RARS mobile robot with $\mu_{peak} = 0.3$ is shown in Figure 3.12. There is no visible difference between the actual path traced and the given path in terms of lateral shift. If $R_r(t)$ is the actual distance of the robot from the path centre “ O ” and $R = 5\text{m}$ is the radius of the path, the radial deviation, the lateral shift given by $R_r(t) - R$ is shown in Figure 3.14. It is in the range of 10^{-9} , which is effectively zero. This is justified in view of Figure 3.13 which presents the plot of lateral force acting on the vehicle during the period of its motion. The centrifugal force, denoted by green line, tries to shift the vehicle laterally is below the maximum frictional resistance provided by the wheel-surface interface, denoted by the red line. Hence, the net lateral force acting on the mobile robot at any point of time during the motion is zero as indicated by the blue line (not visible in Figure 3.13 as it is covered by the black axis line).

Though the RARS robot maintains the path radius (R) at all time, it is not able to complete the path. The path ends at coordinate $(4.862, -1.166)$ denoted by “End Point” in Figure 3.12 instead of $(5, 0)$. This is because there is equal slip in both the wheels which result in less distance being covered along the given path. If, $\beta(t)$ denotes the position the RARS should have attained at time, t , in actual run, the robot is able to cover only the angle $\beta_r(t)$. Therefore there exists an angular displacement error or phase error, $\beta(t) - \beta_r(t)$, in terms of the circular motion of the robot as shown in Figure 3.15. This error actually indicates that the

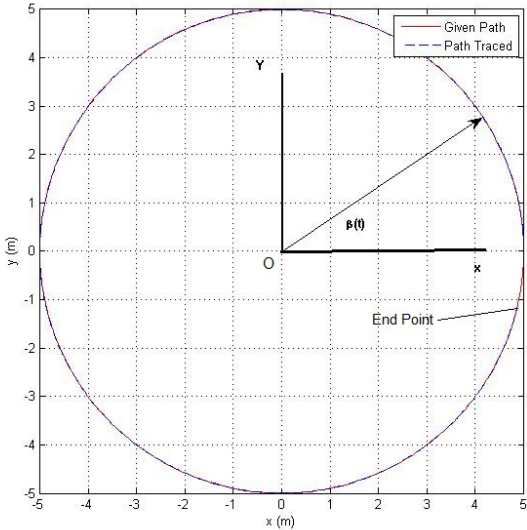


Figure 3.12: RARS path traced when $\mu = 0.3$

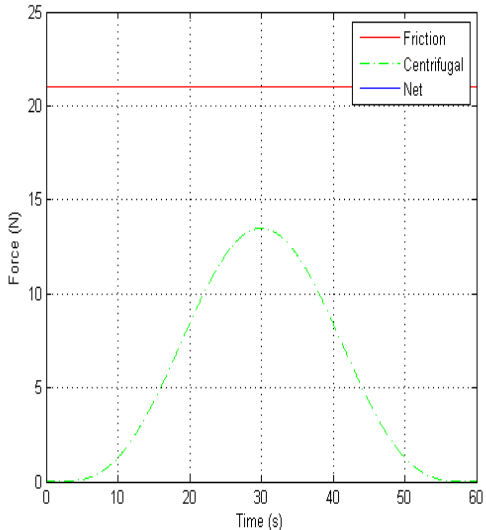


Figure 3.13: Forces on RARS when $\mu = 0.3$

robot has not travelled the distance as required by the given trajectory at time, t . The figure clearly shows that total angular displacement of the robot is less than 350° at the end of 60 sec.

Figure 3.16, shows the trajectory of the RARS robot when the maximum coefficient of friction between the ground and tire is $\mu_{peak} = 0.1$. In this case both lateral, as shown in Figure 3.18 and longitudinal shift, as shown in Figure 3.19, are present. The net lateral force acting on the vehicle, i.e., the blue curve of Figure 3.17 is greater than zero between 20 sec to 40 sec. This lateral force is responsible for the lateral deviation of the actual path traced from the given path. The deviation increases from point “A” to point “B” in Figure 3.16. This is region of the path where the centrifugal force exceeds the frictional force. After point “B” the curve maintains constant radius as the net lateral force acting on the mobile robot again becomes zero.

Note that Figure 3.20 shows the variation of $\beta(t)$ defined in Equation 3.41 and $\dot{\beta}(t)$ with time. Figure 3.17 indicates that the lateral slip initiates at time $t \approx 25$ s when $\mu = 0.1$. This corresponds to angular velocity of $\dot{\beta} = 0.158$ rad/sec as can be read from Figure 3.20 at time $t \approx 25$ s. The linear velocity of the robot to initiate lateral slipping is then given by $R\dot{\beta}$, which is equal to 0.79 m/sec. The robot at

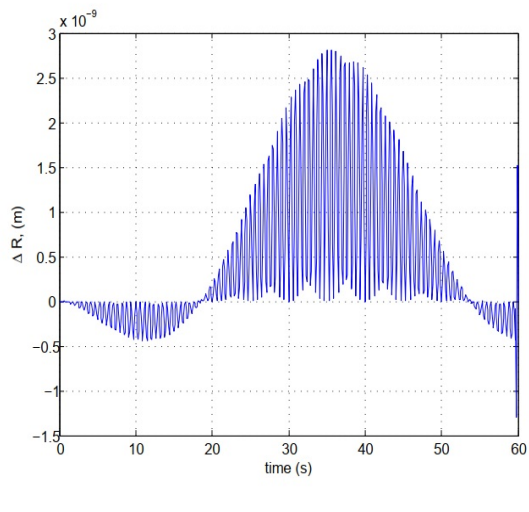


Figure 3.14: RARS, radial deviation
($\mu = 0.3$)

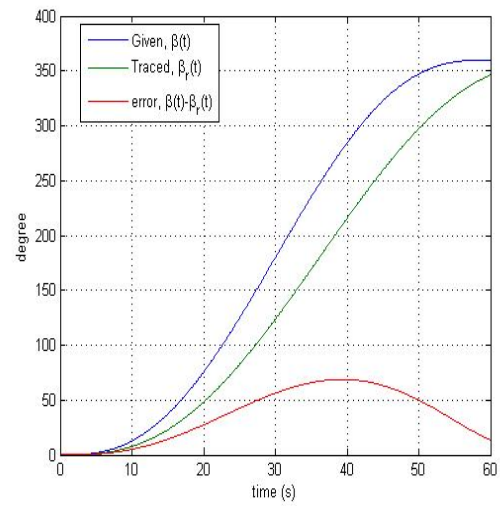


Figure 3.15: Phase and phase error
($\mu = 0.3$)

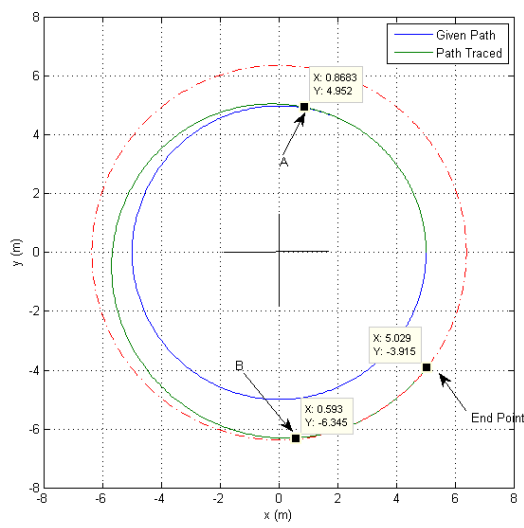


Figure 3.16: RARS path traced when
 $\mu = 0.1$

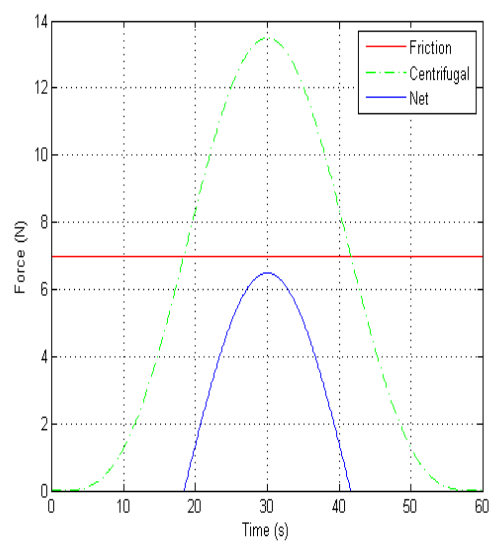


Figure 3.17: Forces on RARS when
 $\mu = 0.1$

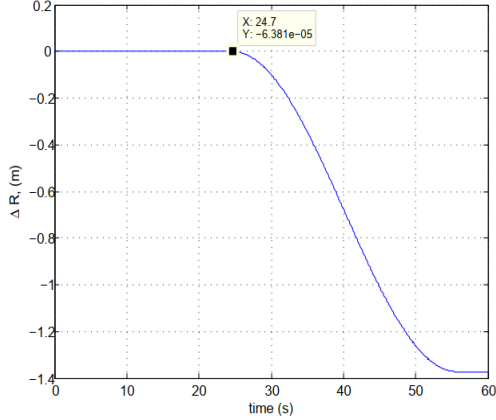


Figure 3.18: RARS radial deviation
($\mu = 0.1$)

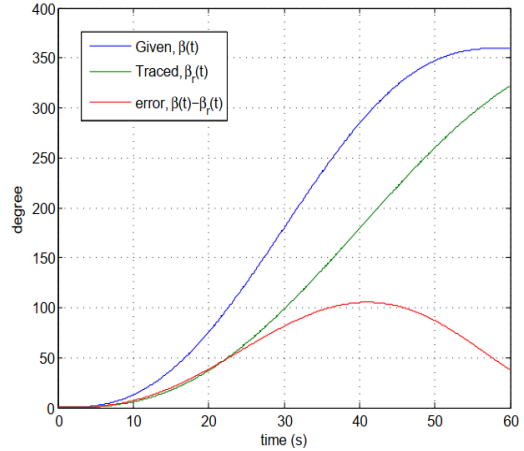


Figure 3.19: Phase and phase error
($\mu = 0.1$)

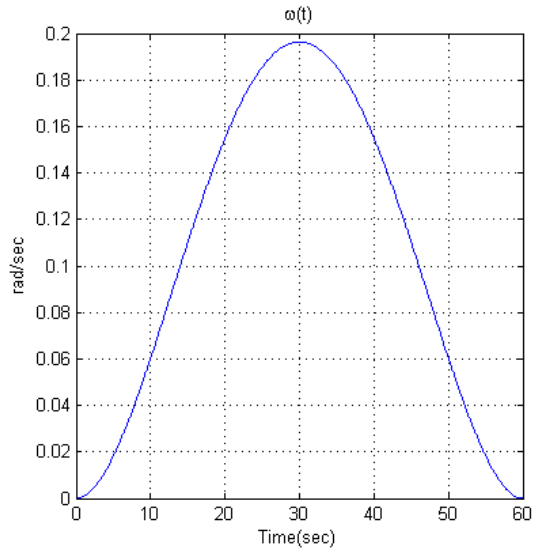
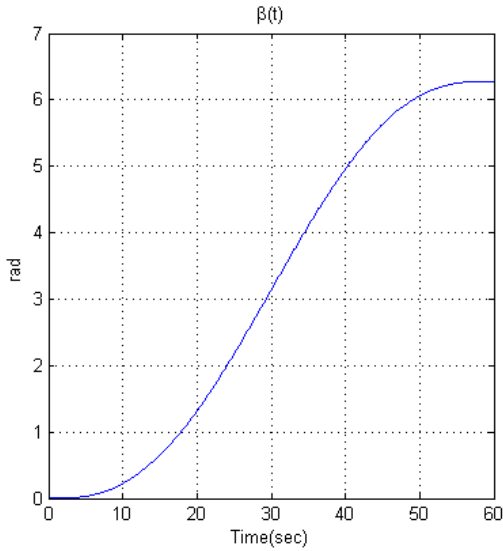


Figure 3.20: Plot of β and $\dot{\beta}$

hand is restricted to the speed of 0.5 m/sec as specified in the robot specification in Table 2.1. The estimated coefficient of friction between the Polyurethane wheel liner and factory floor is around 0.3. Therefore skidding of the mobile robot RARS is unlikely during teleoperation.

3.5 Dynamical Model of Steering System

Typically, the tuning of steering motor is done while the vehicle is stationary. Hence, an independent dynamic model for steering system is essential, which is

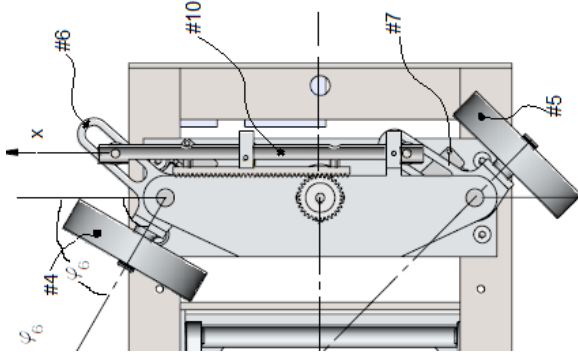


Figure 3.21: Steering assembly

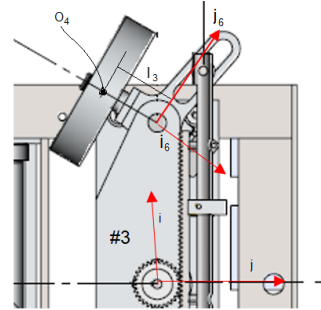


Figure 3.22: Steering linkage

carried out in this section. The steering system is shown in Figure 3.21. The equations of motion were derived under the assumptions, that the vehicle body #3 was at rest and the mass of links #8 and #9 were negligible compared to other links. The kinematic energy of each body except #8 and #9 is derived below.

The kinetic energy of link #6 is given by

$$K_6 = \frac{1}{2}(m_6((x_6^b)^2 + (y_6^b)^2) + I_{6zz})\dot{\phi}_6 \quad (3.85)$$

where, m_6 is the mass, (x_6^b, y_6^b) the coordinate of c.m. expressed in the body coordinate frame $B : \{i_6, j_6, k_6\}$ as shown in Figure 3.22 and I_{6zz} is the moment of inertia in the body coordinate of link #6.

Next we derive the kinetic energy of body # 4, the wheel. The coordinate of c.g of wheel, O_4 in the world $F : \{i, j, k\}$ is given by

$$\begin{pmatrix} x_4 \\ y_4 \end{pmatrix}_F = \begin{pmatrix} -\frac{l}{2} \\ 0 \end{pmatrix} + \begin{pmatrix} \cos \phi_6 & -\sin \phi_6 \\ -\sin \phi_6 & \cos \phi_6 \end{pmatrix} + \begin{pmatrix} -l_3 \\ 0 \end{pmatrix}$$

The linear velocity \dot{O}_4 and its angular velocity ω_6 expressed in the world frame $F : \{i, j, k\}$ is given by

$$\dot{O}_4 = l_6 \dot{\phi}_6 [\sin \phi_6, -\cos \phi_6]^T \quad (3.86)$$

$$\omega_6 = \dot{\phi}_6 k_6 + \dot{\theta}_4 i_6 = [\dot{\theta}_4 \cos \phi_6, \dot{\theta}_4 \sin \phi_6, \dot{\phi}_6]^T \quad (3.87)$$

where, l_6 is the length as shown in Figure 3.22 and $\dot{\theta}_4$ is the spinning rate of the wheel about axis i_6 . Then the kinetic energy of body #4 is given by

$$K_4 = \frac{1}{2} (m \dot{O}_4^T \dot{O}_4 + \omega_6^T [I_6]_F \omega_6) \quad (3.88)$$

$$K_4 = \frac{1}{2} l_6^2 \dot{\phi}_6 m \begin{pmatrix} \sin \phi_6 \\ -\cos \phi_6 \end{pmatrix} \begin{pmatrix} \sin \phi_6 \\ -\cos \phi_6 \end{pmatrix}^T + \begin{pmatrix} \dot{\theta}_4 \cos \phi_6 \\ \dot{\theta}_4 \sin \phi_6 \\ \dot{\phi}_6 \end{pmatrix} [I_6]_F \begin{pmatrix} \dot{\theta}_4 \cos \phi_6 \\ \dot{\theta}_4 \sin \phi_6 \\ \dot{\phi}_6 \end{pmatrix} \quad (3.89)$$

Where $[I_6]_F$ is the inertia matrix of wheel about its c.g. expressed in world frame F . In general the moment of inertia matrix of the body is known in the body frame B , ie $[I_6]_B$. This can be transformed to the world coordinate frame F by using the formula

$$[I_4]_F = R_B^F [I_4]_B [R_B^F]^T$$

where, R_B^F represents rotation transformation matrix between the fixed Frame, F , and the body frame, B . The above Equation, after above transformation can be written as

$$K_4 = \frac{1}{2} (l_3^2 \dot{\phi}_6^2 m_4 + [I_{4xx}]_B \theta_4^2) \quad (3.90)$$

where, I_{4zz} is the moment of inertia of the wheel about its z axis in the body coordinate frame.

The kinetic energy of the tie rod, i.e., body #10, which under goes linear reciprocating motion in a plane is given by

$$K_{10} = \frac{1}{2} m_{10} \dot{x} \quad (3.91)$$

where, x is the displacement of the tie rod and m_{10} is its mass.

The kinetic energy of body #5, i.e., second wheel and second link #7 can be derived in a similar fashion as that of body #4 and #6 respectively. The kinetic energy of body #7 is given as

$$K_7 = \frac{1}{2}(m_7((x_7^b)^2 + (y_7^b)^2) + I_{7zz})\dot{\phi}_7 \quad (3.92)$$

where, m_7 is the mass and I_{7xx} moment of inertia of body #7 .

The kinetic energy of body #5 is given as

$$K_4 = \frac{1}{2}(l_3^2\dot{\phi}_7^2 m_5 + [I_{5xx}]_B\theta_5^2) \quad (3.93)$$

where m_5 is the mass and I_{5xx} moment of inertia of body #5.

From the geometry of Figure 2.8 following relations can be derived

$$\tan(\alpha - \phi_6) = \frac{b+x}{h}, \quad \tan(\alpha - \phi_7) = \frac{b-x}{h} \quad (3.94)$$

$$x_6^b + y_6^b = x_7^b + y_7^b = r_0 \quad (3.95)$$

$$\dot{\phi}_6 = \frac{h\dot{x}}{h^2 + b^2 + 2bx + x^2} = f_1(x)\dot{x}, \quad \dot{\phi}_7 = \frac{h\dot{x}}{h^2 + b^2 - 2bx + x^2} = f_2(x)\dot{x} \quad (3.96)$$

Therefore the total kinetic energy of steering unit is

$$K_s = \sum_{i=4..10} K_i$$

using the expression for K_i and using Equations 4.48, 4.49 and 4.50, the above equation for K_s is written as

$$K_s = \frac{\dot{x}^2}{2} \left(m_{10} + (m_l r_0^2 + I_{zz}) + l_3^2 m_w \right) \left(f_1^2(x) + f_2^2(x) \right) + \frac{1}{2} I_{wxx} \left(\dot{\theta}_4^2 + \dot{\theta}_5^2 \right) \quad (3.97)$$

under the following assumptions

$$l_3 = l_4, \quad m_4 = m_5 = m_w, \quad m_6 = m_7 = m_l, \quad I_{7zz} = I_{6zz} = I_{zz}$$

The Lagrangian in this case is simply the kinetic energy, i.e, $L = K_s$. Since the external forces acts only along the x ordinate, via steering motor. We get

$$F_x = \frac{\partial}{\partial t} \frac{\partial L}{\partial \dot{x}} - \frac{\partial L}{\partial x}$$

or

$$\begin{aligned} F_x = & \ddot{x} \left[m_{10} + (m_l r_o^2 + I_{zz} + l_3^2 m_w) \right] (f_1^2 + f_2^2) \\ & + 2\dot{x}^2 (m_l r_o^2 + I_{zz} + l_3^2 m_w) (f_1 \dot{f}_1 + f_2 \dot{f}_2) + F_1 + F_2 \end{aligned} \quad (3.98)$$

The external force F_1 and F_2 in the above equation is given by

$$F_i = \frac{T_s}{h}, \quad i = 1, 2$$

where T_s is evaluated using Equation 2.14 assuming symmetric loading of both the wheels. The derivative of $f_1(x)$ and $f_2(x)$ is given by

$$\frac{df_1}{dt} = -\frac{2(x+b)h}{(h^2 + b^2 + 2bx + x^2)^2}, \quad \frac{df_2}{dt} = -\frac{2(x-b)h}{(h^2 + b^2 - 2bx + x^2)^2}$$

3.5.1 Design of PID controller

To control the steer angle of the front wheels a computed torque controller [137] was designed. If U denotes the auxiliary control input then F_x is given by

$$\begin{aligned} F_x = & U \left[m_{10} + (mr_o^2 + I_{zz} + l_3^2 m_w) \right] (f_1^2 + f_2^2) \\ & + 2\dot{x}^2 (mr_o^2 + I_{zz} + l_3^2 m_w) (f_1 \dot{f}_1 + f_2 \dot{f}_2) + F_1 + F_2 \end{aligned} \quad (3.99)$$

eliminating F_x using Equation 3.98 and Equation 3.99, we get

$$\ddot{x} = U \quad (3.100)$$

If x_d , is the set point for the displacement of the rack of the steering system and $e(t) = (x(t) - x_d)$ is the position error, we define auxiliary input U as

$$U = -K_d\dot{x} - K_p(x(t) - x_d) - K_i \int e(t)dt \quad (3.101)$$

then Equation 3.100 which represents the overall dynamics of the steering mechanism along with the controller, can be written as

$$\ddot{e}(t) + K_d\dot{e}(t) + K_p e(t) + K_i \int e(t)dt = 0$$

It is be noted that $\dot{e}(t) = \dot{x}$ and $\ddot{e}(t) = \ddot{x}$, since $x_d = const.$. Given that $y_1(t) = \int e(t)dt$ and $Y = [y_1, y_2, y_3]^T$, the above equation can be rewritten in state space

$$\dot{Y} = AY$$

or

$$\begin{pmatrix} \dot{y}_1 \\ \dot{y}_2 \\ \dot{y}_3 \end{pmatrix} = \begin{pmatrix} 0 & 1 & 0 \\ 0 & 0 & 1 \\ -K_i & -K_d & -K_p \end{pmatrix} \begin{pmatrix} y_1 \\ y_2 \\ y_3 \end{pmatrix} \quad (3.102)$$

With $K_d = 20$, $K_p = 60$, $K_i = 100$ the system is stable as the state transition matrix A has all its eigen values, λ , with negative real part, as given below

$$\lambda = \{-16.7794 + 0.0000i, -1.6103 + 1.8348i, -1.6103 - 1.8348i\}$$

These controller parameters were arrived by trial and error using multiple simulation. The guiding principle behind the selection of these parameters was to choose one root far away form the imaginary axis so that its contribution to the response

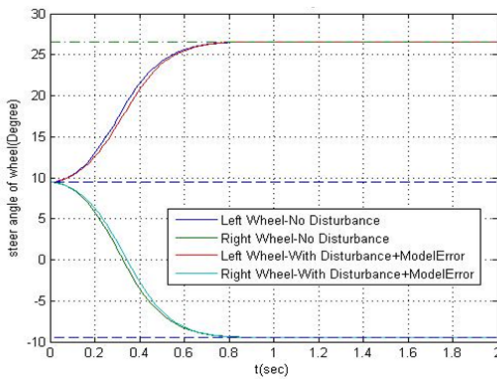


Figure 3.23: Change in steer angle

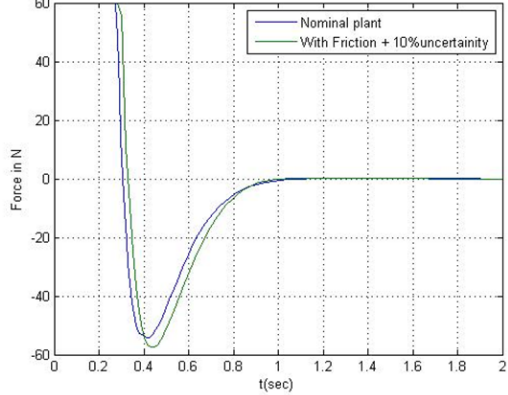


Figure 3.24: Control effort

decays faster with the respect to the other two roots. The system then behaves as second order system. The remaining two roots thus governs the dynamics of the system. They were chosen as complex conjugate with negative real part near the imaginary axis so as to make the steering unit dynamics under damped.

3.5.2 Simulation and results

The simulation of the dynamic Equation 3.98 and controller given by Equations 3.99 and 3.101 was carried out with the step change in steering angle responding to 20 mm rack displacemet (x). The parameter used for the nominal plant were obtained form solid model of the parts and are listed in table 3.2. The results of the wheel orientations and the actuator effort required are given in Figure 3.23 and 3.24 respectively.

Table 3.2: Key parameters steering assembly.

Wheel Mass	m_w	350 g
Wheel Inertia	I_{wxx}	463 Kg mm ²
Connecting Rod Mass	m_{10}	200 g
Link mass	m_l	80g
Link Inertia	I_{zz}	60834 Kg mm ²
Link Cg distance	r_o	18mm

The simulation results establishes that with 10% error in plant parameters there is practically no deviation in the performance of the controller. The results also predicts a settling time of 0.8 sec for the system. It may be noted that the

roll velocity of the wheel does not affect the dynamics of the steering system as is indicated by the absence of $\dot{\theta}_4$ and $\dot{\theta}_5$ from Equation 3.98 .

3.6 Summary

In this chapter, the dynamic equations were derived for the most general form of passive wheel configuration. Even though only two passive wheel configuration was considered the same formulation can be extended to any number of wheels. It is shown that the dynamics of standard caster wheels is a special case of the general case with $d_1 = 0$. It is also proven why a caster needs non-zero caster offset. There is a need of extra actuator in case $d_2 = 0$.

NOC based approach to model wheel slip in dynamics of a mobile manipulator was presented in this chapter. RARS being a redundantly actuated system has a inherent tendency to induce slip in the wheels if their velocities and orientations are not synchronised. A simulation study of RARS was carried out to assess the effect of wheel slip on its dynamics.

The steering mechanism was modelled separately. Simulation was used to find the controller parameters which makes the system marginally damped. This ensured that there is no over steering while keeping the settling time small. These controller parameters were later used to tune the actual system.

Chapter 4

Control of a Mobile Manipulator

In this chapter, the control architecture of the tele-operated mobile manipulator or platform is presented. The user interface for teleoperation is discussed. The control algorithm running on the mobile manipulator and the hardware used for the control of traction and steering is discussed. The protocol used for communication between the robot and the user interface is also described in detail.

4.1 Control Architecture and Hardware

The mobile manipulator explained in chapter 2 was planned to be teleoperated over a wireless network. The control block diagram and architecture are shown in Figure 4.1. It has a remote control station which is the interface for the operator

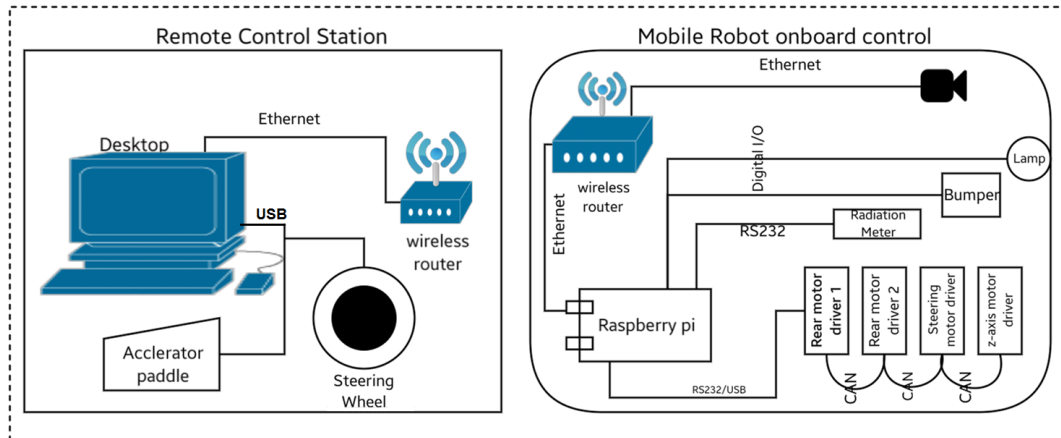


Figure 4.1: Control architecture

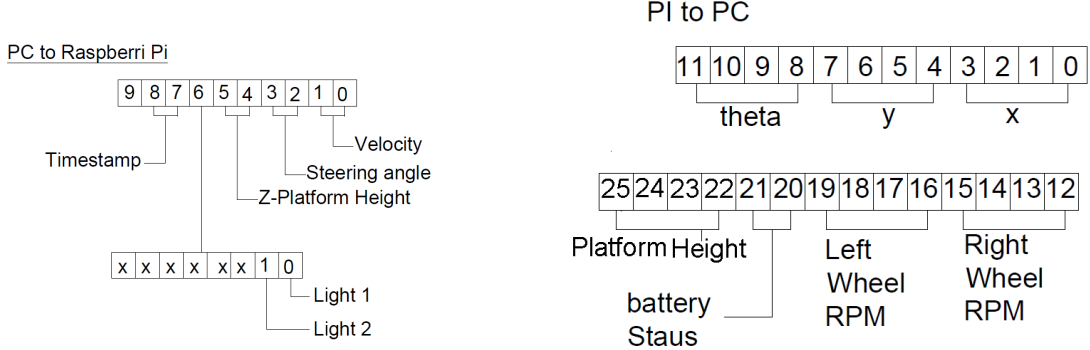


Figure 4.2: Data from PC to the robot Figure 4.3: Data from the robot to PC

and a local onboard controller of the mobile robot. They communicate over a dedicated wireless network. The remote station sends data packet in every 50 milliseconds (20Hz) to the mobile robot. The commanded velocity, steer angle, z position of the platform, and state of the detector and headlamps constitute the data packet sent by the remote station, as shown in Figure 4.2. The onboard controller of the mobile robot replies with a data packet consisting of the X, Y position and orientation θ of the robot, the current steer angle, angular velocities of each wheel, the z position of the top platform, battery voltage and current of each motor. They are indicated in Figure 4.3.

4.1.1 Local onboard controller

The onboard computer which is Raspberry Pi running Raspian (linux) OS receives command from the remote station and controls the robot hardware through customized C++ application. The Raspberry Pi is daisy chained to the four Maxon make, EPOS2 motor controllers/drivers. The communication between the onboard computer and the first Maxon controller is over usb/RS232 interface using Maxon's proprietorial protocol [138]. The first controller serves as CAN master for the rest of the controllers. The rear wheel motor drivers were configured in velocity servo loop. The drivers for steering and the z-axis motors were configured in position control loop. The camera mounted on the mobile robot and Raspberry Pi were connected over Ethernet via a wireless hub. The wiring diagram of the

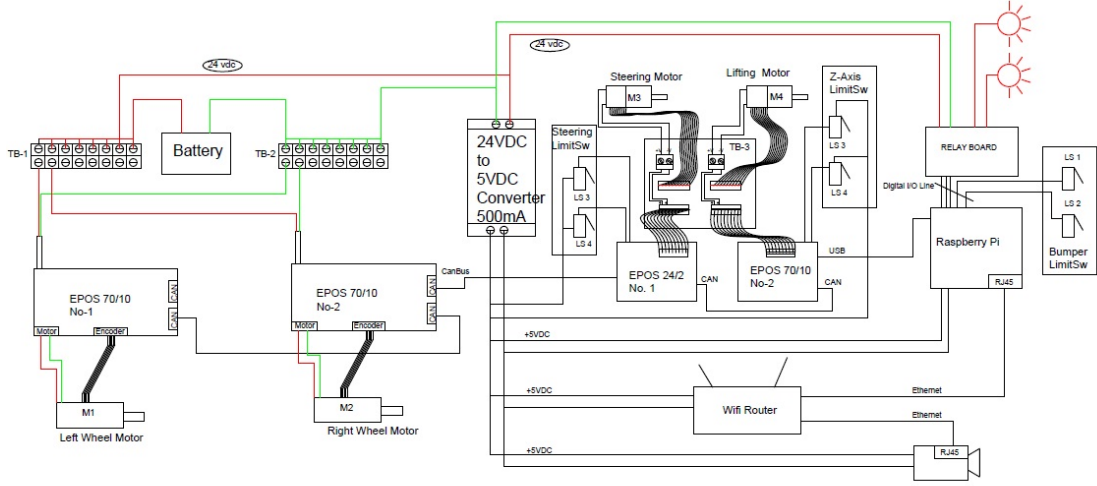


Figure 4.4: Wiring diagram of the WMR

robot is given in Figure 4.4. Since the onboard camera is connected to the wireless network directly, it does not interfere with the command loop between the Raspberry Pi and the PC.

The mobile robot is teleoperated using position-speed command as in [139]. The workspace for the mobile robot was assumed infinite compared to the input device. In case of manipulators position-position, control approach is generally used with scaling. In this case, the mixed approach was used. The steering angle was controlled in position-position mode whereas the mobile robot's speed was controlled by foot pedal's position, i.e. in position-velocity mode. This can be given by the following equation:

$$\begin{pmatrix} V \\ \theta_s \end{pmatrix} = \begin{pmatrix} K_v & 0 \\ 0 & K_s \end{pmatrix} \begin{pmatrix} \tilde{X}_p \\ \tilde{\Theta}_s \end{pmatrix} \quad (4.1)$$

where \tilde{X}_p is the displacement of pedal, $\tilde{\Theta}_s$ is the twist of steering wheel, K_v and K_s are the proportionality constants, V is the velocity of point O_3 and θ_s is the displacement of the steer motor. These proportionality constants are derived based on extreme limits. They are listed in Table 4.1.

Table 4.1: Proportionality constant table

Robot parameters	range	Joy-Stick Parameter	range	parameter Value
θ_s	-60 to +60	$\dot{\Theta}_s$	-90° to 90°	$K_s = 2/3$
V	0 to +60 mm/sec	\tilde{X}_p	0 to 30mm	$K_v = 2$

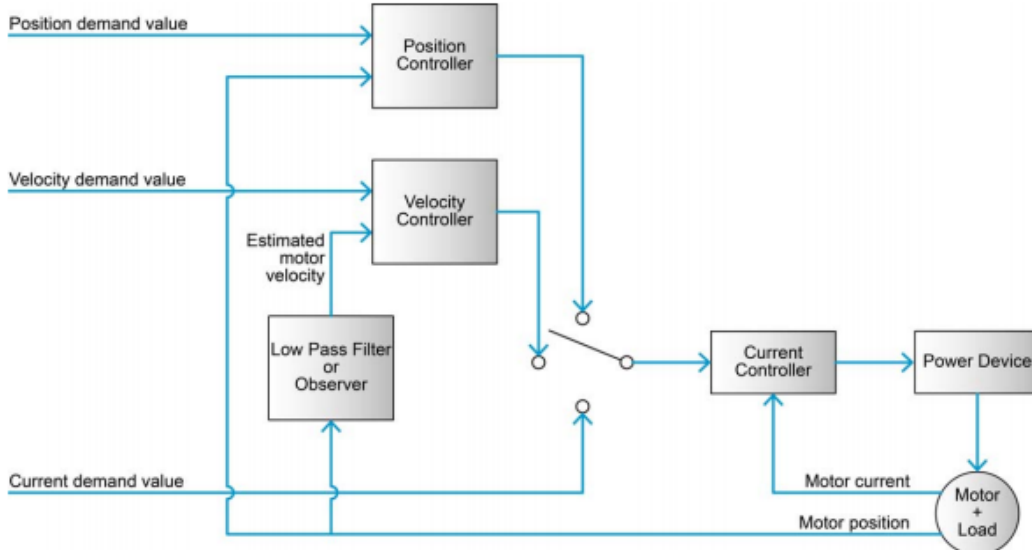


Figure 4.5: Block diagram of EPOS4 controller

4.1.2 Details of the motor controller

Three EPOS2 controllers from Maxon Motors were used to control the mobile robot's rear wheel velocity and the steering gears position. Each controller can control one motor. The overall architecture of the controller as given in [140], [141] is shown in Figure 4.5. The controller can be configured in either current, position or velocity control mode. The inner most current loop controls the torque of the motor. The current feedback loop shown in Figure 4.6 is a Proportional Integrator (PI) controller, running at 25KHz and the transfer function of the PI block is given as 4.2.

$$C(s) = K_p + \frac{K_I}{s} \quad (4.2)$$

where K_p and K_I are the proportional and integral gains.

The rear motor controllers are configured in the velocity control mode. The block diagram of the velocity loop is given in Figure 4.7. The velocity controller is a PI controller with velocity and acceleration feed-forward. The transfer function

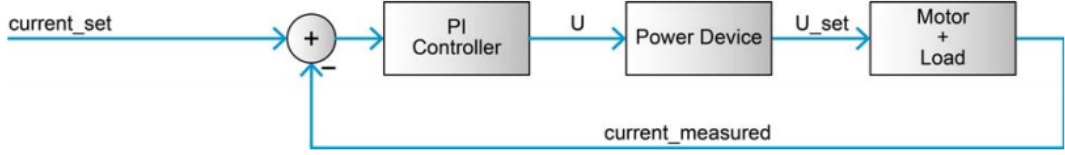


Figure 4.6: Current control block

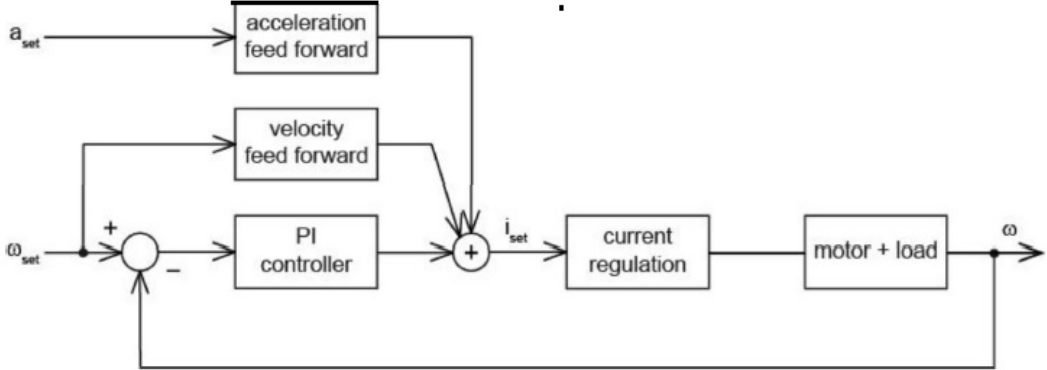


Figure 4.7: Velocity control bolck

$V(s)$ of the velocity loop PI block is given by

$$V(s) = K_{p\omega} + \frac{K_{I\omega}}{s} \quad (4.3)$$

where $K_{p\omega}$ and $K_{I\omega}$ are proportional and integral gains for velocity, respectively. The sampling rate of the velocity loop is 2.5 KHz. The feedforward acceleration and velocity was used to compensate for the known inertial load and viscous frictional load [141] respectively. Velocity is estimated from differentiation of the position data, the low-pass filter in Figure 4.5 eliminates noise due to differentiation. The transfer function $H(s)$ for the low-pass filter is given by

$$H(s) = \frac{1}{1 + \frac{K_{p\omega}}{48K_{I\omega}}} \quad (4.4)$$

The gain values used for each rear motor in the velocity control mode is listed in Table 4.2. No acceleration or velocity feedforward was used. The gain parameters were determined by auto tuning software provided by Maxon Motors.

The steering motor is in position control mode. The block diagram is shown in

Table 4.2: Parameters for left and right rear wheel motor controllers

<i>Gain Parameter</i>	<i>Right motor Value</i>	<i>Left motor Value</i>	<i>Unit</i>
K_p	300	230	$\frac{mV}{A}$
K_I	100	53	$\frac{mV}{A.mS}$
$K_{P\omega}$	1000	5182	$\frac{mA.sec}{rad}$
$K_{I\omega}$	100	425	$\frac{rad}{mA}$

Figure 4.8. It is a PID controller with transfer function given as

$$P(s) = K_{PP} + K_{IP}s + \frac{K_{DP}s}{1 + \frac{K_{DP}}{10K_{PP}}s} \quad (4.5)$$

where K_{PP} , K_{IP} and K_{DP} are position proportional, integral and derivative gains respectively. The velocity feed-forward $F_{\omega P}$ and acceleration feed-forward $F_{\alpha P}$ were used in position control loop to take care of viscous friction and known inertial load. The gains for controller were decided using auto tuning software provided by Maxon Motors. The values are reported in Table 4.3.

It may be noted that the controller parameters listed in Table 4.3 are very different from those used in simulation. This difference is due to the fact that the control structures are different. In the actual system motor dynamics influences, which was not considered during the simulation. In simulation, position error directly affects the torque of the motor through the control parameters K_p , K_d and K_I , whereas the position error in actual system sets the motor current. Hence their units too are different. Direct comparison between simulation PID parameters and actual controllers PID values cannot be done. However, the PID parameters tuned during simulation provided a starting point for the PID tuning for the actual system.

4.2 Control Algorithm

This section discusses in detail the algorithm running on the onboard controller. Command received by the controller was parsed to extract the velocity and the

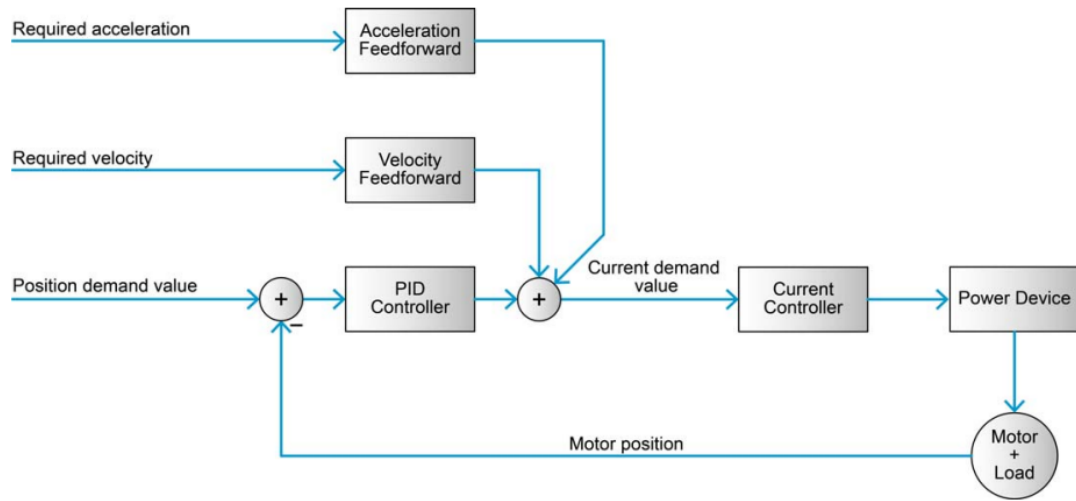


Figure 4.8: Position control bolck

Table 4.3: Parameters of steering motor controller

Gain Parameter	Value	Unit
K_p	537	$\frac{mV}{A}$
K_I	307	$\frac{mV}{A \cdot mS}$
K_{PP}	128	$\frac{mA \cdot sec}{rad}$
K_{IP}	663	$\frac{mA}{rad}$
K_{ID}	200	$\frac{mA}{rad}$
$F_{\omega P}$	0	$\frac{rad}{mA \cdot sec}$
$F_{\alpha P}$	54	$\frac{mA \cdot sec^2}{rad}$

steer angle information. They were suitably scaled to get command velocity V in mm/sec, and steering angle θ_s in radians. It may be noted that the velocity V corresponds to the velocity of point O_r the reference point of the mobile robot. Next the set point for each motor was calculated and sent to individual drive. The algorithm is listed below and the block diagram for the same in Figure 4.9

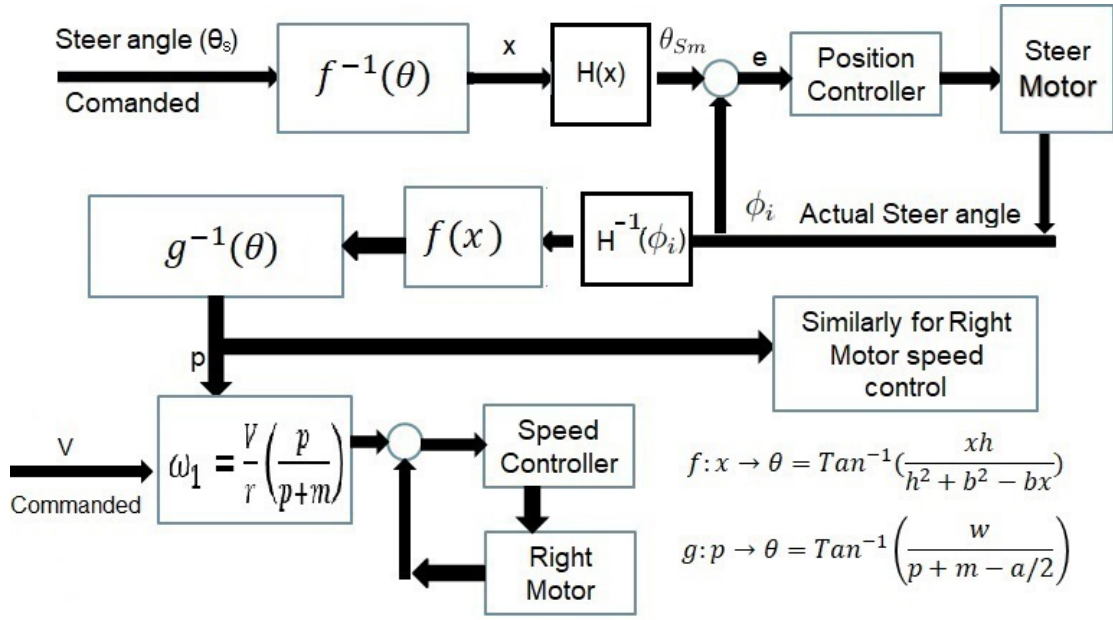


Figure 4.9: Block diagram of WMR controller

1. Calculate the setpoint for steering motor θ_{Sm} based on θ_s .
2. Read the current steering angle ϕ_i .
3. Calculate the velocity setpoints ω_i and ω_o of rear wheels based on the V and ϕ_i .
4. Command setpoints ω_i , ω_o and θ_{Sm} to each motor.

The above loop is repeated every 50 mSec.

The steer angle command received from the control station is not directly sent to the steer motor as set point after suitable scaling. The steer set point is based on the current rear wheel velocities. This is important as the response time of the motors are different. The above methodology helps minimize the deviation from

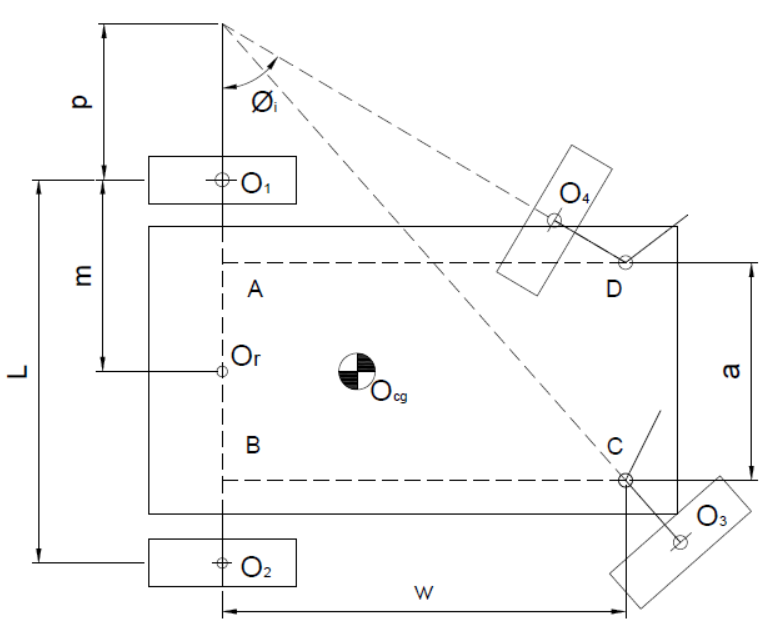


Figure 4.10: Ackerman steering condition

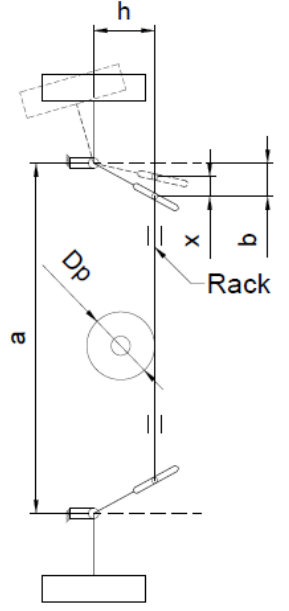


Figure 4.11: Davis steering gear

the Ackerman steering condition even during transit condition, particularly, in case of large change in commanded v and θ_s . Each block in Figure 4.9 is discussed next.

It may be noted that the θ_s always refers to the steer angle of the inner front wheel ϕ_i and V refers to O_r as shown in Figure 4.10, i.e.

$$\theta_s = \phi_i \quad (4.6)$$

The set point of the steering motor at the output of gear box θ_{Sm} is given by equations 4.7 and 4.8 based on the geometry of Davis steering gear [108].

$$\tan \phi_i = \frac{xh}{h^2 + b^2 - bx}$$

or

$$f(\phi_i) : x = \frac{\tan \phi_i(h^2 + b^2)}{h + b \tan \phi_i} \quad (4.7)$$

where x is the displacement of the rack and h and b are link lengths. The rack is

connected to the steering motor by pinion of PCD D_p (30mm) as shown in Figure 4.11. Therefore, the steering motor angle, θ_{Sm} , is given below as

$$H(x) : \theta_{Sm} = x \frac{360}{\pi D_p} \quad (4.8)$$

Next, the equation relating current steer angle ϕ_i and rear wheel set point velocities ω_{RS} and ω_{LS} is presented. From the geometry of Figure 4.10, one gets

$$\begin{aligned} \tan \phi_i &= \frac{\bar{BD}}{\bar{OB}} = \frac{w}{p + m - a/2} \\ g : \phi_i \rightarrow p, \quad p &= \frac{w}{\tan \phi_i} - m + \frac{a}{2} \end{aligned} \quad (4.9)$$

Now using Equations 3.13 and 3.14 in equations relating the right and left wheel velocities to the WMR platform angular velocity ω_3 and velocity, V , of the reference point O_r , presented below

$$\dot{O}_r = \dot{O}_i + \omega_3 \times (O_r - O_i)$$

$$\dot{O}_r = \dot{O}_o + \omega_3 \times (O_r - O_o)$$

We get the velocity of each rear wheel as

$$\begin{aligned} \omega_i &= \frac{Vp}{r(p+m)} \\ \omega_o &= \frac{V(p+2m)}{r(p+m)} \end{aligned}$$

Using the above equations and Equation 4.9, the setpoints for the rear wheels are as follows

$$\omega_i = \frac{V}{r} \frac{\left(\frac{w}{\tan \theta_o} - m + \frac{a}{2}\right)}{\frac{w}{\tan \theta_o} - m + \frac{a}{2} + m} \quad (4.10)$$

$$\omega_o = \frac{V}{r} \frac{\left(\frac{w}{\tan \theta_o} - m + \frac{a}{2}\right) + 2m}{\frac{w}{\tan \theta_o} - m + \frac{a}{2} + m} \quad (4.11)$$

4.2.1 Safety interlocks

The control algorithm has safety interlocks built into it. The vehicle speed has been limited to 0.5 m/sec, this was done based on operator feedback for convenience in driving the vehicle remotely. The vehicle does not move if the manipulator is in the extended condition. This is to avoid overturning of the vehicle in case it has to climb a ramp. Acceleration of the vehicle is never exceeded beyond the limiting value of $0.144g$ which was arrived at based on dynamic stability of the mobile robot as calculated in Equation 2.4. To avoid overturning of vehicle while following a circular path, the linear velocity of the vehicle is limited by Equation 2.7 which is a function of the turning radius.

4.2.2 Wheel odometry

The dead reckoning odometry can be performed based on either the differential drive or Bicycle model. In the present case, we use the differential drive model. Where the rear wheel velocities were used to determine the position and orientation of the mobile robot. The position here means the position of the reference point O_r . The steps are follows.

1. calculate V and ω_3 from current wheel velocities ω_1 and ω_2 using equations 3.14 and 3.15 with $a = 0$.
2. integrate V and ω_3 over time step.

If $x(t)$, $y(t)$ are the coordinate of O_r and $\beta(t)$ be the orientation of the robot with some global coordinate system, the kinematic model of the differential wheel robots is given by [20]

$$\begin{pmatrix} \dot{x} \\ \dot{y} \\ \dot{\beta} \end{pmatrix} = \begin{pmatrix} \cos \beta & 0 \\ \sin \beta & 0 \\ 0 & 1 \end{pmatrix} \begin{pmatrix} V \\ \omega_3 \end{pmatrix} \quad (4.12)$$

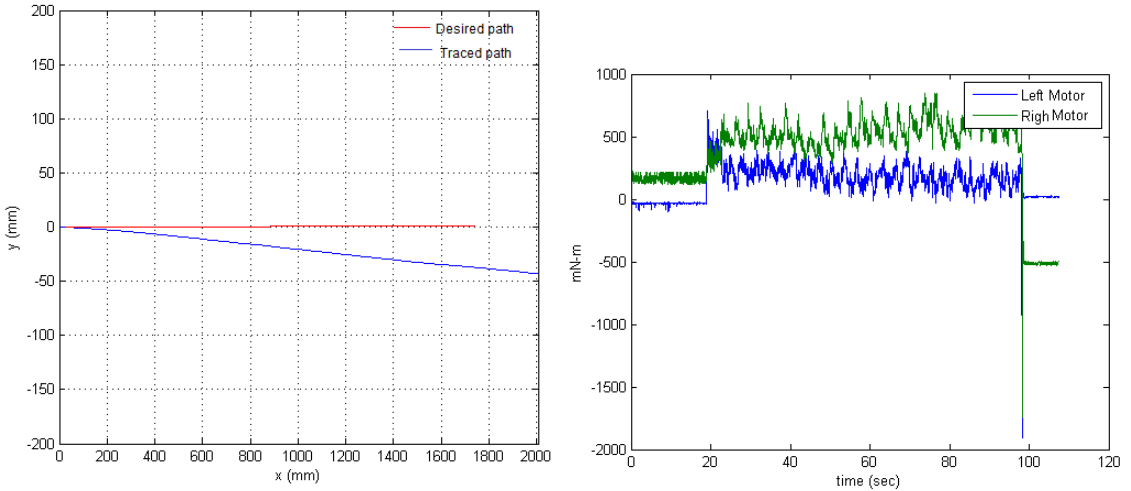


Figure 4.12: Tracing a line

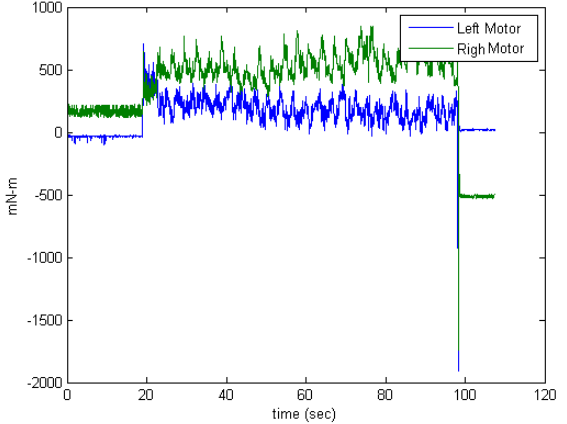


Figure 4.13: Motor torque

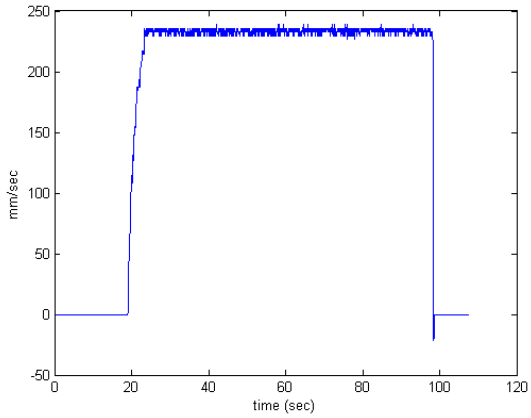


Figure 4.14: Linear velocity

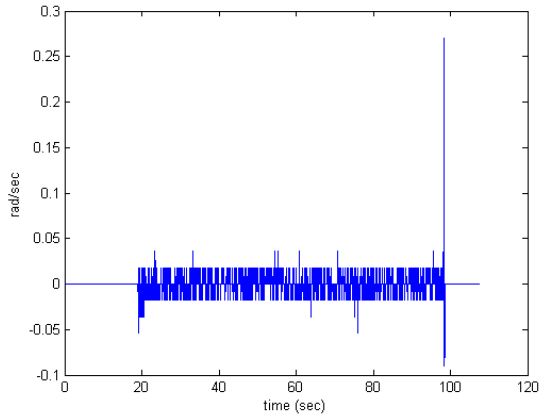


Figure 4.15: Angular velocity

Equation 4.12 is numerically integrated for time δt using the following expressions:

$$x(i + 1) = x(i) + \delta t V(i) \cos \beta(i); \quad (4.13)$$

$$y(i + 1) = y(i) + \delta t V(i) \sin \beta(i); \quad (4.14)$$

$$\beta(i + 1) = \beta(i) + \delta t \omega_3(i); \quad (4.15)$$

where i is at time step t_i . Next, the actual odometric results for the vehicle moving in a circle and a straight line are presented.

As seen in the graph of Figure 4.12 there is a lateral shift in the robots path calculated using odometry. There is a linear shift too, which can be observed due to longer path calculated by odometry. The lateral shift of 200 mm and a linear shift

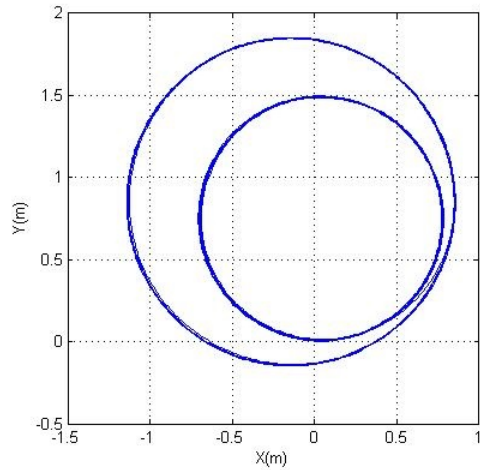


Figure 4.16: Tracing a circle

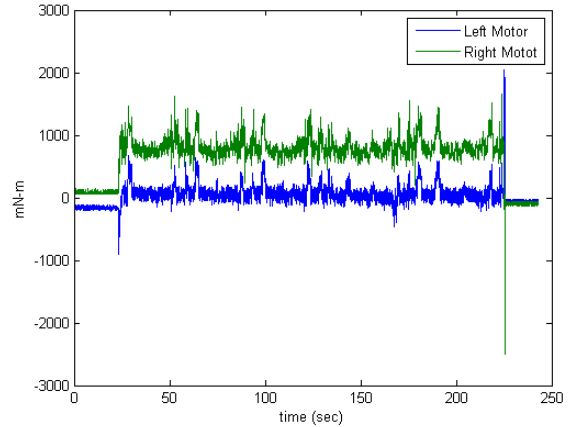


Figure 4.17: Motor torque

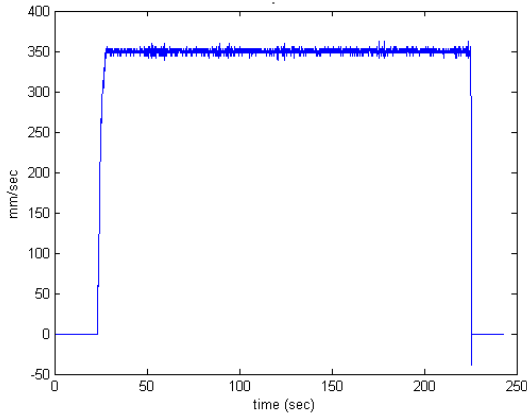


Figure 4.18: Linear velocity

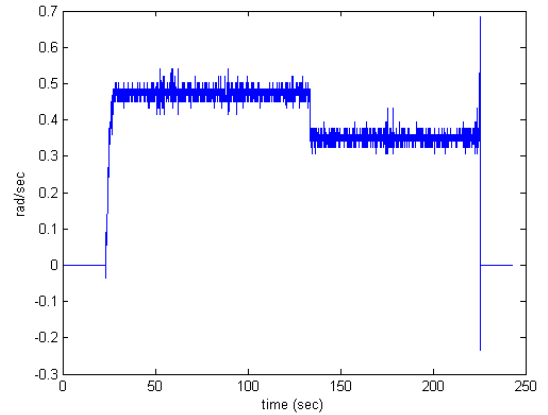


Figure 4.19: Angular velocity

of 300 mm for 15000 mm long path was calculated. This clearly indicates slip in the wheels. The torque curves also shows that one wheel is more loaded than the other this is expected as the battery weight was on one side of the robot.

In Figure 4.18 the robot traces circular path of two different radius. It can be seen that there is no lateral (side) slip during the motion. The step change in the angular velocity at time $t \approx 125 \text{ sec}$, shown in Figure 4.19, indicate transition to a larger radius path. The linear velocity of the robot is maintained constant at 300 mm/sec .

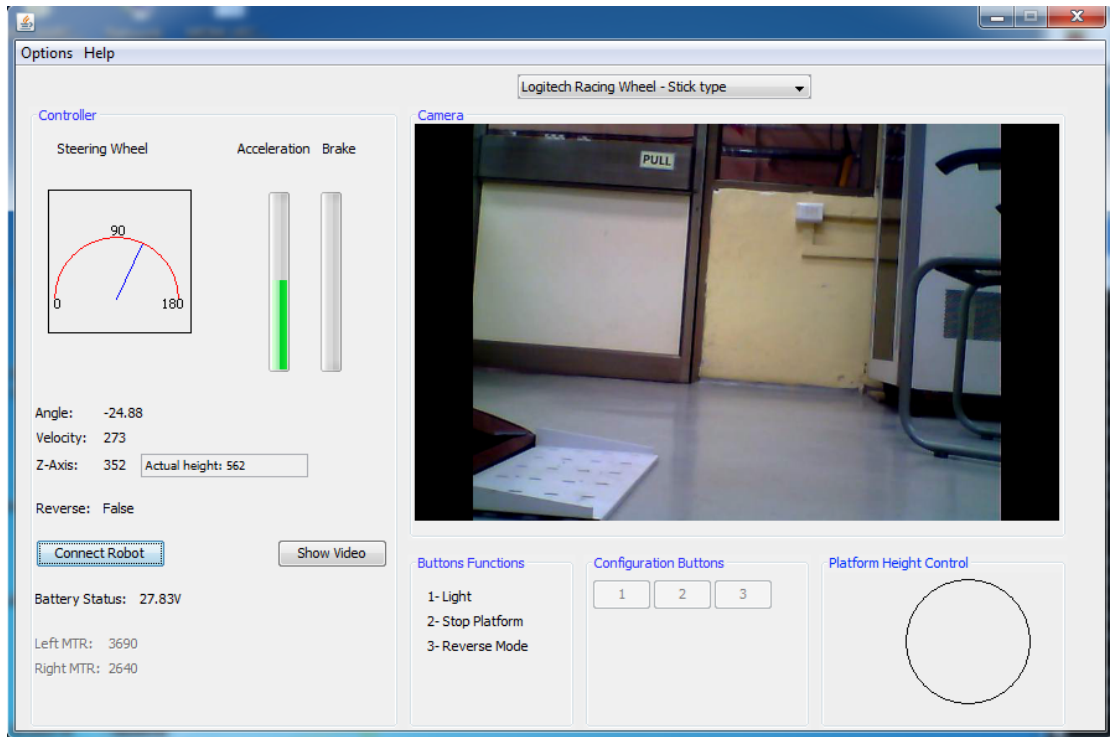


Figure 4.20: User interface for teleoperation

4.3 Remote control station

The operator controls the vehicle from a local station away from the robot over a wireless network. The control station consists of a desktop computer running Windows XP. A steering wheel and two foot switches are connected to the desktop. The steering wheel sets the steering of the remote mobile robot and the footpadel is used to set the velocity V of the robot. A push button in the steering wheel is used to reverse the direction of motion of the robot.

The screen of the desktop displays video streaming from the mobile robot's on board camera. A graphical user interface (GUI) shown in Figure 4.20 displays the robot's parameters such as current steer angle, velocity of each rear wheels and the position of the z-axis. Buttons on the GUI operates the z-axis, head lamps, etc.

4.4 Summary

In this chapter, the control architecture of the mobile manipulator has been presented. The algorithm used to move the robot was discussed in detail. The odometry used for pose estimation of the robot was also presented with the experimental results.

Chapter 5

Simulation of Tele-operation

In this chapter, simulation of a tele-operated mobile robot is presented. In tele-operation, the human operator observes a remote scene through camera(s), and manipulates the local steering wheel and accelerator pedal, as illustrated in Figure 5.1 . The command is transmitted to the mobile robot over wireless network. The operator's response is based on the latest feedback images from the cameras. In general, there is a time lag when communication takes place over wireless network. The time lag deteriorates the human performance as discussed in [95] and references therein. This chapter simulates the tele-operation both without and with time delay in transmission network.

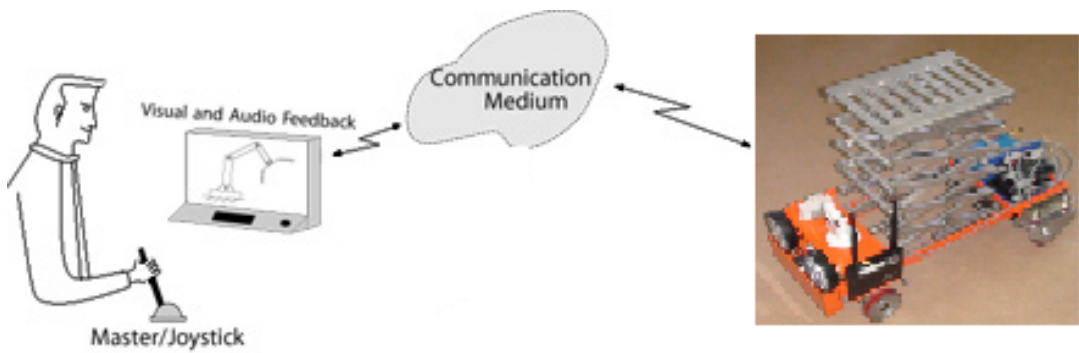


Figure 5.1: Teleoperation architecture

5.1 Modeling of Mobile Robot

The standard kinematic model, as described in [20], of the mobile robot was used for the simulation. The use of kinematic model is justified as the vehicle is expected to move at relatively slow speed and model is simple. Inputs to the model are left and right rear wheel velocities. The front wheels are steered to satisfy the Ackerman condition, as presented in Chapter 2 and are assumed to attain the desired angle instantaneously. Therefore, the robot can be treated as differential drive robot. The kinematic model of the platform is presented below:

$$\begin{pmatrix} \dot{x} \\ \dot{y} \\ \dot{\theta} \end{pmatrix} = \begin{pmatrix} \cos \theta & 0 \\ \sin \theta & 0 \\ 0 & 1 \end{pmatrix} \begin{pmatrix} r_w/2 & r_w/2 \\ r_w/l & -r_w/l \end{pmatrix} \begin{pmatrix} \dot{\phi}_L \\ \dot{\phi}_R \end{pmatrix} \quad (5.1)$$

where , l is the distance between the rear wheels, r_w wheel radius. $\dot{\phi}_R$ and $\dot{\phi}_L$ are the rotational velocities of left and right wheels. The operator station sends the command u_1 and u_2 over the wireless network. In general, it will be delayed by time δ . These commands are interpreted by the robot controller as the left and right wheel velocities. Therefore, by taking the time delay into consideration one can write

$$\begin{pmatrix} \dot{\phi}_R(t) \\ \dot{\phi}_L(t) \end{pmatrix} = \begin{pmatrix} u_r(t - \delta) \\ u_l(t - \delta) \end{pmatrix} \quad (5.2)$$

The control inputs to the mobile robot u_r and u_l are generated by the operator based on the visual data available to the person. Hence, a model of the human operator needs to be used for the simulation of the complete loop.

5.2 Model of Human Operator

In order to simulate the tele-operation loop, one needs a mathematical model of a human operator. The mathematical model of the operator's action is approached assuming a car driving metaphor. The video feedback, which the operator receives

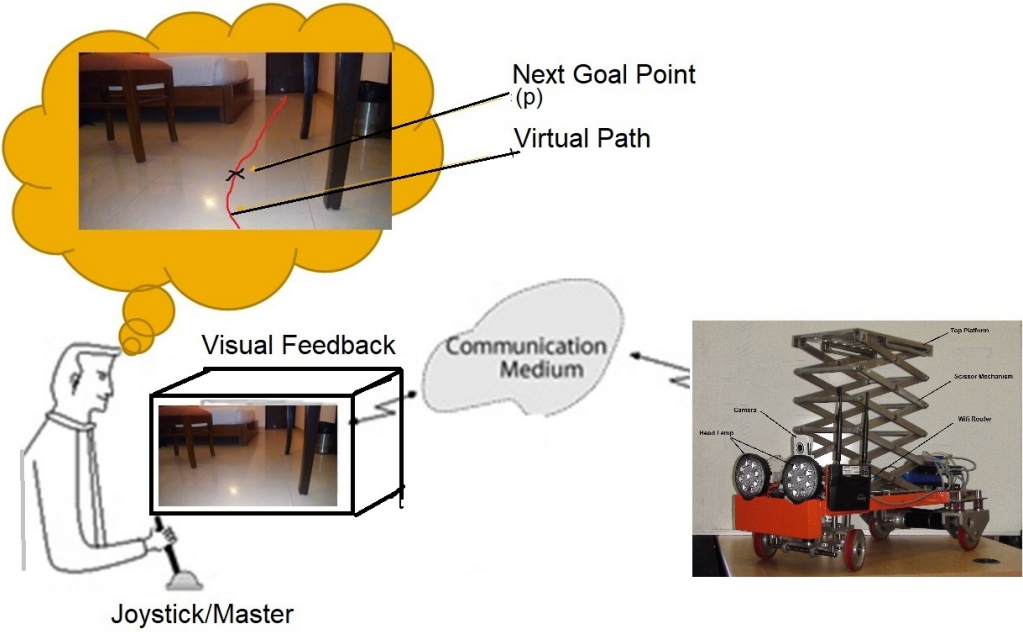


Figure 5.2: Assumed driving strategy

of the remote environment, give him the idea of the vehicle's position and the tentative next goal point (p) based on a lookahead distance (l). He then constructs a virtual path mentally and tries to manoeuvre or steers the robot to follow that path as shown in Figure 5.2. As he moves forward the goal point keeps changing until he reaches the desired location. This methodology of path tracing is known as pure pursuit [54].

The mathematical model for the pure pursuit method of path following can be derived as given in Figure 5.3. As shown in Figure 5.3, the origin of the coordinate system is at point o , the middle of rear axis of the robot. As the differential drive robot can move only about a circle with center lying on the line along its rear axis. An arc OP of radius r , is drawn with center O_1 and passing through o and p . Where p is a point on the path to be traced by the robot. The linear distance between the points o and p is called the *look ahead distance* l . This distance in the case of a tele-operated robot will depend on the field of view of camera at the remote location and the obstacles present in the remote environment.

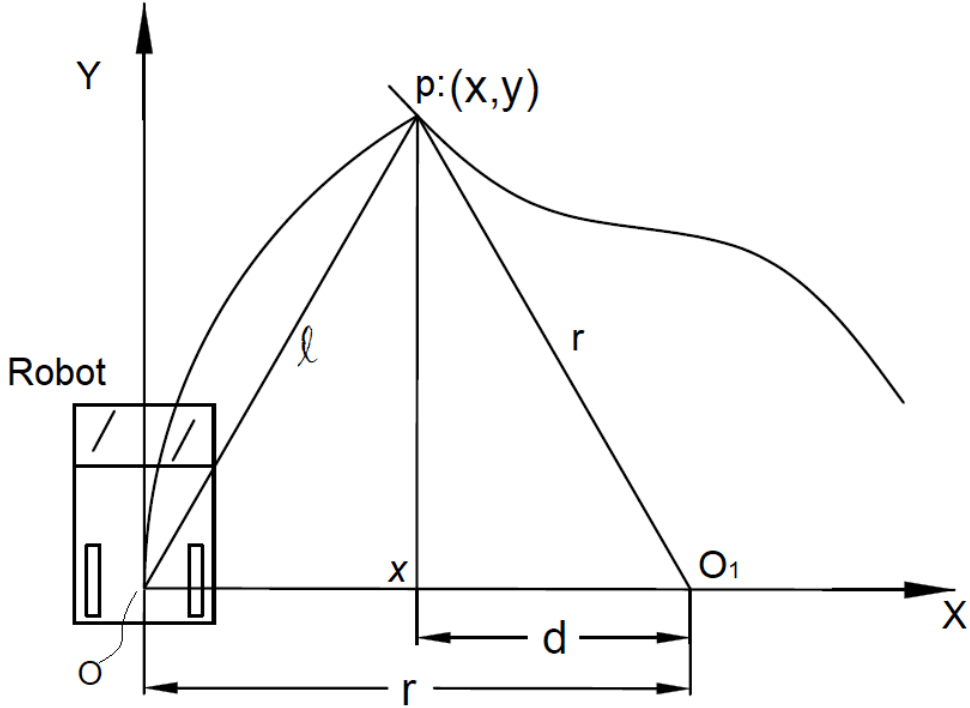


Figure 5.3: Geometry of Pure pursuit

If (x, y) is the coordinate of point p in $X - Y$ coordinate system, then

$$x^2 + y^2 = l^2, \quad d = r - x \quad (5.3)$$

Similarly, from triangle p, x, o_1 we get

$$d^2 + y^2 = r^2 \Rightarrow (r - x)^2 + y^2 = r^2 \Rightarrow x^2 + y^2 - 2rx = 0 \quad (5.4)$$

Replacing x^2 and y^2 in Equation 6.4 with Equation 6.3, we get

$$2rx = l^2 \Rightarrow r = \frac{l^2}{2x} \quad (5.5)$$

Once the radius r , the desired linear velocity of the robot v are known, the angular velocity of the vehicle is $\dot{\theta} = -v/r$. The rear wheel $\dot{\phi}_L(t)$ and $\dot{\phi}_R(t)$ can be calculated from Equation 6.1. Where $\dot{y} = v$ and $\dot{x} = 0$. To match the orientation of the vehicle with that in Figure 5.3, $\theta = 90^\circ$. We then get

$$\begin{pmatrix} \dot{x} \\ \dot{y} \\ \dot{\theta} \end{pmatrix} = \begin{pmatrix} 0 & 0 \\ r_w/2 & r_w/2 \\ r_w/l & -r_w/l \end{pmatrix} \begin{pmatrix} \dot{\phi}_L \\ \dot{\phi}_R \end{pmatrix} \Rightarrow \begin{pmatrix} \dot{\phi}_L \\ \dot{\phi}_R \end{pmatrix} = \begin{pmatrix} \frac{1}{r_w} & \frac{l}{2r_w} \\ \frac{1}{r_w} & -\frac{l}{2r_w} \end{pmatrix} \begin{pmatrix} v \\ \dot{\theta} \end{pmatrix} \quad (5.6)$$

The operator station sends v and $\dot{\theta}$ as the command over the communication network to the robot. The Figure 5.4 shows the simulation strategy

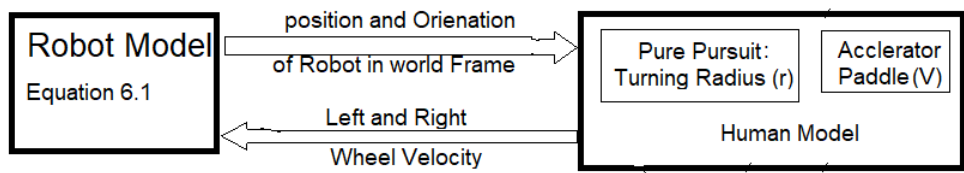


Figure 5.4: Simulation scheme

5.3 Simulation and Results

The teleoperation loop consists of the operator model described in Section 6.2 at one end of the communication link and the mobile robot model described in Section 6.1 on the other end . As shown in Figure 5.5, there will a delay in both directions of communication. In real system, the video image is streamed by the robot. Due to large quantity of data and limited bandwidth the delay $T_1 \gg T_2$. The amount of delay h_1 was experimentally measured and it was found around 0.5 sec, as described in Appendix A. The command sent by the operator is v and $\dot{\theta}$ which is few bytes only. Therefore in simulation $h_2 = 0$ is assumed.

5.3.1 Simulation algorithm

The algorithm for simulation is explained in the following steps.

1. Convert the path from global coordinate system (CS) to Robots Local Coordinate System

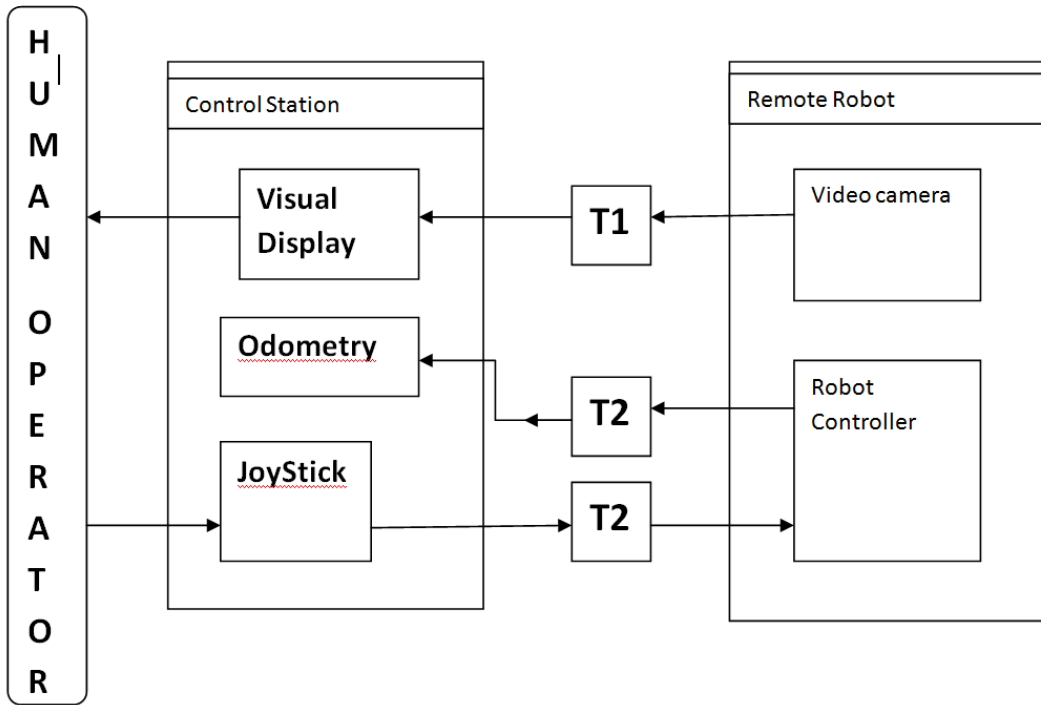


Figure 5.5: Block diagram for teleoperation

2. With a given look ahead distance (l) search for a point on the path
 - If point is found goto Step 3
 - If not found increase the look ahead distance
3. Determine the turning radius (r) using Equation 6.5
4. Calculate the command to the robot based on Equation 6.6. Note that these commands are based on the old visual data the operator saw.
5. Solve delayed differential equation.

Simulation was carried using Matlab. Delay differential equation solver "*dde24*" was used to solve Equations 6.1 and 6.2 with delayed inputs u_r and u_l . The desired path was a circle of radius 5m centred at origin of the global coordinate system. The human action was modelled with look ahead distance of 0.5m and linear velocity of 0.5m/s. The initial position of the robot was (4.5,0.0).

The performance of the system with zero delay, i.e. $T_1 = T_2 = 0$ is shown in Figure 5.6. Figures 5.7 and 5.8 show the robot's motion under delay of 0.5 and

0.8 sec. It is seen that oscillation becomes visible at 0.5sec delay, and with the delay of 0.8 sec the system was on the verge of instability.

It was also observed that the with large vehicle velocity, v and large look ahead distance, l the instability commences with smaller time delay, δ in Equation 6.2.

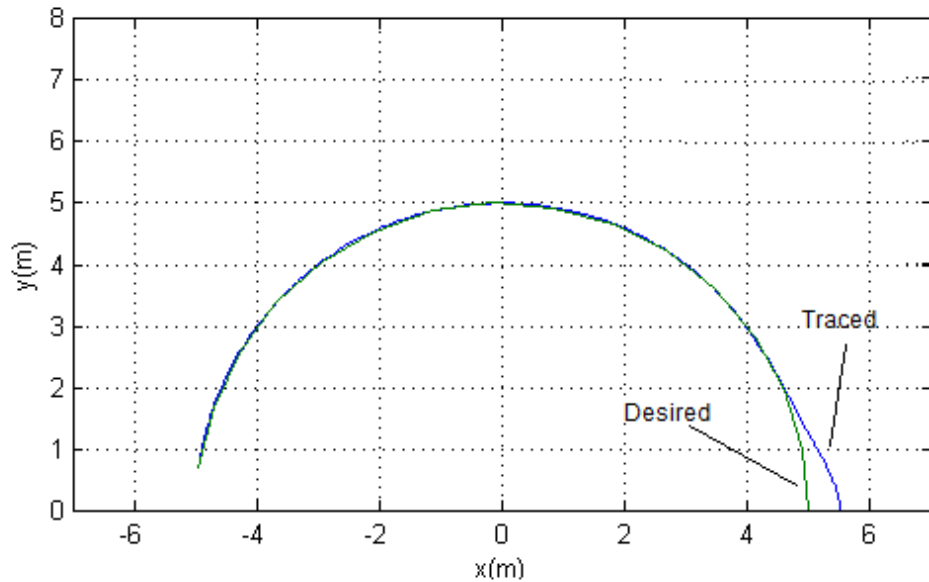


Figure 5.6: Simulation with no time delay in either direction

In the next section we propose a predictive model based feedback control which is used to stabilize robot motion under time delay teleoperation.

5.4 Summary

In this chapter, simulation study of the developed teleoperated mobile robot is presented. A mathematical model of the action of human operator while driving the robot based on visual feedback was presented. Simulation results show that the behaviour of the system deteriorates with increase in delay in communication between the local and remote station. With large time delay the system becomes unstable.

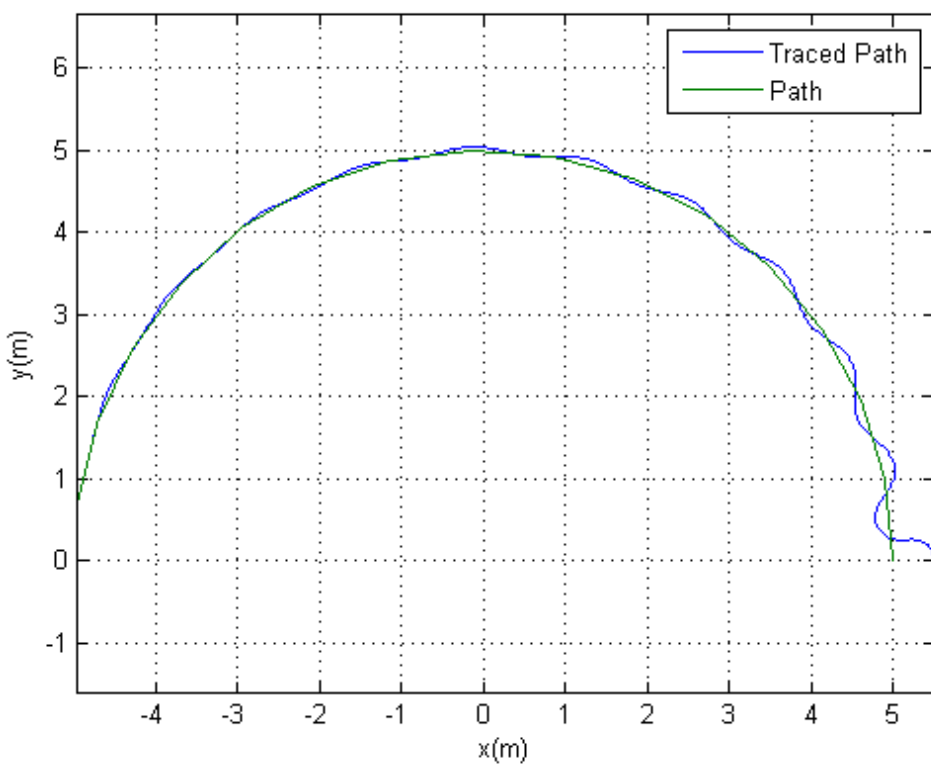


Figure 5.7: Simulation with time delay $h_1 = .5$ sec and $h_2 = 0$ sec

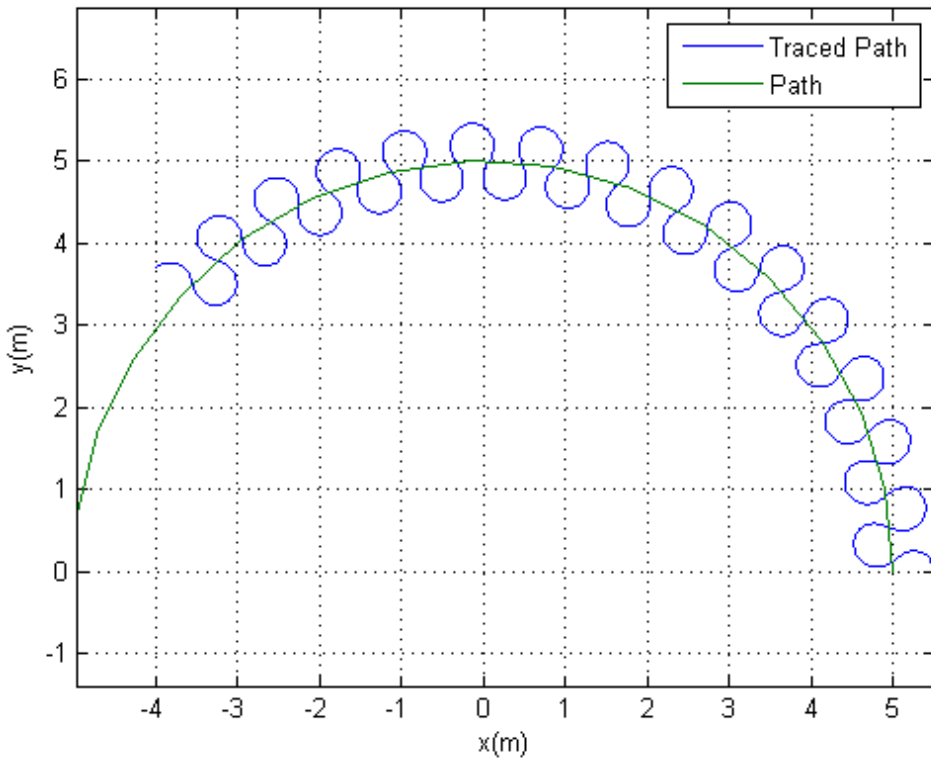


Figure 5.8: Simulation with time delay $h_1 = .8$ sec and $h_2 = 0$ sec

Chapter 6

Predictive Display for Time Delay Compensation

In the last chapter, it was shown using simulation that the time delay between the remote and local stations leads the system towards instability. In this chapter, first a predictive model controller for time delayed teleoperation is presented. Associated issues of time delay on human performance are then highlighted. To alleviate the problem of time delay in visual feedback, predictive display using a RGB-Depth sensor is implemented. Note that the basic framework for implementation may have been known but it was adapted for a specific vehicle like RARS for the first time.

6.1 Time Delay Compensation

Simulation of a time delayed system with pure pursuit model for human controller was presented in Chapter 5. Stability aspects with input delay to the human model was pointed out. In paper by Ollero [45], stability of pure pursuit with input delay is presented and for completeness it is briefly discussed in Appendix B. In view of the above theoretical analysis and the simulation results presented in Chapter 5, it is required to design a stabilizing controller to take care of large delays, e.g., 0.8 sec. One such design based on model predictive control is presented next.

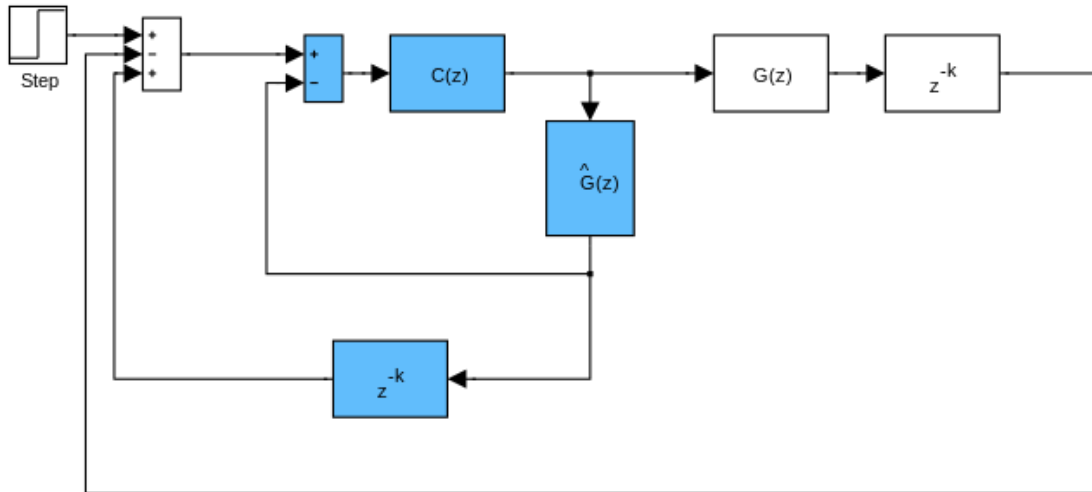


Figure 6.1: Smith predictor [142]

One of the earliest predictor based controller for linear system with time delay was proposed by Smith [142] called the Smith Predictor or Smith Controller. The schematic diagram of the smith controller is shown in Figure 6.1. There are two loops, the inner and the outer loop, where $G(z)$ is the plant, $C(z)$ is the stabilizing controller for the plant without delay, $\hat{G}(z)$ is the model of the plant. As can be seen from Figure 6.1, during the period (k time unit) when the feedback (output) is not available the model of the plant is used to predict the actual plant behaviour and generate the control signal accordingly.

In the presented case, the plant is the mobile robot developed in this PhD research. The block diagram shown in Figure 6.2 depicts the architecture of time delayed system which is applicable to the current mobile robot and the local station. The tele-operation over wireless network for our system resulted in a delay of $T_1 = 500 \text{ ms}$ with update frequency of 2Hz. The delay was caused due to large amount of data being transmitted as video feedback from the robot's onboard camera. Figure 6.3 shows the measured delay in the video link. The frequency of odometric and control data exchange between the two stations was at the rate of 20Hz, i.e., a delay $T_2 = 50 \text{ ms}$ only. This loop runs independent of the video feedback link. It may be noted that $T_2 \ll T_1$.

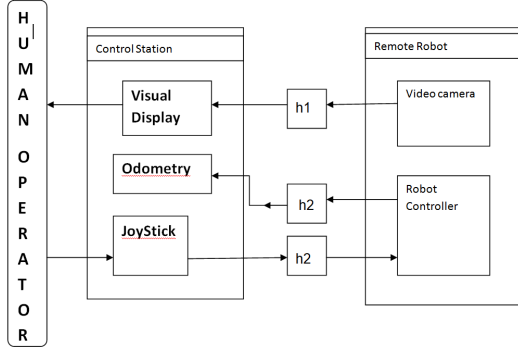


Figure 6.2: Block diagram of time delayed system

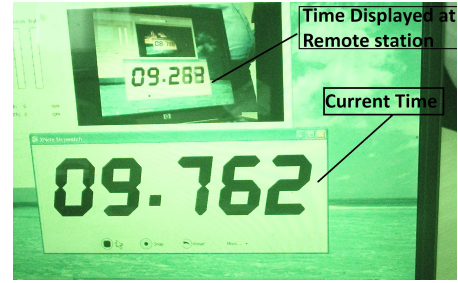


Figure 6.3: Delay measurement

6.1.1 Proposed controller

The proposed control strategy to mitigate the effect of time delay is to predict the current position from the last known position, based on the delayed video image; using the dynamic model of the mobile robot. As shown in Figure 6.4, let us assume that we are at time $t + \delta$, but the latest pose data of the robot available is that of at time t . The present pose at time $t + \delta$ was predicted using the dynamic model of the robot derived in Chapter 3, Equation 3.9, and presented here again for convenience.

$$I(\theta)\ddot{\theta} = C(\theta, \dot{\theta})\dot{\theta} + \tau \quad (6.1)$$

It may be noted that the dynamic model uses torque τ as its input, whereas the local station which uses pure pursuit for simulation of human action generates linear and angular velocities of the robot, v and ω as shown in Figure 6.5. This is taken care by first converting $v \equiv \dot{o}_3$ and $\omega \equiv \omega_3$ to rear wheel velocities using Equations 3.14 and 3.15. The rear wheel velocities are then used in PI controller of the rear wheel motors to generate the τ for Equation 6.1.

This predicted position is given to the pure pursuit algorithm to generate required control outputs for the remote robot. In the simulation, it was assumed that this control inputs reaches the remote robot instantaneously, as $T_1 \gg T_2$. As discussed in the Kinematic model of Chapter 5. Equation 5.1 was used to simulate the remote robot.

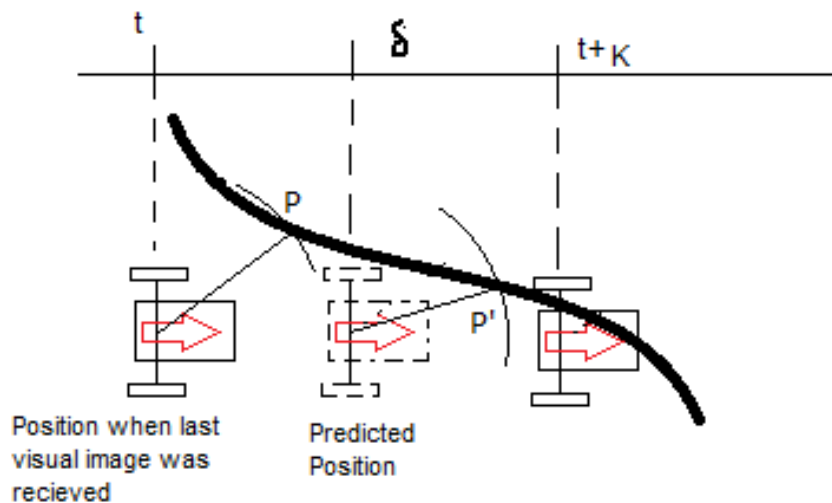


Figure 6.4: Smith predictor applied to RARS mobile robot

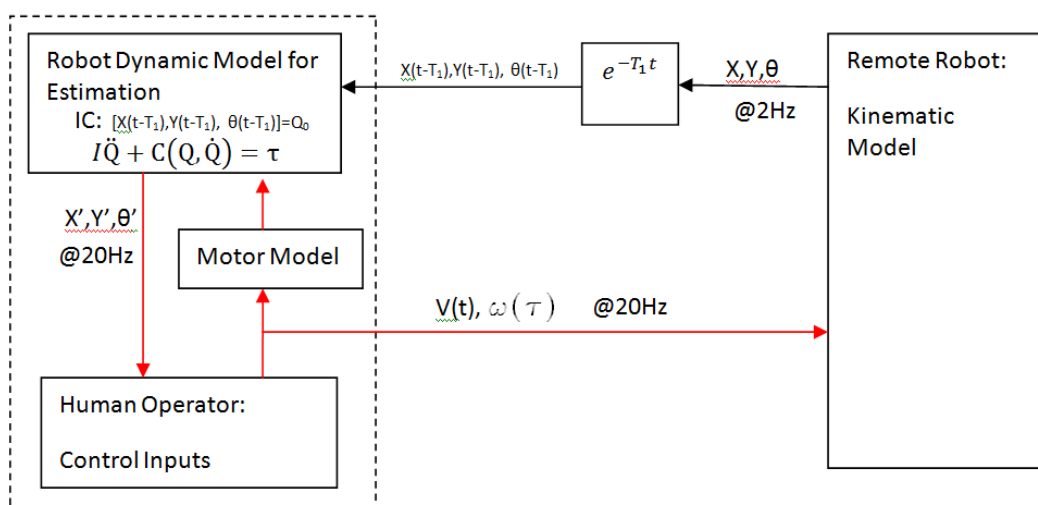


Figure 6.5: Simulation block diagram

6.1.2 Simulation algorithm and results

The simulation scheme is shown in block diagram of Figure 6.5. The algorithm is explained below.

- 1: Convert the path from global coordinate system (CS) to Robot's Local Coordinate System based on the current pose (x, y, θ) of the robot.
- 2: With a given look ahead distance (l) search for a goal point on the path.
- 3: Determine the turning radius (r) using Equation 6.5
- 4: Calculate ω using turning radius (r) and given Linear Velocity v
- 5: Command Robot ω and v
- 6: **if** new pose of the robot is available from remote station **then**
- 7: Update robot pose (x, y, θ)
- 8: **else**
- 9: Calculate the predicted pose of the robot based on command given in Step 4, and using dynamic model of the robot given by Equation 6.1.
- 10: Update robot's pose (x, y, θ)
- 11: **end if**
- 12: **Goto** Step 1

Simulation was carried using Matlab. Differential equation solver "*Ode24*" was used to solve Equations 5.1 and 6.1. The desired path was a circle of radius 5m centred at origin of the global coordinate system. The human action was modelled with look ahead distance l of 0.5m and linear velocity v of 0.5 m/s. The initial position of the robot was (4.5,0.0). The robot's motion under feedback delay of 0.5 sec and 0.8 sec, i.e., $T_1 = 0.5\ sec$ and $T_1 = 0.8\ sec$, are shown in Figures 6.6 and 6.7 respectively. It is seen that oscillation are no more visible at delay of 0.5 sec and 0.8 sec. The system shows no instability.

The above results show that model-based prediction of the robot's pose helps in removing the instability of the system. In actual teleoperation, the operator's control actions are based on the visual display available to him. The delay in visual feedback results in inefficient operator's performance as the person tends

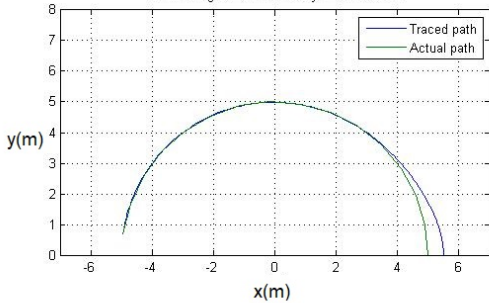


Figure 6.6: Time delay $T_1 = .5$ sec
and $T_2 = 0$ sec

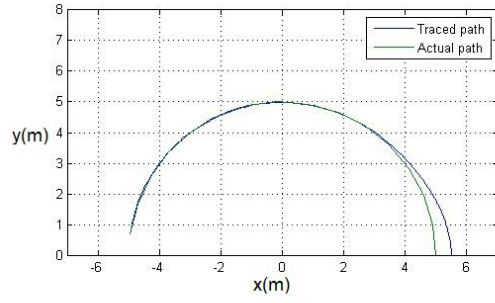


Figure 6.7: Time delay $T_1 = .8$ sec
and $T_2 = 0$ sec

to adopt a wait and watch policy to see the effect of his control action. In the next section, an implementation and adaptation of above discussed *model based prediction* for visual display feedback is presented.

6.2 Delay Compensation using Predictive Display

As indicated in Literature survey, the delay of visual feedback leads to inefficient and unstable performance of a teleoperated system. There are two major methods to overcome time delay induced problems in teleoperation. One is to use *supervisory control* and the other is *predictive display*. The second methodology, i.e., the Predictive Display, was adapted here. This is because it is more intuitive to human operators, and the onboard controller required on the mobile robot is very much simplified.

Predictive display has been defined as using the computer for extrapolating the display forward in time [76]. In this, a local model of the remote scene is used to predict and render the remote scene in response to operator's command. It replaces the delayed video feedback with extrapolated synthesised image of the remote environment. This enables the operator to perform the task normally. Predictive display has been implemented in the past using different sensors such



Figure 6.8: Kinect sensor from Microsoft

as monocular camera fixed on the wall, camera mounted on the robot arm, fusion of Lidar scanner and RGB camera, etc. The proposed approach here is to use a low-cost Kinect Sensor from Microsoft Inc. to generate the 3-D model of the remote environment and use kinematic model of the mobile robot to predict the motion of the actual robot on the 3-D model of the environment to generate a delay-free estimated image of the remote scene operator.

6.2.1 The Kinect sensor

Kinect sensor from microsoft is shown in Figure 6.8. The hardware contains a normal RGB camera, a depth sensor and a four-microphone array, which are able to provide RGB images, depth signals, and audio signals simultaneously. The depth sensor comprises of an Infra Red (IR) projector and the IR camera. The IR projector casts an IR speckle dot of known pattern into the 3-D scene while the IR camera captures the reflected IR speckles. To determine the depth, triangulation method is used. Kinect is therefore an instance of a structured light depth sensor. More details concerning the structured light 3-D imaging technology can be found in [143].

The *RGB camera* delivers three basic colour components of the video. The camera operates at 30 Hz, and can offer images at 640×480 pixels with 8 bits per channel. The *3-D Depth Sensor* creates a depth map, which provides the distance information between the camera and an object. The sensor has a practical range limit of 0.8m-3.5m distance, and outputs video at a frame rate of 30 frames/sec

with the resolution of 640 x 480 pixels. The angular field of view is 57° horizontally and 43° vertically. Number of different open source software libraries are available which includes OpenNI [144], Microsoft Kinect SDK [145] and OpenKinect [146] to access data from the Kinect sensor. OpenNi was used in this research, as it is compatible with RTabMap, an Open Source Software used for reconstruction of the 3-D point cloud model of the remote scene.

6.2.2 Onboard data processing and transmission

In teleoperation. the Kinect sensor mounted on the mobile robot was connected with the onboard Raspberry Pi single board computer with limited processing power. The onboard controller uses OpenNi library to interface with the kinect hardware. The Kinect sensor has two separate cameras. The transformation between the camera centres are known and provided by the manufacturer. It therefore generates two streams, the colour and depth data. It is possible to send the two raw data streams over the network without any processing at the robot's side. This puts less stress on the onboard computer but requires high communication bandwidth. The other option is to stream *registered depth* data over the network. This requires less bandwidth as each pixel has both the colour and depth value associated with it when it is transmitted. Depth Registration requires minimal computing power. Known transformation between the two cameras was used to align the depth pixel and the colour pixel so that they correspond to the same point of the 3-D scene. This is referred to as *depth registration* or *image registration* in the literature. The word "depth" in the *depth registration* indicates that the final image data is with respect to the depth camera's frame. The second method was adapted here. The robot transmits registered depth data, i.e., the RGB and the Depth (RGB-D) values associated with each pixel to the control station over network.

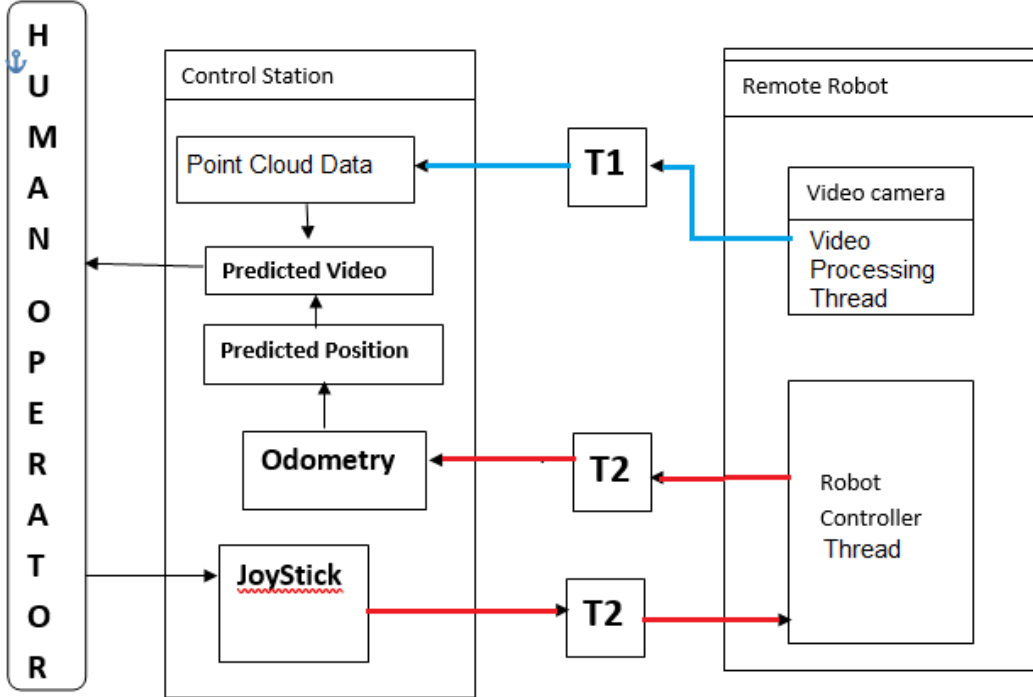


Figure 6.9: Predictive display architecture

6.2.3 3-D reconstruction

The registered depth data received at the operator-station was processed using the RTabMap library [147] and 3-D Point Cloud data was generated. The details of the working of RTabMap can be found in [148] and [149]. Point cloud map is a set of points in 3-D space derived using the camera model and the depth data associated with each pixel of the depth registered data sent from the mobile robot. Each new frame that arrives is added to the current data set after proper transformation. The transformation between the two frames of data was created by matching the common feature in the two frames. The RTabMap library thus outputs a set of 3-D point alongwith their RGB color. The coordinates of the points are always with respect to camera coordinate frame. It may be noted that the registered depth image that has arrived was delayed by T_1 unit of time. So the local station always has a 3-D map w.r.t the robot at $(t - T_1)$ sec.

6.2.4 Extrapolation of remote scene

The visual data present in the current frame is the view that the robot has seen T_1 seconds earlier. Let this data be denoted as $P(t - T_1) = \text{Set}\{P_k\}$. The point P_i is associated with the coordinates Px_k, Py_k, Pz_k and color data c_k . In order to predict the current scene that the robot might be seeing one needs to estimate the current position of the robot. The dynamic model developed in chapter 3 is used to estimate the current position of the robot. To accomplish this the architecture of the teleoperation shown in Figure 6.9 was developed and used to compensate for the time delay. It has been stated earlier that the delay T_2 in exchange of command data and the wheel velocity data from the robot to the operator station was 20ms. It may thus be assumed that using the odometric data in Equation 4.13, 4.14 and 4.15, the current position of the robot was always known to the operator-station. This was performed by Odometric Block of Figure 6.9 by using Equations 4.13, 4.14 and 4.15 from time $t - T_2$ to t . Where t denotes the current time and with initial condition

$$x(i=0) = 0, \quad y(i=0) = 0, \quad \beta(i=0) = 0$$

and

$$i = 0 \text{ to } n; \quad n = T_1/T_2$$

Let the predicted position of the robot at time t be given by

$$[x(i), \quad y(i), \quad \beta(i)] \rightarrow [v(t), y_v(t), \beta_v(t)]^T$$

This was basically the amount by which the robot has moved after the last video frame had arrived. Next, the transformation matrix, T_r^c between the mobile robot's coordinate frame at point O_r in Figure 4.10 and the camera frame was used to calculate the change in pose of the camera. Since the points P_i are in the camera

frame their current coordinates $P'x_i, P'y_i, P'z_i$ was arrived at by using

$$\begin{pmatrix} P'x_i \\ P'y_i \\ P'z_i \end{pmatrix} = T_r^c \begin{pmatrix} Px_i \\ Py_i \\ Pz_i \end{pmatrix} \quad (6.2)$$

This new location of the points were then projected onto the screen of the local operator, thus, giving him the estimated current view of the remote scene. The



Figure 6.10: PCD at time T



Figure 6.11: Predicted scene

view available at the operator station at time t is shown in Figure 6.10 which is T_1 sec old. Based on this old data, the predicted scene is shown in Figure 6.11. The operator sees Figure 6.11 instead of Figure 6.10.

With the predictive display model the operator was able to move the robot without "*wait and see*" stratagey adopted earlier. The motions were smooth and speed of operation improved.

6.3 Summary

In this chapter, the model-based predictive control for control of mobile robot over time delayed network is presented. The stability of the control was verified using simulation. This model was then adopted for teleoperation using visual feedback. Kinect sensor was used to generate the 3-D model of the remote environment in real time. The estimated position of the mobile robot using the odometry was used to project a synthesised image of the 3-D model of the remote environment.

Chapter 7

Conclusions

7.1 Thesis Summary

This thesis describes the design, development and experimentation of a customized mobile manipulator developed at Bhabha Atomic Research Centre (BARC), Mumbai, India for mapping radiation in different areas of Cyclotron building where human access is restricted during Cyclotron operation. The customized mobile manipulator is a four wheeled mobile robot with a vertical lifting platform on which the radiation detector is mounted. The mobile manipulator or platform has two rear wheels individually coupled to two motors and the front two wheels which are mutually connected using a motorized Davis steering mechanism.

The mechanical design was obtained in Chapter 3, and through optimization of steering mechanism, minimum turning radius of 415 mm was achieved while maintaining the over all size constraint of the mobile platform. The optimal location of the CG for the mobile manipulator was decided so as to provide maximum traction as well as stability over 30° ramp. Among different lifting platforms for the vertical motion to the sensor for scanning, a simple scissor based lifting platform was chosen due to several advantages it offers.

The kinematic and dynamic modeling of the customized mobile manipulator was presented in Chapter 4, where the method based on the Natural Orthogonal

Complement was used to derive the dynamic equations of motion of the wheeled mobile robot under study. This analysis highlighted the effect of caster offsets on the maneuverability of a mobile robot. The need of having a positive drive for certain castor offsets were also brought in the analysis.

Control structure for intuitive teleoperation of the mobile robot was presented in Chapter 5. This chapter proposed a user interface at the operator's side, along with the hardware and software required for the teleoperation. The control algorithm running on the robot's on-board computer was also presented. The contribution there was that it synchronizes all three motors; two in velocity control and one in position control mode (steering). In spite of difference in response time, Ackerman relation for wheel rolling was always satisfied.

The developed mobile robot was controlled by an operator who was physically separated from the mobile manipulator. A dedicated wireless network and the video signal of the remote environment from the robot's on-board camera was available. The limited bandwidth resulted in the delay of the video. Chapter 6 dealt with the simulation of a tele-operation for the mobile robot under time delay. A mathematical model of the human operator based on pure pursuit algorithm was presented. The simulation predicted instability with increase in time delay and linear velocity of the mobile robot. These studies qualitatively matched with the operator behaviour under similar conditions.

Note that the time delay in the video feedback affects the efficiency of the operator. In order to overcome this, predictive display was proposed. In Chapter 7, a new methodology was presented for the predictive display based on the 3-D model generated using the RGB-Depth data provided by a Kinect Sensor mounted on the mobile robot and the predicted position of the robot based on dynamic model of the robot presented in Chapter 4. This novel method did not require the 3-D model of the remote environment known before hand as reported in the literature earlier. This flexibility allows the tele-operation of the mobile robot in an unknown environment.

In summary, a mobile manipulator was successfully conceived, designed, assembled and controlled remotely for the purpose for which it was intended, i.e, to map the radiation of a given area.

7.2 Current Status

A prototype of mobile manipulator and its tele-operation system were manufactured and assembled at BARC, Mumbai, India based on the analysis and algorithms presented in this thesis. The robot was lab tested and the video of the same can be accessed on at the following link <https://youtu.be/B50ngfLQjo4> using the QR code shown in Figure 7.1 or <http://web.iitd.ac.in/~saha/amaren.mp4> using the QR code shown in Figure 7.2 . The system will shortly be deployed at Variable Energy Cyclotron Centre (VECC) at Kolkata, India for the same purpose.



Figure 7.1: QR code Youtube



Figure 7.2: QR Code alternate

7.3 Future Scope

The testing and evaluation of teleoperation system during actual trial opened up further scope of improvement. Few of these are listed below:

- (i) Detection of slip and estimation of slip parameters using inertial sensors such as gyroscope and accelerometer mounted on the mobile robot in combination with wheel odometer.

Several algorithm are available in the literature which uses sensor fusion to arrive at better estimation of robots pose. This estimated pose can then

be used to calculate the estimated real time slip based on the actual wheels encoder readings. Based on the estimated slip and using the slip model presented in Section 3.4.3, actual slip parameters can then be estimated.

- (ii) Pose estimation using encoder mounted on the front passive wheels for slip detection.

The two front wheel are passive wheel, which in general will undergo less slip than the actuated wheels. On flat terrain and with wheels with low inertia they can give a better estimate of the robots position. Since the contact point of the two wheel keep changing with respect to the robot body an algorithm based on kinematics of the steering linkage can be worked out to give the position of the robot body based on the odometry of theses wheels. It needs to be seen if this in combination with the inertial sensors can produce better estimate.

- (iii) Semi-automated navigation using intermediate goal point.

In this mode the operator will give goal point/s on the screen. This 2D point on the screen would then be mapped to the 3-D point in the actual environment. A planing algorithm will then generate a path between the current position of the robot and goal point. This path must to satisfy the minimum turning radius constrain of the mobile robot. This path will then be feedback to the robots on board controller. A local tracking controller will then be activated to track the path.

- (iv) Texture mapping of predicted visual image instead of 3-D point cloud model currently used.

Since the color of the environment is also available along with its distance an algorithm needs be developed or existing algorithm implemented which will use the 3-D point cloud which contains the distance information and the colour to produce surface with texture. This will give a more natural feel of the environment to the operator.

- (v) Force feedback to the operator for estimation of obstacle location in the remote environment.

This can be achieved using ultrasonic sensors mounted on the periphery of the robot. Once obstacles comes too close to the robot, the distance of the obstacle from the robot will be transmitted to the control station. The software at the operator side then will give some vibratory input to the steering wheel. The amplitude of vibration should be function of the distance of the robot from the obstacle, the heading direction and the speed of approach. A proper function to give intuitive feel to the operator has to be worked out.

Bibliography

- [1] K. Ohno, S. Kawatsuma, T. Okada, E. Takeuchi, K. Higashi, and S. Tadokoro, “Robotic control vehicle for measuring radiation in fukushima daiichi nuclear power plant,” in *Safety, Security, and Rescue Robotics (SSRR), 2011 IEEE International Symposium on*, pp. 38–43, IEEE, 2011.
- [2] B. L. Luk, K. Liu, A. A. Collie, D. S. Cooke, and S. Chen, “Tele-operated climbing and mobile service robots for remote inspection and maintenance in nuclear industry,” *Industrial Robot: An International Journal*, vol. 33, no. 3, pp. 194–204, 2006.
- [3] L. Ray, A. Price, A. Streeter, D. Denton, and J. H. Lever, “The design of a mobile robot for instrument network deployment in antarctica,” in *Robotics and Automation, 2005. ICRA 2005. Proceedings of the 2005 IEEE International Conference on*, pp. 2111–2116, IEEE, 2005.
- [4] L. Briones, P. Bustamante, and M. A. Serna, “Wall-climbing robot for inspection in nuclear power plants,” in *Robotics and Automation, 1994. Proceedings., 1994 IEEE International Conference on*, pp. 1409–1414, IEEE, 1994.
- [5] S. Galt, B. Luk, D. Cooke, and A. Collie, “A tele-operated semi-intelligent climbing robot for nuclear applications,” in *Mechatronics and Machine Vision in Practice, 1997. Proceedings., Fourth Annual Conference on*, pp. 118–123, IEEE, 1997.
- [6] C.-S. Cho, J.-D. Kim, S.-G. Lee, S. K. Lee, S.-C. Han, and B.-S. Kim, “A study on automated mobile painting robot with permanent magnet wheels for outer plate of ship,” in *Robotics (ISR), 2013 44th International Symposium on*, pp. 1–4, IEEE, 2013.
- [7] J. Borenstein, “Control and kinematic design of multi-degree-of freedom mobile robots with compliant linkage,” *IEEE Transactions on Robotics and Automation*, vol. 11, no. 1, pp. 21–35, 1995.
- [8] Y. P. Li, T. Zielinska, M. Ang, and W. Lin, “Wheel-ground interaction modelling and torque distribution for a redundant mobile robot,” in *Proceedings 2006 IEEE International Conference on Robotics and Automation, 2006. ICRA 2006.*, pp. 3362–3367, IEEE, 2006.
- [9] P. F. Muir and C. P. Neuman, “Kinematic modeling of wheeled mobile robots,” *Journal of Robotic Systems*, vol. 4, no. 2, pp. 281–340, 1987.

- [10] B.-J. Yi and W. K. Kim, “The kinematics for redundantly actuated omnidirectional mobile robots,” *Journal of Robotic Systems*, vol. 19, no. 6, pp. 255–267, 2002.
- [11] L.-C. Lin and H.-Y. Shih, “Modeling and adaptive control of an omnimecanum-wheeled robot,” *Intelligent Control and Automation*, vol. 4, no. 02, p. 166, 2013.
- [12] O. Diegel, A. Badve, G. Bright, J. Potgieter, and S. Tlale, “Improved mecanum wheel design for omni-directional robots,” in *Proc. 2002 Australasian Conference on Robotics and Automation, Auckland*, pp. 117–121, 2002.
- [13] H. Taheri, B. Qiao, and N. Ghaeminezhad, “Kinematic model of a four mecanum wheeled mobile robot,” *International Journal of Computer Applications*, vol. 113, no. 3, pp. 6–9, 2015.
- [14] D. Oetomo and M. H. Ang, “Singularity-free joint actuation in omnidirectional mobile platforms with powered offset caster wheels,” *Journal of Mechanical Design*, vol. 130, no. 5, p. 054501, 2008.
- [15] W. Chung, C.-b. Moon, C. Jung, and J. Jin, “Design of the dual offset active caster wheel for holonomic omni-directional mobile robots,” *International Journal of Advanced Robotic Systems*, vol. 7, no. 4, p. 26, 2010.
- [16] G. Witus, “Mobility potential of a robotic six-wheeled omnidirectional drive vehicle ODV with z-axis and tire inflation control,” in *Proceedings SPIE , Unmanned Ground Vehicle Technology II* (G. R. Gerhart, R. W. Gunderson, and C. M. Shoemaker, eds.), vol. 4024, pp. 106–114, International Society for Optics and Photonics, 2000.
- [17] K. L. Moore, M. Davidson, V. Bahl, S. Rich, and S. Jirgal, “Modelling and control of a six-wheeled autonomous robot,” in *Proceedings of the 2000 American Control Conference. ACC (IEEE Cat. No. 00CH36334)*, vol. 3, pp. 1483–1490, IEEE, 2000.
- [18] T. B. Park, J. H. Lee, B.-J. Yi, W. K. Kim, B. J. You, and S.-R. Oh, “Optimal design and actuator sizing of redundantly actuated omni-directional mobile robots,” in *Proceedings 2002 IEEE International Conference on Robotics and Automation (Cat. No. 02CH37292)*, vol. 1, pp. 732–737, IEEE, 2002.
- [19] J. C. Alexander and J. H. Maddocks, “On the kinematics of wheeled mobile robots,” *The International Journal of Robotics Research*, vol. 8, no. 5, pp. 15–27, 1989.
- [20] G. Campion, G. Bastin, and B. Dandrea-Novel, “Structural properties and classification of kinematic and dynamic models of wheeled mobile robots,” *IEEE Transactions on Robotics and Automation*, vol. 12, no. 1, pp. 47–62, 1996.
- [21] N. A. M. Hootsmans, *The Motion Control Manipulators on Mobile Vehicles*. PhD thesis, Massachusetts Institute of Technology, 1992.

- [22] J. H. Chung, S. A. Velinsky, and R. A. Hess, "Interaction control of a redundant mobile manipulator," *The International Journal of Robotics Research*, vol. 17, no. 12, pp. 1302–1309, 1998.
- [23] J. Y. Luh, M. W. Walker, and R. P. Paul, "On-line computational scheme for mechanical manipulators," *Journal of Dynamic Systems, Measurement, and Control*, vol. 102, no. 2, pp. 69–76, 1980.
- [24] F. Boyer and S. Ali, "Recursive inverse dynamics of mobile multibody systems with joints and wheels," *IEEE Transactions on Robotics*, vol. 27, no. 2, pp. 215–228, 2011.
- [25] J. Angeles and S. K. Lee, "The formulation of dynamical equations of holonomic mechanical systems using a natural orthogonal complement," *Journal of Applied Mechanics*, vol. 55, p. 243, 1988.
- [26] J. Angeles, *Fundamentals of Robotic Mechanical Systems: Theory, Methods, and Algorithms*, vol. 124. Springer Science & Business Media, 2013.
- [27] S. K. Saha and J. Angeles, "Kinematics and dynamics of a three-wheeled 2-DOF AGV," in *Robotics and Automation, 1989. Proceedings., 1989 IEEE International Conference on*, pp. 1572–1577, IEEE, 1989.
- [28] S. K. Saha and J. Angeles, "Dynamics of nonholonomic mechanical systems using a natural orthogonal complement," *Journal of Applied Mechanics*, vol. 58, no. 1, pp. 238–243, 1991.
- [29] R. L. Williams, B. E. Carter, P. Gallina, and G. Rosati, "Dynamic model with slip for wheeled omnidirectional robots," *IEEE Transactions on Robotics and Automation*, vol. 18, no. 3, pp. 285–293, 2002.
- [30] R. Balakrishna and A. Ghosal, "Modeling of slip for wheeled mobile robots," *IEEE Transactions on Robotics and Automation*, vol. 11, no. 1, pp. 126–132, 1995.
- [31] H. Khan, J. Iqbal, K. Baizid, and T. Zielinska, "Longitudinal and lateral slip control of autonomous wheeled mobile robot for trajectory tracking," *Frontiers of Information Technology & Electronic Engineering*, vol. 16, no. 2, pp. 166–172, 2015.
- [32] J. Dakhllallah, S. Glaser, S. Mammar, and Y. Sebsadji, "Tire-road forces estimation using extended kalman filter and sideslip angle evaluation," in *2008 American Control Conference*, pp. 4597–4602, IEEE, 2008.
- [33] Y. Liu, Y. Jia, and N. Xi, "Dynamic model and adaptive tracking controller for 4-powered caster vehicle," in *2010 IEEE International Conference on Robotics and Automation*, pp. 4940–4945, IEEE, 2010.
- [34] Y. Tian, N. Sidek, and N. Sarkar, "Modeling and control of a nonholonomic wheeled mobile robot with wheel slip dynamics," in *2009 IEEE Symposium on Computational Intelligence in Control and Automation*, pp. 7–14, IEEE, 2009.

- [35] S. N. Sidek, *Dynamic Modeling and Control of Nonholonomic Wheeled Mobile Robot Subjected to Wheel Slip*. PhD thesis, Vanderbilt University, 2008.
- [36] S. Konduri, E. Orlando, C. Torres, and P. R. Pagilla, “Effect of wheel slip in the coordination of wheeled mobile robots,” in *Proceedings of the 19th World Congress the International Federation of Automatic Control*, vol. 47, pp. 8097–8102, IFAC, 2014.
- [37] L. Ojeda, D. Cruz, G. Reina, and J. Borenstein, “Current-based slippage detection and odometry correction for mobile robots and planetary rovers,” *IEEE Transactions on Robotics*, vol. 22, no. 2, pp. 366–378, 2006.
- [38] C. Lee, K. Hedrick, and K. Yi, “Real-time slip-based estimation of maximum tire-road friction coefficient,” *IEEE/ASME Transactions on Mechatronics*, vol. 9, no. 2, pp. 454–458, 2004.
- [39] W. Buchele, L. Xie, *et al.*, “Computer analysis of the lateral stability of agricultural tractors.,” *Paper-American Society of Agricultural Engineers*, no. 90-1589, 1990.
- [40] I. S. Jones and M. B. Penny, “Engineering parameters related to rollover frequency,” tech. rep., SAE Technical Paper, 1990.
- [41] S. Dubowsky and E. Vance, “Planning mobile manipulator motions considering vehicle dynamic stability constraints,” in *Proceedings, 1989 International Conference on Robotics and Automation*, pp. 1271–1276, IEEE, 1989.
- [42] R. B. McGhee and A. A. Frank, “On the stability properties of quadruped creeping gaits,” *Mathematical Biosciences*, vol. 3, pp. 331–351, 1968.
- [43] M. Vukobratovic and D. Juricic, “Contribution to the synthesis of biped gait,” *IEEE Transactions on Biomedical Engineering*, no. 1, pp. 1–6, 1969.
- [44] M. Vukobratovic, B. Borovac, D. Surla, and D. Stokic, *Biped Locomotion: Dynamics, Stability, Control and Application*, vol. 7. Springer Science & Business Media, 2012.
- [45] A. Ollero and G. Heredia, “Stability analysis of mobile robot path tracking,” in *Intelligent Robots and Systems 95.'Human Robot Interaction and Cooperative Robots', Proceedings. 1995 IEEE/RSJ International Conference on*, vol. 3, pp. 461–466, IEEE, 1995.
- [46] Q. Huang and S. Sugano, “Manipulator motion planning for stabilizing a mobile-manipulator,” in *Proceedings 1995 IEEE/RSJ International Conference on Intelligent Robots and Systems. Human Robot Interaction and Cooperative Robots*, vol. 3, pp. 467–472, IEEE, 1995.
- [47] Q. Huang, S. Sugano, and I. Kato, “Stability control for a mobile manipulator using a potential method,” in *Proceedings of IEEE/RSJ International Conference on Intelligent Robots and Systems (IROS'94)*, vol. 2, pp. 839–846, IEEE, 1994.

- [48] S. Sugano, Q. Huang, and I. Kato, “Stability criteria in controlling mobile robotic systems,” in *Proceedings of 1993 IEEE/RSJ International Conference on Intelligent Robots and Systems (IROS'93)*, vol. 2, pp. 832–838, IEEE, 1993.
- [49] S. Furuno, M. Yamamoto, and A. Mohri, “Trajectory planning of mobile manipulator with stability considerations,” in *2003 IEEE International Conference on Robotics and Automation (Cat. No. 03CH37422)*, vol. 3, pp. 3403–3408, IEEE, 2003.
- [50] D. Messuri and C. Klein, “Automatic body regulation for maintaining stability of a legged vehicle during rough-terrain locomotion,” *IEEE Journal on Robotics and Automation*, vol. 1, no. 3, pp. 132–141, 1985.
- [51] A. Ghasempoor and N. Sepehri, “A measure of machine stability for moving base manipulators,” in *Proceedings of 1995 IEEE International Conference on Robotics and Automation*, vol. 3, pp. 2249–2254, IEEE, 1995.
- [52] E. Papadopoulos and D. A. Rey, “A new measure of tipover stability margin for mobile manipulators,” in *Proceedings of IEEE International Conference on Robotics and Automation*, vol. 4, pp. 3111–3116, IEEE, 1996.
- [53] E. Papadopoulos and D. A. Rey, “The force-angle measure of tipover stability margin for mobile manipulators,” *Vehicle System Dynamics*, vol. 33, no. 1, pp. 29–48, 2000.
- [54] R. C. Coulter, “Implementation of the pure pursuit path tracking algorithm,” tech. rep., Carnegie-Mellon University, Robotics Institute, Pittsburgh, USA, 1992.
- [55] M. J. Barton, “Controller development and implementation for path planning and following in an autonomous urban vehicle,” *Master's thesis, Australian Centre for Field Robotics, School of Aerospace, Mechanical and Mechatronic Engineering, University of Sydney*, 2001.
- [56] J. Wit, C. D. Crane III, and D. Armstrong, “Autonomous ground vehicle path tracking,” *Journal of Robotic Systems*, vol. 21, no. 8, pp. 439–449, 2004.
- [57] T. Hellstrom and O. Ringdahl, “Follow the past: a path-tracking algorithm for autonomous vehicles,” *International Journal of Vehicle Autonomous Systems*, vol. 4, no. 2, pp. 216–224, 2006.
- [58] B. Paden, M. Čáp, S. Z. Yong, D. Yershov, and E. Frazzoli, “A survey of motion planning and control techniques for self-driving urban vehicles,” *IEEE Transactions on Intelligent Vehicles*, vol. 1, no. 1, pp. 33–55, 2016.
- [59] O. Khatib, “Real-time obstacle avoidance for manipulators and mobile robots,” in *Proceedings. 1985 IEEE International Conference on Robotics and Automation*, vol. 2, pp. 500–505, IEEE, 1985.
- [60] O. Khatib, “Commande dynamique dans l'espace opérationnel des robots manipulateurs en présence d'obstacles,” *PhD thesis, Ecole Nationale Supérieure de l'Aeronautique et de l'Espace*, 1980.

- [61] J. Latombe, *Robot Motion Planning*, vol. 124. Springer Science & Business Media, 2012.
- [62] L. Tang, S. Dian, G. Gu, K. Zhou, S. Wang, and X. Feng, “A novel potential field method for obstacle avoidance and path planning of mobile robot,” in *2010 3rd International Conference on Computer Science and Information Technology*, vol. 9, pp. 633–637, IEEE, 2010.
- [63] M. G. Park, J. H. Jeon, and M. C. Lee, “Obstacle avoidance for mobile robots using artificial potential field approach with simulated annealing,” in *ISIE 2001. 2001 IEEE International Symposium on Industrial Electronics Proceedings*, vol. 3, pp. 1530–1535, IEEE, 2001.
- [64] J. Borenstein and Y. Koren, “Real-time obstacle avoidance for fast mobile robots,” *IEEE Transactions on Systems, Man, and Cybernetics*, vol. 19, no. 5, pp. 1179–1187, 1989.
- [65] J. Borenstein and Y. Koren, “The vector field histogram-fast obstacle avoidance for mobile robots,” *IEEE Transactions on Robotics and Automation*, vol. 7, no. 3, pp. 278–288, 1991.
- [66] I. Ulrich and J. Borenstein, “VFH+: Reliable obstacle avoidance for fast mobile robots,” in *Proceedings. 1998 IEEE International Conference on Robotics and Automation*, vol. 2, pp. 1572–1577, IEEE, 1998.
- [67] O. Brock and O. Khatib, “High-speed navigation using the global dynamic window approach,” in *Proceedings 1999 IEEE International Conference on Robotics and Automation*, vol. 1, pp. 341–346, IEEE, 1999.
- [68] J. Minguez and L. Montano, “Nearness diagram (ND) navigation: collision avoidance in troublesome scenarios,” *IEEE Transactions on Robotics and Automation*, vol. 20, no. 1, pp. 45–59, 2004.
- [69] S. Garrido, L. Moreno, and D. Blanco, “Voronoi diagram and fast marching applied to path planning,” in *Proceedings 2006 IEEE International Conference on Robotics and Automation, 2006. ICRA 2006.*, pp. 3049–3054, IEEE, 2006.
- [70] F. Duchoň, A. Babinec, M. Kajan, P. Beňo, M. Florek, T. Fico, and L. Jurišica, “Path planning with modified a star algorithm for a mobile robot,” *Procedia Engineering*, vol. 96, pp. 59–69, 2014.
- [71] N. J. Nilsson, “A mobile automaton: An application of artificial intelligence techniques,” tech. rep., Stanford Research Institute, Artificial Intelligence Center, Menlo Park, California, USA, 1969.
- [72] P. Bhattacharya and M. L. Gavrilova, “Roadmap-based path planning-using the voronoi diagram for a clearance-based shortest path,” *IEEE Robotics & Automation Magazine*, vol. 15, no. 2, pp. 58–66, 2008.
- [73] O. Takahashi and R. J. Schilling, “Motion planning in a plane using generalized voronoi diagrams,” *IEEE Transactions on Robotics and Automation*, vol. 5, no. 2, pp. 143–150, 1989.

- [74] H. L. Martin and D. P. Kuban, *Teleoperated Robotics in Hostile Environments*. Society of Manufacturing Engineers, 1985.
- [75] J. Vertut and P. Coiffet, *Teleoperations and Robotics: Evolution and Development of Robot Technology, vol. 3A*. Englewood Cliffs, NJ: Prentice-Hall, Inc, 1986.
- [76] T. B. Sheridan, “Space teleoperation through time delay: Review and prognosis,” *IEEE Transactions on Robotics and Automation*, vol. 9, no. 5, October 1993.
- [77] T. H. Massie, J. K. Salisbury, *et al.*, “The phantom haptic interface: A device for probing virtual objects,” in *Proceedings of the ASME Winter Annual Meeting, Symposium on Haptic Interfaces for Virtual Environment and Teleoperator Systems*, vol. 55,1, pp. 295–300, Citeseer, 1994.
- [78] S. Grange, F. Conti, P. Helmer, P. Rouiller, and C. Baur, “Overview of the delta haptic device,” tech. rep., Institut de Systèmes Robotiques, Ecole Polytechnique Fédérale de Lausanne, 1015 Lausanne, Switzerland, 2001.
- [79] C. Clover, G. R. Luecke, J. J. Troy, and W. A. McNeely, “Dynamic simulation of virtual mechanisms with haptic feedback using industrial robotics equipment,” in *Robotics and Automation, 1997. Proceedings., 1997 IEEE International Conference on*, vol. 1, pp. 724–730, IEEE, 1997.
- [80] M. Ueberle, N. Mock, and M. Buss, “Vishard-10, a novel hyper-redundant haptic interface,” in *Haptic Interfaces for Virtual Environment and Teleoperator Systems, 2004. HAPTICS’04. Proceedings. 12th International Symposium on*, pp. 58–65, IEEE, 2004.
- [81] J. Yoon and J. Ryu, “Design, fabrication, and evaluation of a new haptic device using a parallel mechanism,” *IEEE/ASME Transactions on Mechatronics*, vol. 6, no. 3, pp. 221–233, 2001.
- [82] R. Aracil, M. Ferre, M. Hernando, and J. Sebastian, “Telerobotic system for live-power line maintenance: Robtet,” *IEEE Transactions on Industrial Electronics*, vol. 44, no. 5-44, pp. 630–637, 1997.
- [83] L. Matthies, “Stereo vision for planetary rovers: Stochastic modeling to near real-time implementation,” *International Journal of Computer Vision*, vol. 8, no. 1, pp. 71–91, 1992.
- [84] G. Hirzinger, “Robots in space-a survey,” *Advanced Robotics*, vol. 9, no. 6, pp. 625–651, 1994.
- [85] R. Goertz, R. Blomgren, J. Grimson, G. Forster, W. Thompson, and W. Kline, “The ANL model 3 master-slave electric manipulator—its design and use in a cave,” *Trans. Am. Nuclear Soc.*, vol. 4, no. 2, 1961.
- [86] C. Flatau, “SM-229: A new compact servo master-slave manipulator,” in *Proceedings of the 25th Conference on Remote Systems Technology*, 1977.

- [87] D. A. Lawrence, “Stability and transparency in bilateral teleoperation,” *IEEE Transactions on Robotics and Automation*, vol. 9, no. 5, pp. 624–637, 1993.
- [88] P. F. Hokayem and M. W. Spong, “Bilateral teleoperation: An historical survey,” *Automatica*, vol. 42, no. 12, pp. 2035–2057, 2006.
- [89] R. J. Anderson and M. W. Spong, “Bilateral control of teleoperators with time delay,” *IEEE Transactions on Automatic Control*, vol. 34, no. 5, pp. 494–501, 1989.
- [90] J. Rebelo and A. Schiele, “Time domain passivity controller for 4-channel time-delay bilateral teleoperation,” *IEEE Transactions on Haptics*, vol. 8, no. 1, pp. 79–89, 2015.
- [91] G. Niemeyer and J.-J. Slotine, “Stable adaptive teleoperation,” *IEEE Journal of Oceanic Engineering*, vol. 16, no. 1, pp. 152–162, 1991.
- [92] S. Stramigioli, R. Mahony, and P. Corke, “A novel approach to haptic teleoperation of aerial robot vehicles,” in *Robotics and Automation (ICRA), 2010 IEEE International Conference on*, pp. 5302–5308, IEEE, 2010.
- [93] S. Stramigioli, C. Secchi, A. J. van der Schaft, and C. Fantuzzi, “Sampled data systems passivity and discrete port-hamiltonian systems,” *IEEE Transactions on Robotics*, vol. 21, no. 4, pp. 574–587, 2005.
- [94] M. Krstic, *Delay Compensation for Nonlinear, Adaptive, and PDE Systems*. Springer, 2009.
- [95] J. Y. Chen, E. C. Haas, and M. J. Barnes, “Human performance issues and user interface design for teleoperated robots,” *IEEE Transactions on Systems, Man, and Cybernetics, Part C (Applications and Reviews)*, vol. 37, no. 6, pp. 1231–1245, 2007.
- [96] T. Sheridan, “Human supervisory control of robot systems,” in *Robotics and Automation. Proceedings. 1986 IEEE International Conference on*, vol. 3, pp. 808–812, IEEE, 1986.
- [97] P. K. Pook and D. H. Ballard, “Teleassistance: Contextual guidance for autonomous manipulation,” in *AAAI-94. Proceedings.*, pp. 1291–1296, 1994.
- [98] M. Jagersand and R. Nelson, “Visual space task specification, planning and control,” in *Computer Vision, 1995. Proceedings., International Symposium on*, pp. 521–526, IEEE, 1995.
- [99] T. B. Sheridan, “Space teleoperation through time delay: Review and prognosis,” *IEEE Transactions on Robotics and Automation*, vol. 9, no. 5, pp. 592–606, 1993.
- [100] A. K. Bejczy and W. S. Kim, “Predictive displays and shared compliance control for time-delayed telemanipulation,” in *Intelligent Robots and Systems' 90.'Towards a New Frontier of Applications', Proceedings. IROS'90. IEEE International Workshop on*, pp. 407–412, IEEE, 1990.

- [101] W. S. Kim and A. K. Bejczy, “Demonstration of a high-fidelity predictive/preview display technique for telerobotic servicing in space,” *IEEE Transactions on Robotics and Automation*, vol. 9, no. 5, pp. 698–702, 1993.
- [102] M. Jagersand, “Image based predictive display for tele-manipulation,” in *Robotics and Automation, 1999. Proceedings. 1999 IEEE International Conference on*, vol. 1, pp. 550–556, IEEE, 1999.
- [103] K. Yerex, D. Cobzas, and M. Jagersand, “Predictive display models for tele-manipulation from uncalibrated camera-capture of scene geometry and appearance,” in *Robotics and Automation, 2003. Proceedings. ICRA ’03. IEEE International Conference on*, vol. 2, pp. 2812–2817, IEEE, 2003.
- [104] Z. Deng and M. Jagersand, “Predictive display system for tele-manipulation using image-based modeling and rendering,” in *Intelligent Robots and Systems, 2003.(IROS 2003). Proceedings. 2003 IEEE/RSJ International Conference on*, vol. 3, pp. 2797–2802, IEEE, 2003.
- [105] A. Kelly, N. Chan, H. Herman, D. Huber, R. Meyers, P. Rander, R. Warner, J. Ziglar, and E. Capstick, “Real-time photorealistic virtualized reality interface for remote mobile robot control,” *The International Journal of Robotics Research*, vol. 30, no. 3, pp. 384–404, 2011.
- [106] T. Burkert, J. Leupold, and G. Passig, “A photorealistic predictive display,” *Presence: Teleoperators & Virtual Environments*, vol. 13, no. 1, pp. 22–43, 2004.
- [107] H. Hu, C. P. Quintero, H. Sun, and M. Jagersand, “On-line reconstruction based predictive display in unknown environment,” in *Robotics and Automation (ICRA), 2015 IEEE International Conference on*, pp. 4446–4451, IEEE, 2015.
- [108] T. Bevan, *Theory of Machines, Third Edition*. Delhi, India: CBS Publishers & Distributors, 1984.
- [109] Y. Yamamoto and X. Yun, “Coordinating locomotion and manipulation of a mobile manipulator,” in *Decision and Control, 1992., Proceedings of the 31st IEEE Conference on*, pp. 2643–2648, IEEE, 1992.
- [110] S. Rajendran and et.al., “Mobile robot for reactor vessel inspection,” in *National Conference on Advanced Manufacturing and Robotics*, pp. 2527–2532, CMERI, Durgapur, WB,, 2004.
- [111] F. G. Pin and S. M. Killough, “A new family of omnidirectional and holonomic wheeled platforms for mobile robots,” *IEEE Transactions on Robotics and Automation*, vol. 10, no. 4, pp. 480–489, 1994.
- [112] J. E. M. Salih, M. Rizon, S. Yaacob, A. H. Adom, and M. R. Mamat, “Designing omni-directional mobile robot with mecanum wheel,” *American Journal of Applied Sciences*, vol. 3, no. 5, pp. 1831–1835, 2006.

- [113] J. Suthakorn, S. S. H. Shah, S. Jantarajit, W. Onprasert, W. Saensupo, S. Saeung, S. Nakdhamabhorn, V. Sa-Ing, and S. Reaungamornrat, “On the design and development of a rough terrain robot for rescue missions,” in *Robotics and Biomimetics, 2008. ROBIO 2008. IEEE International Conference on*, pp. 1830–1835, IEEE, 2009.
- [114] M. Guarnieri, R. Debenest, T. Inoh, E. Fukushima, and S. Hirose, “Development of Helios VII: an arm-equipped tracked vehicle for search and rescue operations,” in *Intelligent Robots and Systems, 2004.(IROS 2004). Proceedings. 2004 IEEE/RSJ International Conference on*, vol. 1, pp. 39–45, IEEE, 2004.
- [115] K. Nagatani, S. Tachibana, M. Sofne, and Y. Tanaka, “Improvement of odometry for omnidirectional vehicle using optical flow information,” in *Intelligent Robots and Systems, 2000.(IROS 2000). Proceedings. 2000 IEEE/RSJ International Conference on*, vol. 1, pp. 468–473, IEEE, 2000.
- [116] H. P. Moravec, “The CMU rover.,” in *AAAI*, pp. 377–380, 1982.
- [117] H. P. Moravec, “The Stanford cart and the CMU rover,” *Proceedings of the IEEE*, vol. 71, no. 7, pp. 872–884, 1983.
- [118] S. K. Saha, J. Angeles, and J. Darcovich, “The design of kinematically isotropic rolling robots with omnidirectional wheels,” *Mechanism and Machine Theory*, vol. 30, no. 8, pp. 1127–1137, 1995.
- [119] J. Carlson and R. R. Murphy, “How UGVs physically fail in the field,” *IEEE Transactions on Robotics*, vol. 21, no. 3, pp. 423–437, 2005.
- [120] K. H. Low and Y. Leow, “Kinematic modeling, mobility analysis and design of wheeled mobile robots,” *Advanced Robotics*, vol. 19, no. 1, pp. 73–99, 2005.
- [121] *Motor Catalogue 2014*. Switzerland: Maxon Motors, 2017.
- [122] J. T. Machado and M. F. Silva, “An overview of legged robots,” in *International Symposium on Mathematical Methods in Engineering*, MME Press Ankara, Turkey, 2006.
- [123] K. P. Valavanis and G. J. Vachtsevanos, *Handbook of Unmanned Aerial Vehicles*. Springer Publishing Company, Incorporated, 2014.
- [124] J.-B. Mouret, *Evolutionary Adaptation in Natural and Artificial Systems*. PhD thesis, Université Pierre et Marie Curie, 2015.
- [125] G. Campion and W. Chung, “Wheeled robots,” in *Springer Handbook of Robotics*, pp. 391–410, Springer, 2008.
- [126] R. M. DeSantis, “Modeling and path-tracking control of a mobile wheeled robot with a differential drive,” *Robotica*, vol. 13, no. 04, pp. 401–410, 1995.

- [127] K. C. Koh and H. S. Cho, “A smooth path tracking algorithm for wheeled mobile robots with dynamic constraints,” *Journal of Intelligent & Robotic Systems*, vol. 24, no. 4, pp. 367–385, 1999.
- [128] B. d’Andrea Novel, G. Campion, and G. Bastin, “Control of nonholonomic wheeled mobile robots by state feedback linearization,” *The International Journal of Robotics Research*, vol. 14, no. 6, pp. 543–559, 1995.
- [129] B. d’Andrea Novel, G. Bastin, and G. Campion, “Modelling and control of non-holonomic wheeled mobile robots,” in *Robotics and Automation, 1991. Proceedings., 1991 IEEE International Conference on*, pp. 1130–1135, IEEE, 1991.
- [130] K. Thanjavur and R. Rajagopalan, “Ease of dynamic modelling of wheeled mobile robots WMRs using kane’s approach,” in *Robotics and Automation, 1997. Proceedings., 1997 IEEE International Conference on*, vol. 4, pp. 2926–2931, IEEE, 1997.
- [131] S. Saha, *Introduction to Robotics*. Tata McGraw-Hill, New Delhi, 2010.
- [132] D. Wang and C. B. Low, “Modeling and analysis of skidding and slipping in wheeled mobile robots: Control design perspective,” *IEEE Transactions on Robotics*, vol. 24, no. 3, pp. 676–687, 2008.
- [133] H. B. Pacejka and E. Bakker, “The magic formula tyre model,” *Vehicle System Dynamics*, vol. 21, no. S1, pp. 1–18, 1992.
- [134] X. Claeys, J. Yi, L. Alvarez, R. Horowitz, and C. C. De Wit, “A dynamic tire/road friction model for 3D vehicle control and simulation,” in *2001 IEEE Intelligent Transportation Systems. Proceedings (Cat. No. 01TH8585)*, pp. 483–488, IEEE, 2001.
- [135] B. T. Kulakowski, “Mathematical model of skid resistance as a function of speed,” *Transportation Research Record*, no. 1311, 1991.
- [136] H. Dugoff, P. Fancher, and L. Segel, “An analysis of tire traction properties and their influence on vehicle dynamic performance,” *SAE Transactions*, pp. 1219–1243, 1970.
- [137] J. J. Craig, *Introduction to Robotics: Mechanics and Control*, vol. 3. Pearson/Prentice Hall Upper Saddle River, NJ, USA:, 2005.
- [138] *EPOS Application Note: RS232 to CAN-open Getway*. Maxon Motors, 2012.
- [139] I. Farkhatdinov and J.-H. Ryu, “Hybrid position-position and position-speed command strategy for the bilateral teleoperation of a mobile robot,” in *Control, Automation and Systems, 2007. ICCAS’07. International Conference on*, pp. 2442–2447, IEEE, 2007.
- [140] M. Z. Zeroual, “Maxon auto tuning,” *iNaCoMM2013, IIT Roorkee, India*, 2013.
- [141] *EPOS4 Application Note: Positioning Controllers*. Maxon Motors, 2012.

- [142] O. J. Smith, “A controller to overcome dead time,” *ISA J.*, vol. 6, pp. 28–33, 1959.
- [143] J. Geng, “Structured-light 3D surface imaging: a tutorial,” *Advances in Optics and Photonics*, vol. 3, no. 2, pp. 128–160, 2011.
- [144] “Openni [online].” <http://www.openni.org/>. Accessed: 2018-09-30.
- [145] “Microsoft kinect sdk [online]..” <https://www.microsoft.com/en-hk/download/details.aspx?id=44561>. Accessed: 2018-09-30.
- [146] “Openkinect [online]..” <https://github.com/OpenKinect/libfreenect/>. Accessed: 2018-09-30.
- [147] “Rtabmap [online].” <https://github.com/introlab/rtabmap>. Accessed: 2018-09-30.
- [148] M. Labb  and F. Michaud, “RTAB-Map as an open-source lidar and visual simultaneous localization and mapping library for large-scale and long-term online operation,” *Journal of Field Robotics*, vol. 36, no. 2, pp. 416–446, 2019.
- [149] M. Labbe and F. Michaud, “Appearance-based loop closure detection for online large-scale and long-term operation,” *IEEE Transactions on Robotics*, vol. 29, no. 3, pp. 734–745, 2013.

Appendix A

A.1 Measurement of Time Delay in Video Feed-back

The experiment used to find the time delay in video feedback is described here. The operator station's graphical user interface is shown in Figure A.1. This displays the video received from the camera mounted on the mobile robot in the window marked with a green boundary.

To measure the time delay, a digital clock and the user interface runs side by side on the operator screen. The camera on the robot is now oriented to face the user interface, so that the camera captures the video of the digital clock running on the user PC. The schematic of the experimental set-up is shown in Figure A.2. The screen shot of the operator screen is shown in Figure A.3. The red box marks the clock running on the PC. The blue box marks the time captured by the robot camera in the most recent video frame received at the operator station. We thus see the delay of $9.2 - 8.7 = 0.5$ sec, for the video frame to travel from robot to the operator station. This delay includes both the processing time and the transmission time.

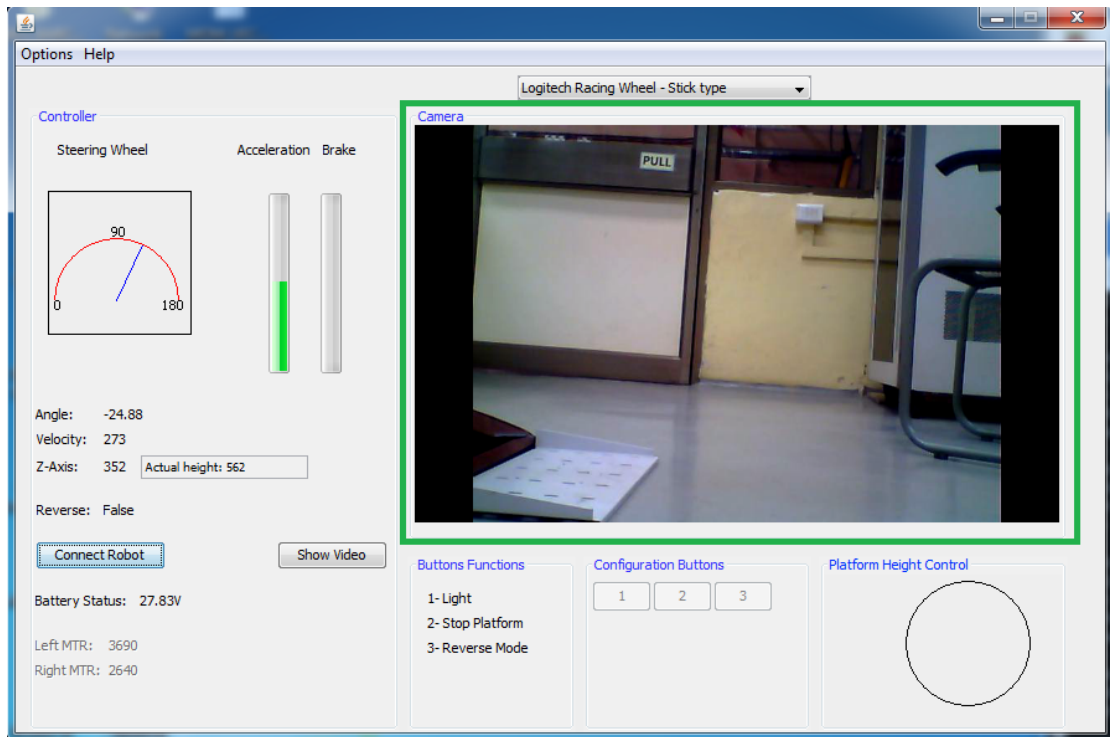


Figure A.1: User interface for teleoperation

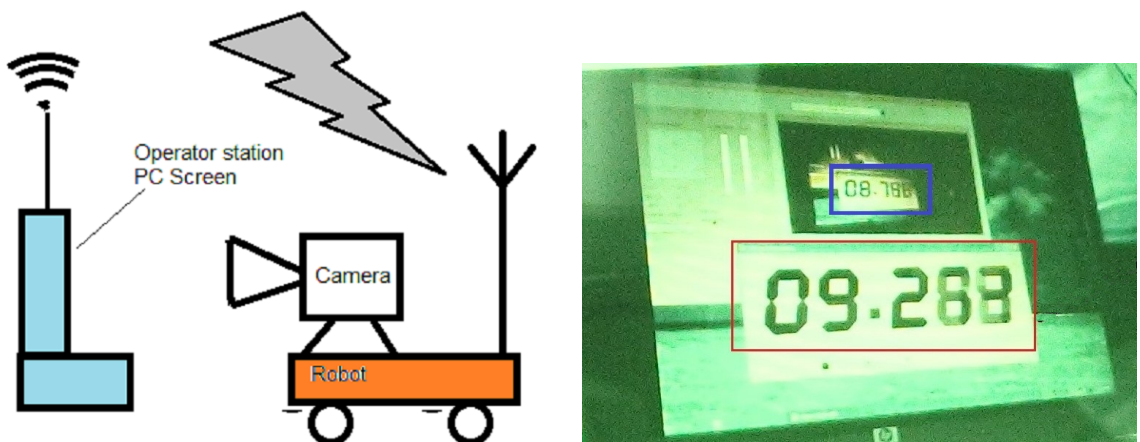


Figure A.2: Experimental setup: Schematic

Figure A.3: Screen shot of operator PC

Appendix B

B.1 Stability of Pure Pursuit under Time Delay

The kinematic model of a mobile robot is given by Equation B.1 and first order model for steering dynamics is given by Equation B.2

$$\begin{pmatrix} \dot{x}'_w \\ \dot{y}'_w \\ \dot{\theta} \end{pmatrix} = \begin{pmatrix} -V \sin \theta \\ V \cos \theta \\ V\gamma \end{pmatrix} \quad (\text{B.1})$$

$$\frac{d\gamma'}{dt} = -\frac{1}{T}(\gamma' - \gamma_r) \quad (\text{B.2})$$

where, (x', y', θ) is the posture of robot in coordinate system attached to the robot, V is the longitudinal velocity, γ is the angular velocity, T time constant of steering dynamics and γ_r the control input. Since the control input is generated by Pure Pursuit it is given by

$$\gamma_r = \frac{1}{r} = \frac{2x}{L^2} \quad (\text{B.3})$$

where r is defined in Equation 5.5 and L is the *look ahead distance*. The above Equations B.1 and B.2 using the fact that $\dot{y}'_w = 0$, because of the non-holonomic

constraint of the robot, can be written in the state space form as

$$\begin{pmatrix} \dot{x} \\ \dot{\theta} \\ \dot{\gamma} \end{pmatrix} = \begin{pmatrix} -\sin \theta \\ \gamma \\ -\gamma - \frac{2x}{l^2} \end{pmatrix} \quad (\text{B.4})$$

where the following scaling of variables were used to render it non-dimensional.

$$t = \frac{t'}{T}, \quad x = \frac{x'_w}{VT}, \quad \gamma = VT\gamma', \quad l = \frac{L}{VT}$$

The above system was linearised about the origin and delay τ in input was introduced to get Equation B.5

$$\begin{pmatrix} \dot{x} \\ \dot{\theta} \\ \dot{\gamma} \end{pmatrix} = J \begin{pmatrix} x(t) \\ \theta(t) \\ \gamma(t) \end{pmatrix} + J_\tau \begin{pmatrix} x(t-\tau) \\ \theta(t-\tau) \\ \gamma(t-\tau) \end{pmatrix} \quad (\text{B.5})$$

where J is the Jacobian with respect to state and J_τ is Jacobian with respect to τ . Based on location of roots of the Characteristic Quasi-Polynomial $q(s)$ given by

$$q(s) = \det[sI - J - J_\tau e^{s\tau}]$$

limiting look ahead distance L , for stable path tracking of a circular path for different input delays was presented by Ollero [45]. The results are represented here for in Figure B.1.

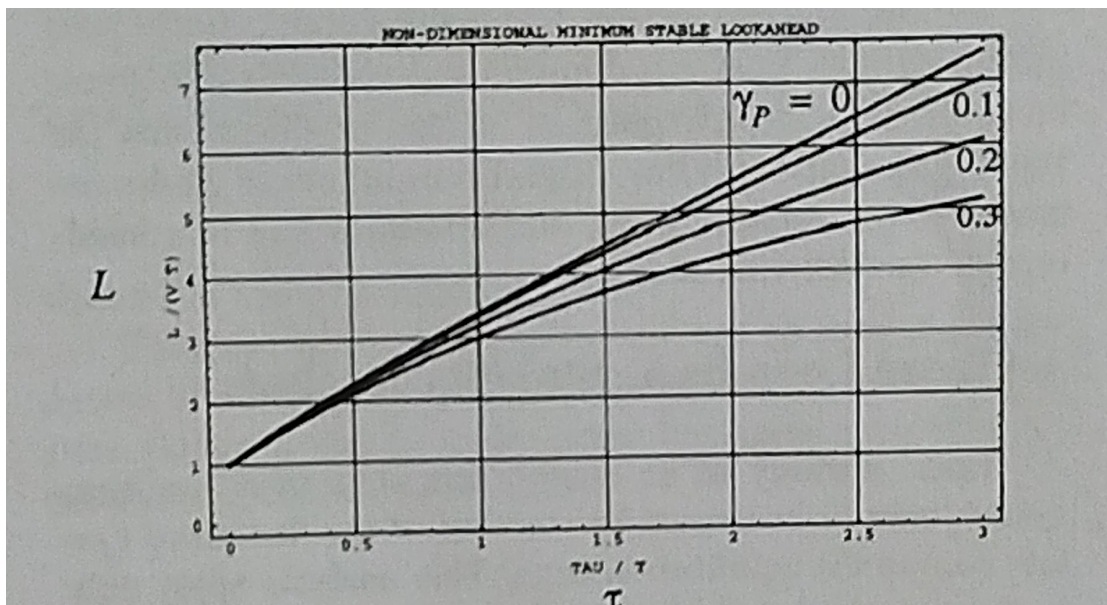


Figure B.1: Results obtained by Ollero [45]

Appendix C

C.1 Optimal Design of Steering Linkages

Objective is to minimize turning radius within the space available after installation of the rear wheel assembly, battery compartment and scissor mechanism on a given over all frame size of the vehicle. The design variables are x , a , h , and w . These variables are described in Chapter 2 and shown in Figures 2.7 and 2.8

Objective function to be minimized is the turning radius, R given by

$$R = \frac{a}{2} + \frac{w(h^2 + b^2 - bx)}{hx} \quad (\text{C.1})$$

where

$$\frac{2b}{h} = \frac{a}{w}$$

The constrain equations are

$$x < \frac{a}{2} - b - 20$$

$$h^2 + \left(\frac{a}{2}\right)^2 < 100^2$$

The bonds on the design variables are given by

$$30 < h < 200$$

$$500 < w < 600$$

$$50 < a < 270$$

$$0 < x$$

The minimization was carried out in Matlab using *fmincon()* function. The resulting minimum radius thus obtained was

$$R_{min} = 228 \text{ mm}$$

The corresponding design variables obtained were

$$h = 30 \text{ mm}, w = 515 \text{ mm}, a = 190 \text{ mm}, x = 69.8 \text{ mm}$$

The achieved minimum turning radius was $R_{min} = 415 \text{ mm}$. This was due to introduction of support for the rack and links which were not taken into consideration in the optimization process.

Publications from the Thesis

Research papers published/presented/under preparation are listed below

Conference

1. Das Amaren P., et al. "Design of a Teleoperated Mobile Manipulator for Inspection of Cyclotron Vault." *Machines, Mechanism and Robotics-Proceedings of iNaCoMM 2017*. Springer, Singapore, 2019. 529-540.
2. Das Amaren P., Saha S. K., Bhasin S., and Badodkar D. N., "Kinematic and Dynamic of redundantly actuated mobile robot using NOC", *under preparation*
3. Das Amaren P., Saha S. K., Bhasin S., and Badodkar D. N., "RGB-D based Predictive Display for Tele-operation of Mobile Robot in Unknown Environment", To be Submitted to *Advances in Robotics, International Conference of Robotics Society of India, (AiR 2019)*, IIT Madras, Chennai, July 2-6, 2019
4. Das Amaren P., Saha S. K., Bhasin S., and Badodkar D. N., "Control Architecture for Tele-operated Mobile Platform for Radiation Mapping in Radioactive Areas", *under preparation*

Brief Bio-data of the Author

Shri Amaren Prasanna Das, graduated in Mechanical Engineering from Kalyani Government Engineering College, Kalyani, West Bengal, India thereafter joined BARC Training School in the year 1999. After successful completion of the one year orientation training in Nuclear Science and Technology, he joined Division of Remote Handling and Robotics, BARC, Mumbai in 2000 as Scientific Officer-C. Subsequently, he obtained his M.Tech. degree in Systems and Control Engineering from IIT-Bombay, Mumbai in 2007. He joined Ph.D. in 2012 in the Department of Mechanical Engineering at Indian Institute of Technology Delhi as an external part-time Ph. D. scholar.